Use of the $^1S_0$ Neutron-Proton Scattering Length as a Probe for Three-Nucleon Forces

by

Frank Salinas Meneses

Department of Physics
Duke University

Date: _____
Approved:

_____
Calvin Howell, Supervisor

_____
Werner Tornow

_____
Seog Oh

_____
Russell Roberson

_____
Roxanne Springer

Dissertation submitted in partial fulfillment of
the requirements for the degree of
Doctor of Philosophy in the Department of Physics
in the Graduate School of Duke University

1998

ABSTRACT

(Physics – Nuclear)

Use of the $^1S_0$ Neutron-Proton Scattering Length as a Probe for Three-Nucleon Forces

by

Frank Salinas Meneses

Department of Physics
Duke University

Date: _____
Approved:

_____
Calvin Howell, Supervisor

_____
Werner Tornow

_____
Seog Oh

_____
Russell Roberson

_____
Roxanne Springer

An abstract submitted in partial fulfillment of
the requirements for the degree of
Doctor of Philosophy in the Department of Physics
in the Graduate School of Duke University

1998

ABSTRACT

Use of the $^1S_0$ Neutron-Proton Scattering Length as a Probe for Three-Nucleon Forces

by

Frank Salinas Meneses

The three-nucleon force has been suggested [Šla89] as an explanation for the discrepancy in the values of the neutron-neutron scattering length a_{nn} determined from the $^2H(\pi^-, nn\gamma)$ reaction (-18.6 ± 0.3 fm [Mil90]) and the world-average value obtained from kinematically complete neutron-deuteron breakup experiments (-16.73 ± 0.47 fm [Mil90]). In breakup experiments there are three nucleons in the exit channel, whereas there are only two in $\pi^- - d$. The hypothesis is that in nd breakup the interaction between nucleons is distorted by the presence of the third one.

To investigate possible three-nucleon force (3NF) effects, we have performed a measurement of the neutron-proton scattering length a_{np} in a kinematically complete ^{2}H(n,nnp) experiment at an incident neutron energy of 13.0 MeV. All measurements were conducted at TUNL and used the tandem accelerator. The value of a_{np} is very well known from two-nucleon scattering (-23.749 ± 0.008 fm) [Koe75]. A deviation from the well-known value would be evidence in favor of three-nucleon forces. In this work we measured the cross section for the neutron-proton final-state interaction (np FSI). In the np FSI one of the neutrons and the proton resulting from the break up process leave with zero relative momentum. The proton was detected in a deuterated scintillator, which served as the target. The neutrons were detected with liquid organic scintillators placed at angles defined by the kinematics of the reaction. Their energies were determined from their time-of-flight from the target to the neutron detector. In the present investigation of the 3NF, we have determined a_{np} values from our cross section measurements at four production angles ($\theta_{np} = 20.5^\circ, 28.0^\circ, 35.5^\circ$, and 43.0°) of the np FSI . Theoretical studies [Hüb93] suggest

that a 3NF should have a strong angular dependence.

The values of a_{np} were determined in this work by direct comparison of our measured cross sections to theoretical predictions from Faddeev calculations, which were made using a modified version of the Bonn-B (OBEPQ) nucleon-nucleon potential. In this version of the Bonn potential, the value of a_{np} can be easily adjusted. A Monte-Carlo simulation was used to average the calculations over the finite geometry, the beam energy spread, and the energy resolution of the detectors of our experimental setup. At each production angle of the np FSI, the cross section was simulated for $a_{np} = -22.0, -23.0, -23.75$, and -25.0 fm. A χ^2 analysis of a_{np} was performed at each production angle to determine the value which best fits experimental cross section.

Our measurements gave $a_{np} = -23.4 \pm 0.77$ fm. This result is consistent with the two-nucleon value for a_{np} within the experimental uncertainty. Additionally, there was no strong angular dependence observed in the value of a_{np}. We conclude from these findings that any 3NF effects on the nucleon-nucleon FSI cross section in nd breakup are insufficient in size to explain the discrepancy between the nd and the $\pi^- - d$ measurements of a_{nn}.

Acknowledgements

This experiment is the product of the work and effort of the TUNL neutron time-of-flight (TOF) group. Special thanks go to my advisor Calvin Howell for his help, and guidance during all these years. He was of invaluable assistance during all stages of this experiment. I give my deep appreciation to Werner Tornow for his dedication, patience and vast knowledge of physics, on which we could always count on. I am greatly indebted to my long-time friend and colleague, Dinko Eduardo González Trotter, for his tremendous work, insight and patience during these years and for the countless hours spent in discussions about the experiment. He was responsible for the the electronic equipment setup, part of the data analysis, and the Monte-Carlo simulations used in the comparisons of theoretical results and experimental data. I am also indebted to the members of the neutron TOF group for their help and friendship: Qiankun Chen, Alex Crowell, Chris Roper, and Richard Walter. Special thanks go to the former TOF graduate student Dr. Ross Setze for his guidance, and for his enormous help in developing the data analysis techniques and in the measurements of the neutron detector efficiencies. In addition, the following visiting scientists also contributed: Yingtang Chen [1], Zemin Chen [1], Hongqing Tang [2], Zuying Zhou [2] and Scott Carman [3]. Henryk Witała [4] from the Bochum-Cracow group provided the program to rigorously calculate the nd elastic and the breakup cross sections, which

[1] Tsinghua University, Beijing, China
[2] CIAE, Beijing, China
[3] Lawrence Livermore National Laboratory
[4] Jagellonian University, Cracow, Poland

allowed us to create libraries for the Monte-Carlo simulations.

The present work also owes a lot to all the technical staff at TUNL. I am grateful to Paul Carter and Richard O'Quinn for the superb state in which they kept the TUNL tandem accelerator and the ion source, and for their assistance in solving equipment problems. a big thanks goes to Sidney Edwards for his excellent administration of the TUNL VAX computer cluster where a big part of the data analysis was performed. This project is indebted to both Sidney Edwards and Patrick Mullkey for their assistance with the maintenance of the electronic equipment and the fabrication of the "miles" of cable needed to form the trigger circuit. Also, I would like to thank all the secretaries in both the Duke Physics department and in TUNL, specially Donna Rugger and Patricia Gibson who were always very helpful and kind. They contribute a large part to the smooth functioning of these institutions.

Above all, I want to thank my family for their love and support during all my life. Both my parents Eduardo Salinas Málaga and Soledad Meneses de Salinas always instilled in me the love of knowledge and allowed me to follow my own path. I also want to thank my brother Gonzalo Salinas Meneses and my sister Delsy Salinas Meneses for all their love and support.

Frank Salinas Meneses

Duke University

March 1998

To My Family

Contents

List of Figures

List of Tables

Chapter 1

Introduction

Nuclei are highly resonant quantum systems held together by the strongest force in nature. The fundamental constituents of nuclei are quarks in groups of three and held together by gluons. In principle, all nuclear phenomena should be derivable from the solution of the many-body problem describing nuclear systems as the interactions of quarks and gluons. Though this perspective is appealing, it is presently not mathematically tractable for mainly two reasons. First, the form of the quark-quark interaction needed to bind quarks into hadrons prevents the use of perturbation theory at distances relevant to nuclei. Second, the dimensions of the eigenstate basis, even for simple nuclei, exceed the computational capabilities of today's most powerful computer systems. So for now, we rely on approximations and models to explain nuclear phenomena in terms of fundamental interactions.

The discovery of the neutron by James Chadwick in 1932 answered the question of the missing mass in medium- and heavy-mass nuclei and in many ways started the field of nuclear physics. The dynamics of the interactions of the constituent particles are inherently different from those of the atom. In the atom, the electrons are held in fixed orbits about the massive (approximately 2000 times the mass of the electron cloud) and positively charged nucleus by electromagnetic forces. The influences of the electron-electron interactions on atomic structure are modest. In contrast, the constituents of nuclei are strongly interacting,

and it is these interactions that define the structure of these tightly bound systems. In spite of this seemingly "plum-pudding" arrangement of constituents, it was found that neutrons and protons orbit about the center of mass of the system in well-defined orbits, much like electrons in atoms, and consequently a shell structure exists. The nuclear shell model is built on a similar premise as in atomic physics. The motion of the nucleons are assumed to be constrained by their interactions with a central potential. The interaction of nucleons with each other is assumed to be small. In the case of nuclei, the central potential is the result of the many-body interactions in the system. Though both systems exhibit a many-body shell structure, the dynamics of nuclei are much more complicated than those of atoms, and the shell model cannot explain all nuclear phenomena. There are a number of phenomena that the shell model is inherently incapable of predicting. Some examples are:

1. The constant density of nuclei with the radius proportional to $A^{1/3}$.
2. The systematic dependence of neutron excess (N-Z) on $A^{5/2}$ for stable nuclei.
3. The fission by thermal neutrons of U^{235} and other odd-N nuclei.
4. The back bending of the moment of inertia of nuclei.

The liquid-drop model was developed to explain phenomena that were outside the realm of the shell model. It is in some ways the antithesis of the shell model in the sense that it assumes that nucleons interact strongly with each other. The feature that is common between the nuclear shell model and the liquid-drop models of nuclei is the reduction of a many-body problem into a two-body problem using a mean field. It is the nuclear mean field that should be derivable from the fundamental theory of the strong interaction, quantum chromodynamics (QCD). As discussed above, deriving the nuclear mean field from the quark-quark interaction is beyond present computational capabilities, even for light-mass nuclei. However, the problem can be simplified by using a folding model. In folding models, the nucleon-nucleon (NN) potential is convoluted with the nuclear matter density

function to produce the nuclear mean potential. Though the approach is approximate, it does provide a connection between bulk matter nuclear phenomena and the underlying fundamental interactions. For obvious reasons, the results from folding-model calculations depend critically on the NN interactions used.

Meson-exchange models of the NN interaction describe an impressive amount of two-nucleon data and are accepted as the low-energy limit of QCD. The parameters of meson-exchange potentials are adjusted to fit two-nucleon free scattering data and the properties of the deuteron. However, there is substantial evidence that the free NN interaction is altered inside nuclear matter, and therefore the potential models developed by fitting free two-nucleon data cannot be directly applied to nuclei. One striking piece of evidence is that most developed meson-exchange potentials, Bonn-B [Mac87], Paris, and AV-18, fail to reproduce the density where nuclear matter saturates. Of course these calculations were done within the framework of the folding model and are subject to the criticisms of the model. Developments over the last decade on calculations of observables in few-nucleon systems provide the theoretical framework for connecting bound-state and scattering phenomena to attributes of the basic NN interaction. The most progress has been made in the three-nucleon system.

Three-nucleon (3N) continuum observables can be rigorously computed to a numerical accuracy of less than 1% using realistic NN meson-exchange potentials. Though the 3N system has too few nucleons to honestly discuss it in terms of a mean field, there are some indications that the free two-nucleon forces are modified in this relatively simple system. Among the evidence are:

1. The leading meson-exchange potentials underbind the triton by almost 0.8 out of 8.48 MeV.

2. The discrepancy between the $^1S_0$ neutron-neutron scattering length (a_{nn}) determined from neutron-deuteron (nd) breakup measurements [Šla89] and the values extracted from pion-deuteron capture [Gab84].

3. The slight angular dependence of the $^1S_0$ neutron-proton scattering length (a_{np}) extracted from proton-deuteron (pd) breakup data using a simplified theoretical approach [Brü70].

In this thesis, we exploit the solid theoretical foundation of the three-nucleon system, the high sensitivity of the NN scattering length to small variations in the nuclear potential, and the accurately determined value of a_{np} [Koe75] to investigate medium modifications to the neutron-proton (np) interaction. In the present work, we measured differential cross sections for the ^{2}H(n,nnp) reaction in the kinematic region of the neutron-proton final-state interaction (np FSI). Cross sections were measured at four production angles of the np FSI for an incident neutron energy of 13.0 MeV. A value of a_{np} is extracted from the data at each production angle to determine if there is a deviation from the two-nucleon value, and to see if there is any angular dependence.

In the remainder of this chapter, I give an intuitive definition of the S-wave scattering length, describe how a_{np} has been determined in the two-nucleon system, and present the pertinent kinematic relationships needed to discuss nd breakup .

1.1 The Scattering Length

In the limit of zero-energy scattering between two particles, the cross section is given by

$$\lim_{k\to 0} \sigma = 4\pi a^2, \tag{1.1}$$

where a is the scattering length.

An intuitive way of understanding the scattering length is shown in Fig. 1.1, where the radial wave function of a two-nucleon system is shown. The intercept of the line tangent to the wave function at the range of the interaction potential with the radial axis is the scattering length. For a bound system the boundary conditions impose a positive scattering length. For an unbound system the scattering length is negative.

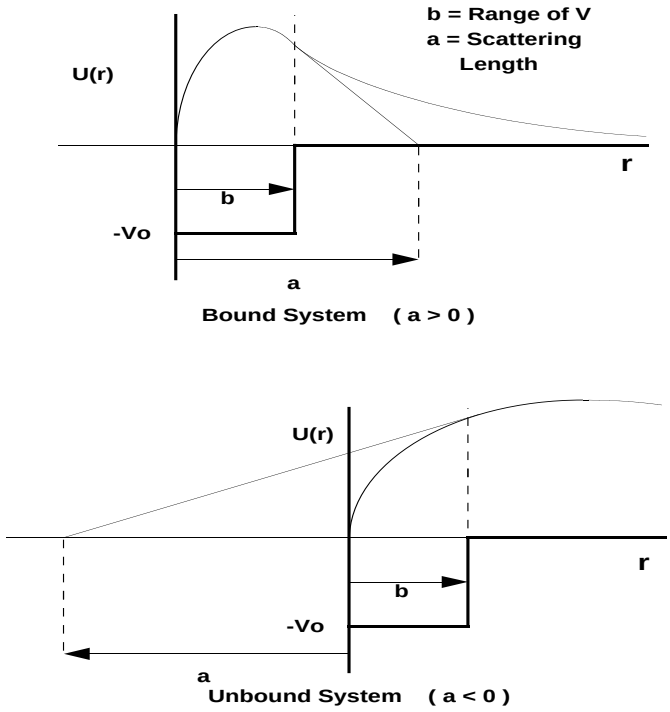

Figure 1.1: The radial wave functions for a two-body system system. The top figure is for a bound system. The bottom figure is for an unbound system. The intercept of the tangent line at the range of the potential with the axis gives the scattering length.

The scattering length is a very powerful magnifying glass of the nuclear potential for systems that are nearly bound. A change of the order of $\sim 1\%$ in the potential translates to about a ~ 3 fm change in the scattering length out of around 20 fm.

The np spin singlet system is slightly unbound, therefore the $^1S_0$ neutron-proton scattering length (a_{np}) is an ideal observable for investigating deviations in the NN interaction due to medium effects in the three-nucleon system. There is a discrepancy in the value of the $^1S_0$ neutron-neutron scattering length extracted from measurements using the $\pi^- - d$ reaction (-18.5 ± 0.3 fm) [Gab84] and the value obtained from kinematically complete nd breakup experiments (-16.73 ± 0.47 fm) [Šla89]. Since in the first reaction there are two nucleons in the exit channel, while the second one has three, some researchers have speculated that the discrepancy is due to a three-nucleon force (3NF), i.e. a force that depends on the simultaneous quantum numbers of the three nucleons. If a three-nucleon

force is responsible for the discrepancy in the value of a_{nn} extracted from two- and three-nucleon reactions, then the same discrepancy should show up in a measurement of a_{np} in a three-nucleon reaction like nd breakup .

Studies of 3NF effects using the Tucson-Melbourne three-nucleon force indicate a significant production-angle dependence for the np FSI cross section [Wit96]. The $\theta_{np} = 43.0^\circ$ np FSI configuration (θ_{np} is the angle at which the np pair is emitted in the final-state) is of special interest because according to predictions using the the Tucson-Melbourne 3NF, the effect of such a force vanishes at this angle. In addition, rigorous 3N calculations show that the np FSI cross section for $\theta_{np} = 43.0^\circ$ to be relatively insensitive to the details of various realistic potential models [Wit96], making it an ideal configuration from which to extract a_{np}.

Unlike a_{nn}, it is possible to measure a_{np} directly from neutron scattering off hydrogen targets. In fact, a_{np} is very well determined as will be discussed in the following section.

1.2 Sensitivity of the Scattering Length to the Nuclear Potential Strength

The variation of the scattering length with the strength of the nuclear potential can be estimated with a simple calculation. We begin by examining the different solutions of the Schrödinger equation when two particles interact with potentials of strength V and $V + \delta V$. The wave equations are

$$\frac{d^2u_0}{dr^2} + \frac{m}{\hbar^2}[E - V]u_0 = 0 \tag{1.2}$$

$$\frac{d^2u}{dr^2} + \frac{m}{\hbar^2}[E - V - \delta V]u = 0, \tag{1.3}$$

respectively.

Multiplying the first equation by $u(r)$ and the second one by $u_0(r)$, subtracting the first equation from the second, and integrating by parts inside the range b of the potential

we obtain the following relation between the logarithmic derivative of the wave function and the difference in the strength of the potentials

$$\frac{1}{u}\frac{du}{dr}\bigg|_{r=b} - \frac{1}{u_0}\frac{du_0}{dr}\bigg|_{r=b} = \frac{1}{u(b)u_0(b)}\frac{m}{\hbar^2}\int_0^b \delta V u u_0 dr. \tag{1.4}$$

At the boundary (i.e. at $r = b$), the internal and external wave functions match in value and in slope. The general form of the external solution for an unbound system is

$$u(r) = A\sin(kr + \delta), \tag{1.5}$$

where A is an arbitrary normalization factor. The logarithmic derivative at $r = b$ in the low energy limit (i.e. $k \to 0$) is given by

$$\frac{1}{u}\frac{du}{dr}\bigg|_{r=b} = -k\frac{A\cos(kr+\delta)}{A\sin(kr+\delta)} = -k\cot\delta = \frac{1}{a}, \tag{1.6}$$

where in the last equality we have used the usual definition of the scattering length in the finite range approximation. This result is also true for a bound system, where the external wave function is a decaying exponential.

Using the above result, the left hand side of equation 1.4 can be written as

$$\frac{1}{u}\frac{du}{dr} - \frac{1}{u_0}\frac{du_0}{dr} = -\frac{\delta a}{a^2}, \tag{1.7}$$

where we have taken the change in the scattering length δa to be small enough that the product $a(a + \delta a) \approx a^2$.

For a nearly-bound system, in the zero energy limit, the wavelength should be such that almost one quarter of the wave fits inside the range of the potential. We can use this fact to relate the range b and the average strength of the potential $\overline{V}$

$$b = \frac{1}{4}\lambda = \frac{1}{4}\frac{2\pi}{k} = \frac{\pi}{2}\hbar\frac{1}{\sqrt{m\overline{V}}}. \tag{1.8}$$

The wave functions $u(r)$ and $u_0(r)$ inside the range of the potential, for the nearly-bound case are

$$u(r) \approx u_0(r) \approx B\sin(\frac{\pi r}{2b}). \tag{1.9}$$

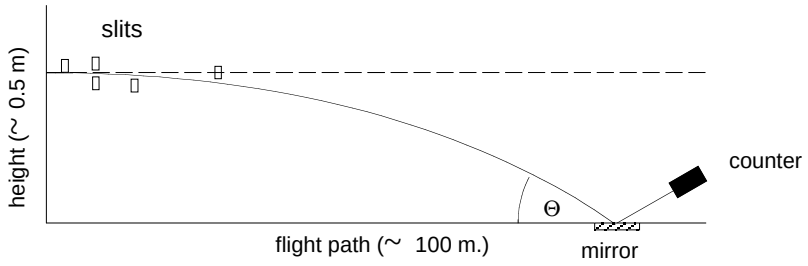

Figure 1.2: Experimental arrangement for the gravity refractometer technique used for the measurement of a_{np}.

Assuming a constant δV and using the wave functions in equation 1.9, the term on the right hand side of equation 1.4 can be evaluated at $r = b$

$$\frac{1}{uu_0}\frac{m}{\hbar^2}\int_0^b \delta V u u_0 dr = \frac{m}{\hbar^2}\delta V \int_0^b u u_0 dr = \frac{m}{\hbar^2}\delta V \frac{b}{2}. \tag{1.10}$$

Substituting the results of equations 1.8 into equation 1.10, and using equation 1.7, we obtain the desired relation between the fractional change in the scattering length in terms of the fractional change in the potential

$$-\frac{\delta a}{a} = \frac{a}{b}\left(\frac{\pi}{2}\right)^2 \frac{1}{2}\frac{\delta V}{V} = 1.23\frac{a}{b}\frac{\delta V}{V}. \tag{1.11}$$

For the case of the neutron-proton scattering length $a/b \approx 10$. Therefore, a small change in the potential is magnified by a factor of ten in the scattering length of a nearly-bound system.

1.3 Measurements of a_{np} in the Two-Nucleon System

The value of a_{np} has been very accurately extracted from direct two-nucleon reactions. The most accurate of these is the one using the gravity refractometer technique [Koe75]. A diagram of the experimental setup is shown in Fig. 1.2.

In this experiment, a beam of thermal neutrons (~ 0.1 meV) from a nuclear reactor travel in a near horizontal direction, falling by the action of gravity. The neutrons fall

towards a "mirror" made of various samples composed of carbon, hydrogen and chlorine. When the neutrons hit the mirror they will be reflected if their kinetic energy is not enough to overcome the mean potential $V = 2\pi\hbar^2 N a_{coh}/m$, where N is the density of target atoms, m is the neutron mass, and a_{coh} is the coherent scattering length of the sample. Hence, the critical height of fall, h_0, below which all neutrons are totally reflected is given by

$$N a_{coh} = \frac{m^2 g h_0}{2\pi\hbar^2}. \tag{1.12}$$

Because of damping effects due to absorption and incoherent scattering of neutrons, the reflection coefficient curve is not a step function at the critical height. Instead, the reflection curve as a function of height (h), the critical height (h_0), and the damping factor (A) is given by

$$R = \left| \frac{1 - \sqrt{(1 - h_0/h + iA/h)}}{1 + \sqrt{(1 - h_0/h + iA/h)}} \right|^2 . \tag{1.13}$$

The damping factor A is proportional to the absorption and incoherent scattering cross sections.

The critical height is measured for every sample. The height of fall is varied from the place where almost none of the neutrons are reflected to the detector, to a height where almost all neutrons are reflected. At each height the reflectivity, given by the ratio of the number of reflected neutrons to the number of incident neutrons, is calculated. Thus, the reflectivity curve for each substance is obtained. A sample curve is shown in Fig. 1.3. To extract the critical height a fit to the reflectivity curve is made using equation 1.13 with h_0 as a parameter. The coherent scattering length for the sample is calculated from the critical height using equation 1.12. For computing the scattering amplitudes of hydrogen, carbon, and chlorine, an over-determined system of equations of the form

$$a_{coh} = x \cdot a_C + y \cdot a_H + z \cdot a_{Cl} \tag{1.14}$$

is setup, where x, y, z are the number of atoms of carbon, hydrogen, and chlorine in each sample, respectively. Finally the system of equations is solved, and the proton scattering

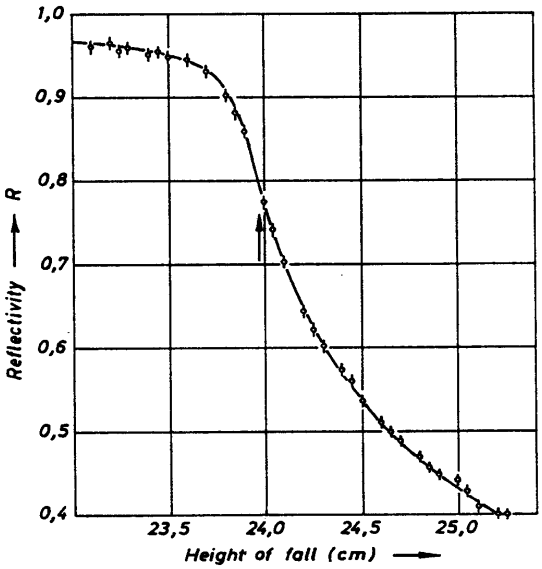

Figure 1.3: Reflectivity curve for toluene. The fit uses $h_0 = 23.955$ cm.

length a_p is obtained from the scattering length of hydrogen, a_H, by correcting for the contributions of deuterium.

The singlet (a_{np}) and triplet (a_t) neutron-proton scattering lengths can be calculated using the following relations involving a_p the extracted proton scattering length, and σ_0, the total neutron-proton cross section

$$\mu = \frac{1}{1 + m/m_H} \tag{1.15}$$

$$S^2 = \frac{1}{12}(\frac{\sigma_0}{\pi} - 4\mu^2 a_p^2) \tag{1.16}$$

$$a_t = \mu a_p + S \tag{1.17}$$

$$a_{np} = \mu a_p - 3S \tag{1.18}$$

The latest measurements report [Koe75] $a_t = 5.424 \pm 0.003$, and $a_{np} = -23.749 \pm 0.008$.

1.4 Three-Particle Kinematics

The breakup of a deuteron (Q = -2.25 MeV) by a neutron beam produces two neutrons and a proton in the exit channel. Using conservation of energy and momentum to eliminate the proton energy and momentum in the exit channel, we arrive at the equation for the kinematic locus in the plane of the neutron energies in the laboratory system:

$$\begin{aligned}\frac{1}{m_3}[&E_1(m_1+m_3)+E_2(m_2+m_3)\\ &-2\sqrt{m_0m_1E_0E_1}\cos\theta_1-2\sqrt{m_0m_2E_0E_2}\cos\theta_2\\ &+2\sqrt{m_1m_2E_1E_2}\cos\theta_{12}]=Q+E_0(1-\frac{m_0}{m_3}).\end{aligned} \tag{1.19}$$

The projectile energy and mass are E_0 and m_0. The subscripts 1 and 2 refer to the neutrons and the subscript 3 to the proton. The angles θ_1 and θ_2 are the angles at which the neutrons are ejected with respect to the beam axis. The angle θ_{12} is the angle between the neutrons. These three angles in our experiment are defined by the liquid scintillators, which were placed at fixed angles and distances from the target, and were used to detect the outgoing neutrons. This fixes the kinematic locus, and so determines the region of phase space where the energies of the two neutrons corresponding to *nd* breakup events will lie. For comparison with theoretical predictions, data are presented as a function of S, the distance along the locus. The kinematic locus is also called the S-curve. The starting point, i.e. the S = 0 point, is chosen at the place where the curve intersects the E_1 axis. At that point E_2 is zero. From that point S increases in a counter-clockwise direction along the locus. The kinematic loci for the four *np* FSI configurations are shown in Fig. 1.4.

This thesis is based on kinematically over-determined cross section measurements of the *np* FSI at four production angles, $\theta_{np} = 20.5°, 28.0°, 35.5°$ and $43.0°$. A $E_0 = 13$ MeV neutron beam was produced by the ^{2}H(d,n)^{3}He reaction. The beam was collimated and directed to a deuterated scintillator C_6D_{12} target (NE-232) where the *nd* breakup reaction occurs. Eight neutron detectors were placed at the four production angles to detect the neutron in the emitted *np* pair as described in chapter 3. Additionally, the second neutron

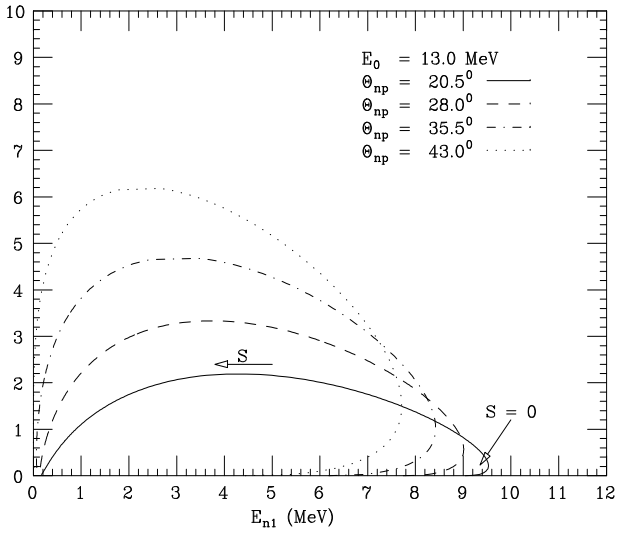

Figure 1.4: Kinematic S-curves for *nd* breakup , for the four *np* FSI configurations of this experiment. The neutron projectile has $E_0 = 13.0$ MeV.

produced by the breakup was detected using four other neutron detectors. The angles of these detectors were chosen for the special case when the proton and the first neutron leave at the same angle with zero relative energy. The direction of the second neutron is constrained by conservation of energy and momentum. The proton was detected in the deuterated scintillator target (also referred to as the center detector). The neutron energies were determined by the time-of-flight (TOF) method. The data were stored on tape in event-by-event mode for later off-line analysis. The statistical precision of the yields for all *np* FSI configurations was at least $\pm 4.8\%$.

Monte-Carlo simulation codes were written to account for the finite geometry of the detector setup, the energy resolution of the center detector, the attenuation of neutrons in their path towards the liquid scintillators, and the energy spread in the beam. These effects were folded into the theoretical prediction for direct comparison with the experimentally determined cross sections. Extensive three-nucleon calculations were done on a Cray Y-

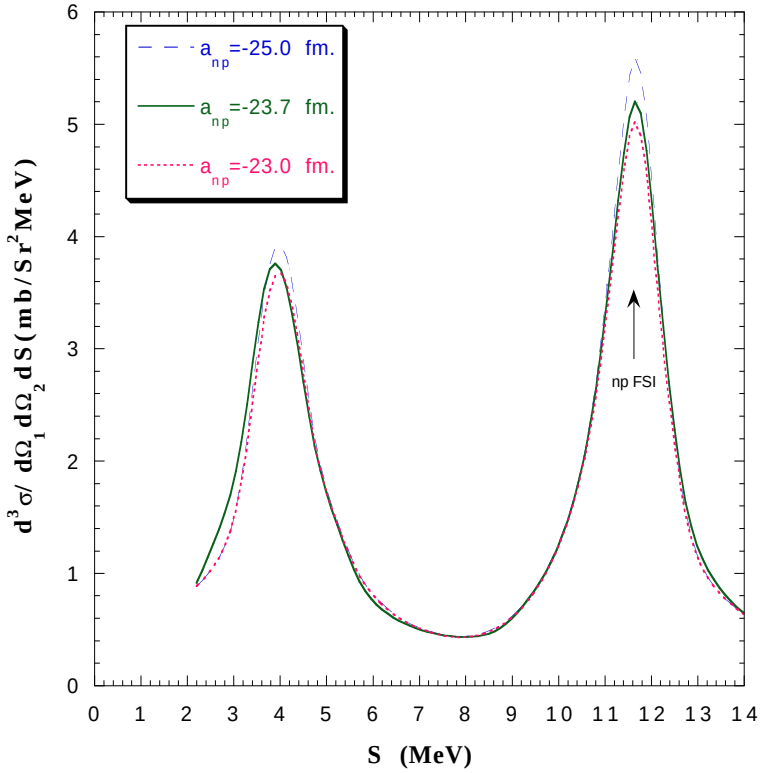

Figure 1.5: Cross section for the np FSI at $\theta_{np} = 43.0°$ along the kinematic locus for three different values of a_{np}.

MP at the North Carolina Super Computing Center to create the cross section libraries needed for the simulations. The calculations were performed over an energy and angle range sufficient to cover the entire phase space of the eight np FSI configurations of our experiment. The simulations include the neutron detector efficiencies which were measured at TUNL. These efficiency measurements were confirmed independently at PTB for two of the three types of detectors used in the experiment. [1].

The simulations used the Bonn-B OBEPQ NN potential. In this potential, we adjusted the coupling constant of the σ meson. There is a one-to-one correspondence between this coupling constant and a_{np}. To extract a_{np} one searches for the value of the

[1] Physikalisch-Technische Bundesanstalt, Braunschweig, Germany

coupling constant that produces a cross section which minimizes a χ^2 comparison with the experimental data. The sensitivity of the cross section along the kinematic locus to a_{np} is shown in Fig. 1.5 for $\theta_{np} = 43.0°$.

The rest of this thesis presents the details of the experiment. Chapter 2 is a review of the Bonn potential, two and three-body scattering, calculation of cross sections for the np FSI configurations and the techniques to include 3NFs into the calculation of cross sections. Chapter 3 explains the experimental equipment, and techniques used. Chapter 4 explains the details of the Monte-Carlo simulations of the experiment. Chapter 5 describes the methods used to extract a_{np} from the data. Chapter 6 is a description of the measurement of the neutron detection efficiencies of the detectors used in the experiment. This measurement is very important for the success of the experiment. Finally, chapter 7 presents the results and conclusions of this work.

Chapter 2

Theory

2.1 Introduction

Monte-Carlo simulations of the nd breakup experiment were used to compare theoretical predictions to experimental cross-sections. The cross-section libraries for the Monte-Carlo simulations were created from thee-nucleon (3N) Faddeev calculations [Fad61]. The calculations were made using the Bonn-B OBEPQ meson-exchange potential. In the Bonn-B potential the $^1S_0$ neutron-proton scattering length a_{np} was varied by adjusting the scalar-isoscalar σ meson-nucleon coupling constant.

Forty-eight cross-section libraries for nd breakup were used to analyze the data in this thesis. For each of the four detector-angle configurations where measurements were made, twelve cross-section libraries were created. Libraries were made for four values of a_{np} ($-22.0, -23.0, -23.75$, and -25.0 fm). The a_{np} values were chosen to cover the expected range of the experimental data and in fine enough steps to permit linear interpolation between a_{np} points. To cover the energy spread in the incident neutron beam ($\Delta E_0 = \pm 200keV$) libraries were generated at three energies ($E_0 = 12.8, 13.0$, and 13.2 MeV) for each a_{np} value.

All cross sections were computed using the computer codes supplied by H. Witała

of the Bochum-Cracow theory group [Glö96]. In this code, the three-body (3B) Faddeev equations are solved numerically. Faddeev solved the quantum mechanical 3B problem by decomposing the coupled equations for the transition amplitudes in such a way that the resulting kernel of the integral equations is connected and compact, and therefore suitable for numerical solution.

In this chapter, the theoretical framework used in the computer code by Witała is described. We start with a general discussion of the meson-exchange picture of the nucleon-nucleon interaction. Next, the theory of two- and three-body scattering is presented. In Section 2.4 details of the procedure for calculating cross sections from the transition amplitudes for the breakup reaction are given. The chapter is concluded with a presentation of the procedure used to include a three-nucleon force (3NF) into the calculations, with a calculation showing the effect of the Tucson-Melbourne 3NF on the cross section of nd breakup at the np FSI peak as a function of production angle. Note however, that a 3NF was not included into the potential used in our MC simulations.

2.2 Meson-Exchange Theory and the Bonn-B Potential

It is well accepted that Quantum Chromodynamics (QCD) is the fundamental theory of the strong interaction. However QCD does not allow solutions at low energies using perturbation methods because of its strong coupling constant. Currently, the best description of the strong interaction between nucleons is given by effective potentials based on meson-exchange theory.

Takenaki, Nakamura, and Sasaki [Tak51], proposed to subdivide the nuclear force into three regions:

1. a long range ("classical") region for inter-nucleon distance r larger than 2 fm,
2. an intermediate range ("dynamical") region (1 fm $\lesssim r \lesssim$ 2 fm), and
3. a short range ("core") region ($r \lesssim$ 1 fm).

This subdivision has proven very useful in nuclear physics because it allows a step-by-step exploration of the nuclear interaction. This classification will be used in the rest of this discussion.

Any potential characterizing the nucleon-nucleon (NN) interaction has to describe the following five empirical facts about the nuclear force:

1. The nuclear force is short ranged. This can be seen from the saturation properties of nuclei. Examples are, the constant binding energy per nucleon for nuclei with $A > 4$ and the fact that the nuclear density is roughly proportional to $A^{1/3}$.

2. It is attractive in the intermediate range. This is implied by nuclear binding and more directly by the positive S-wave phase shifts at low energies ($\lesssim 300$ MeV).

3. There is a repulsive core (for $r \lesssim 1$ fm), as evidenced by the negative s-wave phase-shifts at high energies ($\gtrsim 300$ MeV).

4. The nuclear force has a tensor component. Evidence supporting this fact are the quadrupole moment and the asymptotic D/S ratio of the deuteron, and the non-vanishing mixing parameters ϵ_J obtained in a phase-shift analysis of NN scattering data.

5. There is a strong short-ranged spin-orbit force. This is seen from the shape of the triplet P-wave phase shifts.

Additionally, there is a small spin-spin force ($\sigma_\mathbf{1} \cdot \sigma_\mathbf{2}$).

The Bonn potential is a field theoretical model based on the exchange of several types of mesons. In this model, the meson and nucleon masses are fixed and the meson-nucleon couplings are left as parameters to fit experimental data. The model includes diagrams where a nucleon is excited into a Δ isobar resonance (1232 MeV). The Bonn potential includes the following diagrams:

1. One-Meson Exchange: Here we have the pions, responsible for the long range interaction (mostly tensor), the ω mesons, important for the spin-orbit force and the short range repulsion, the ρ meson, which reduces the tensor force in the short range region, and δ mesons, which add a small contribution to the central force (s-wave interactions).

2. 2-π Exchange: These include s-wave correlated and uncorrelated exchanges. They are important to provide the intermediate range attraction of the nuclear potential.

3. $\pi - \rho$ Exchange: These are important to give the core region its strong repulsion. They have their greatest effect on the lower partial waves ($^1S_0$,$^3P_1$,$^3P_0$).

The mesons differ in their isospin, field type and coupling strength. The following types of fields are included:

1. the pseudoscalar (ps) field,

2. the scalar (s) field, and

3. the vector (v) field. The vector field has two different couplings. A vector coupling g_v and a tensor coupling f_v.

Because mesons and nucleons are not point particles, a form factor must be introduced to describe the aggregate structure of the meson-nucleon vertex. These form factors are of the form

$$\left(\frac{\Lambda_\alpha^2 - m_\alpha^2}{\Lambda_\alpha^2 - \mathbf{k}^2}\right)^{n_\alpha}, \tag{2.1}$$

where α represents the type of meson, Λ_α is called the cutoff mass, m_α is the meson mass, $\mathbf{k}$ is the three-momentum transfer, and n_α is an exponent dependent on the type of meson. For ω and ρ (vector mesons), n_α has a value of 2. For all other mesons, n_α has a value of 1. The cutoff masses suppress the contribution of high momenta, i.e. small distances, and are

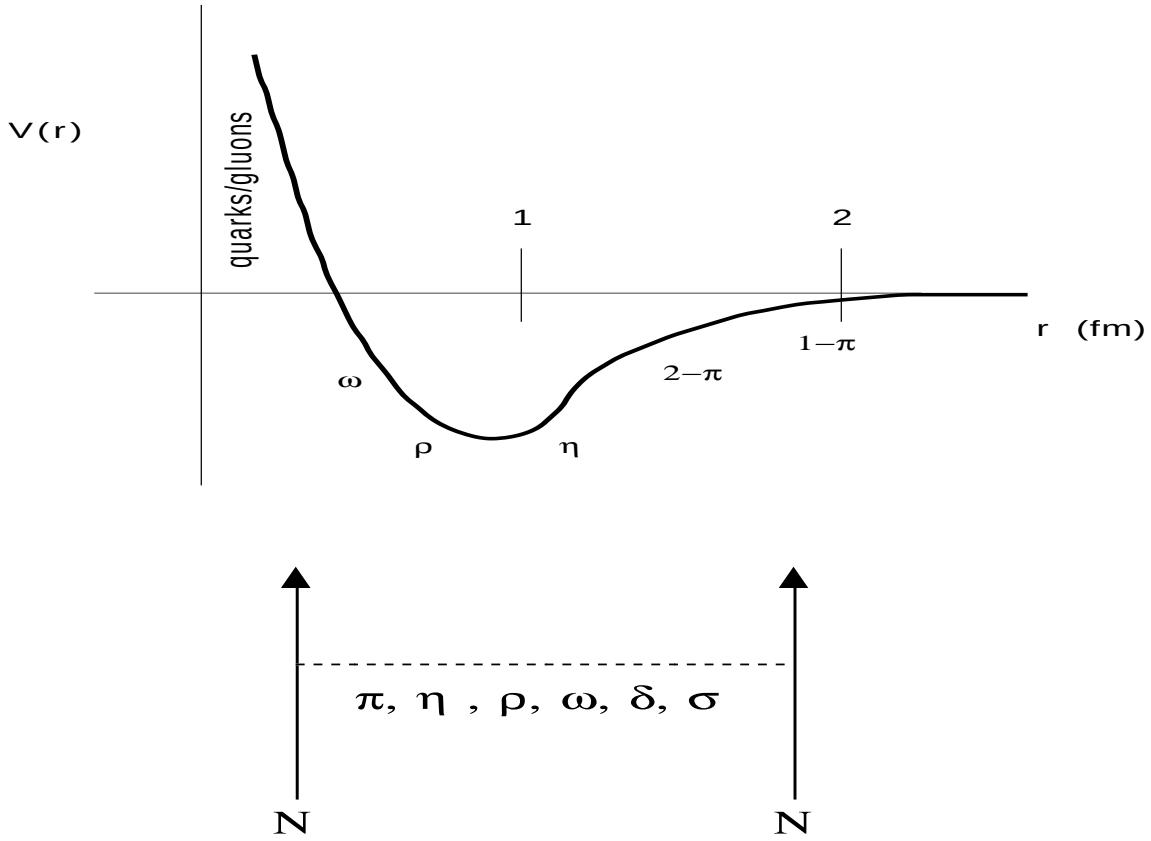

Figure 2.1: The Bonn-B potential can be subdivided in several regions where different mesons are dominant.

related to the hadron size. However, since a hadron size cannot be calculated from QCD, the cutoff masses are adjusted to fit empirical data.

The Bonn-B potential is a non-relativistic one-boson exchange potential derived from the full Bonn potential. The mesons included in the single meson-exchange diagrams are shown in Fig. 2.1. The Bonn-B potential uses the sigma meson (a scalar-isoscalar meson) as a one boson parameterization of the uncorrelated 2π and $\pi\rho$ exchanges. The σ meson's coupling constant and cutoff mass are adjusted to fit the NN data. The correlated s-wave 2π exchange diagrams are replaced by the exchange of the scalar-isoscalar σ' meson. The coupling of this meson is taken from s-wave $\pi\pi$ scattering phase shifts, so it is not a free parameter, unlike the coupling of the σ meson.

Table 2.1: Meson types and their effects on the different aspects of the nuclear force. The letter I denotes isospin.

Coupling	**Bosons (strength of coupling)**		**Characteristics of predicted forces**			
	I = 0 [1]	I = 1 $[\tau_1 \cdot \tau_2]$	Central [1]	Spin-Spin $[\sigma_1 \cdot \sigma_2]$	Tensor $[S_{12}]$	Spin-Orbit $[\mathbf{L} \cdot \mathbf{S}]$
ps	η (weak)	π (strong)	-	Weak, coherent with v, t	Strong	-
s	σ (strong)	δ (weak)	Strong, attractive	-	-	Coherent with v
v	ω (strong)	ρ (weak)	Strong, repulsive	Weak, coherent with ps	Opposite to ps	Strong, coherent with s
t	ω (weak)	ρ (strong)	- -	Weak, coherent with ps	Opposite to ps	-

The contributions of the η meson are not included in the full Bonn potential because it is a pseudoscalar meson of large mass (compared to the pion), and because it has a small coupling constant. These features make its effect very small. It is however included in the Bonn-B potential to improve the $^3P_1$ and $^3P_0$ phase shifts which are too high because the $\pi\rho$ exchange is excluded. Mesons with large $s\overline{s}$ content are also ignored because their coupling to the nucleon is suppressed according to Zweig's rule. Mesons with masses larger than 1 GeV are excluded because their short range effects are masked by the strong short-range repulsion from ω-exchange. Also the cutoff masses mimic structure at that scale.

Table 2.1 summarizes the effect on the different aspects of the nuclear force of the different mesons used in the Bonn-B potential. Table 2.2 shows the meson masses, their couplings and cutoff masses used in the Bonn-B potential The values of the coupling constants and cutoff masses are constrained by experimental NN scattering data. They are adjusted to reproduce the neutron-proton (np) phase-shift data.

For the creation of cross section libraries for the Monte-Carlo simulation of the present work, a modified version of the Bonn-B potential was used. In this version of the

Table 2.2: Masses, coupling constants and cutoff masses for the mesons in the Bonn-B potential

meson	**mass** (MeV)	$g_\alpha^2/4\pi$	Λ_α **(GeV)**
π	138.03	14.4	1.7
η	548.8	3	1.5
ρ	769	0.9	1.85
ω	782.6	24.5	1.85
δ	983	2.488	2.0
σ [a]	550	8.9437	1.9
	(720)	(18.3773)	(2.0)

[a] The σ parameters given in parenthesis apply to the $T = 0$ NN potential.

potential, the neutron-proton and the neutron-neutron interactions are treated separately. Thus, the σ coupling constant can be adjusted independently for the np interaction. Changing this coupling constant for the np interaction changes the value of a_{np}. The potential used in our simulations does not include a three-nucleon force.

2.3 Scattering Theory

2.3.1 2N Scattering

The two-body problem decomposes nicely into motion of the center of mass (CM) and motion relative to the CM. The problem then becomes equivalent to the motion of one particle of mass equal to the reduced mass $\mu = m_1 m_2/(m_1 + m_2)$ under the influence of a potential V and the free motion of the CM. The Schrödinger equation for two particles interacting through a potential V is given by

$$H \mid \Psi \rangle = (-\frac{1}{2\mu}\nabla^2 + V) \mid \Psi \rangle = (H_0 + V) \mid \Psi \rangle = i\frac{\partial}{\partial t} \mid \Psi \rangle. \tag{2.2}$$

The formal solution of the Schrödinger equation in terms of the eigenstates $\mid \phi \rangle$ of

the free Hamiltonian H_0 is

$$\mid \Psi^+ \rangle = \lim_{t\to\infty} e^{iHt}e^{-iH_0 t} \mid \phi \rangle = \Omega^+ \mid \phi \rangle. \tag{2.3}$$

The Ω^+ is called the Möller operator. The Möller operator evolves a solution of the free Hamiltonian in the infinite past into its corresponding solution of the interacting Hamiltonian. Similarly, one can define the backwards Möller operator Ω^-, which maps a free solution in the infinite future to a solution of the full Hamiltonian with the same energy.

In terms of the Möller operators, the amplitude of starting from a state $\mid \phi_0 \rangle$ of energy E_0 and scattering to another state $\mid \phi_f \rangle$ of energy E_f through the interaction V is given by

$$\langle \phi_f \mid S \mid \phi_0 \rangle = \langle \phi_f \mid \Omega^{(-)\dagger}\Omega^+ \mid \phi_0 \rangle. \tag{2.4}$$

This equation defines the S-matrix as the operator that evolves the initial scattering state from the infinite past to an eigenstate of the full Hamiltonian (using Ω^+), and then from this state to the corresponding free state in the infinite future (using $\Omega^{(-)\dagger}$).

To perform calculations it is better to use the Fourier transform of the Möller operators in energy space. The scattering state can then be expressed as

$$\mid \Psi^+ \rangle = \lim_{\epsilon\to 0} i\epsilon G(E+i\epsilon) \mid \phi \rangle = \lim_{\epsilon\to 0} i\epsilon \frac{1}{E+i\epsilon - H} \mid \phi \rangle. \tag{2.5}$$

The operator $G(E+i\epsilon)$ is the Green's function or propagator of the state of energy E by the full Hamiltonian H. In analogy to this operator the propagator under the free Hamiltonian is defined by

$$G_0(E+i\epsilon) = \frac{1}{E+i\epsilon - H_0}. \tag{2.6}$$

The full Green's function is related to the free propagator by the following Lippmann-Schwinger type equation

$$G = G_0 + G_0 V G = G_0 + G V G_0. \tag{2.7}$$

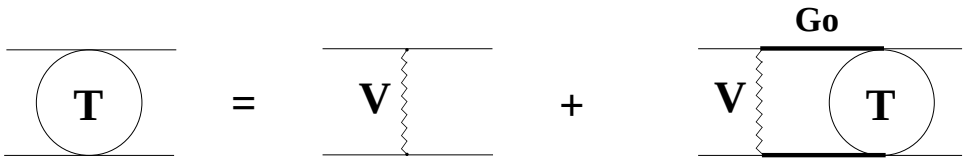

Figure 2.2: Two nucleon T-matrix. The wavy line indicates the interaction between the two nucleons by the potential V. Between interactions the particles propagate freely through G_0.

Using this resolvent identity, the S-matrix that takes an initial state $\mid \phi_0 \rangle$ of momentum $\mathbf{q_0}$ into a state $\mid \phi_f \rangle$ of momentum $\mathbf{q_f}$ can be written as

$$\begin{aligned} \langle \phi_f \mid S \mid \phi_0 \rangle &= \langle \phi_f \mid \Psi^+ \rangle \\ &= \delta(\mathbf{q_f} - \mathbf{q_0}) - 2\pi i \delta(E_f - E_0) \langle \phi_f \mid V \mid \Psi^+ \rangle \\ &= \delta(\mathbf{q_f} - \mathbf{q_0}) - 2\pi i \delta(E_f - E_0) \langle \phi_f \mid T \mid \phi_0 \rangle. \end{aligned} \tag{2.8}$$

Equation 2.8 defines the T-matrix. The T-matrix contains all the information about the scattering process. The scattering cross section can be written in terms of the T-matrix as

$$\frac{d\sigma}{d\Omega} = (2\pi)^4 \mu^2 \mid \langle \phi_f \mid T \mid \phi_0 \rangle \mid^2 . \tag{2.9}$$

The delta function in Equation 2.8 insures that the energy of the initial and final states is the same. Thus, the T-matrix element that enters Equation 2.9 is on-shell.

It can be shown that the T-matrix obeys the following integral equation (see Fig. 2.2)

$$T = V + VG_0T = V + TG_0V. \tag{2.10}$$

The procedure for finding the scattering cross section is to solve Equation 2.10 to obtain the T-matrix, and then use Equation 2.9 to find the cross section.

2.3.2 3N Scattering

The quantum mechanical three-body problem is considerably more difficult than the two-body one. The three particles can form various arrangements. Two particles can

be in a bound state, while the third one is separated from them far enough that there is no interaction between the free particle and the bound pair. These configurations are called the two-body fragmentation channels. Additionally, the three particles can be separated far enough from each other that there is negligible interaction between them, and they can be treated as free particles. This arrangement is the breakup channel.

The Hamiltonian for the scattering of three nucleons under the nuclear potential is:

$$H = \sum_{i=1}^{3} \frac{\mathbf{k_i}}{2m_i} + V_i + V_4. \tag{2.11}$$

The V_i are the two-nucleon potentials. The convention is that i is the particle not influenced by the potential V_i. For example V_1 is the potential between particles 2 and 3 while particle 1 is free. The potential V_4 represents a three-nucleon force(3NF). For the rest of this section the 3NF will not be included. The effects of such a force on the three-nucleon equations will be presented in Section 2.5.

To decouple the center of mass motion from the internal motion, it is convenient to transform the kinematic variables into the following Jacobi coordinates (see Fig. 2.3:

$$\mathbf{x} = \mathbf{x_2} - \mathbf{x_3} \tag{2.12}$$

$$\mathbf{y} = \mathbf{x_1} - \frac{m_2\mathbf{x_2} + m_3\mathbf{x_3}}{m_2 + m_3} \tag{2.13}$$

$$\mathbf{R} = \frac{m_1\mathbf{x_1} + m_2\mathbf{x_2} + m_3\mathbf{x_3}}{m_1 + m_2 + m_3}. \tag{2.14}$$

The conjugate momenta are then given by

$$\mathbf{p} = \frac{m_3\mathbf{k_2} - m_2\mathbf{k_3}}{m_2 + m_3} \tag{2.15}$$

$$\mathbf{q} = \frac{(m_2 + m_3)\mathbf{k_1} - m_1(\mathbf{k_2} + \mathbf{k_3})}{m_1 + m_2 + m_3} \tag{2.16}$$

$$\mathbf{K} = \mathbf{k_1} + \mathbf{k_2} + \mathbf{k_3}. \tag{2.17}$$

In terms of these coordinates the Hamiltonian becomes

$$H = \frac{\mathbf{K}}{2\sum m_i} + \frac{\mathbf{p}}{2\mu} + \frac{\mathbf{q}}{2M} + \sum_{i=1}^{3} V_i, \tag{2.18}$$

where the reduced masses are defined as

$$\mu = \frac{m_2 m_3}{m_2 + m_3} \qquad M = \frac{m_1(m_2 + m_3)}{m_1 + m_2 + m_3}. \tag{2.19}$$

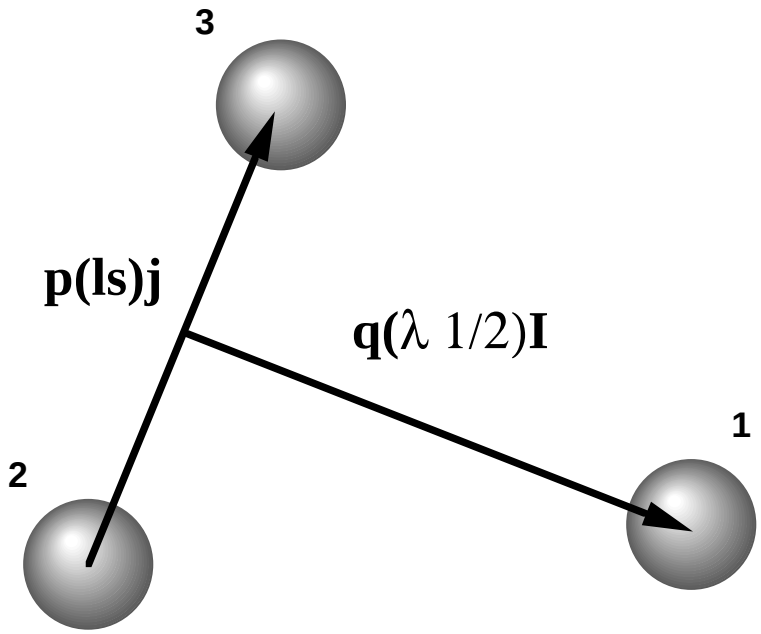

Figure 2.3: Jacobi linear and angular momentum coupling scheme for the three-nucleon system. The relative momentum between particles 2 and 3 is p. The angular momentum and total spin of the 2-3 sub-system are l and s, and the total angular momentum is j. The relative momentum between particle 1 and the center of mass of the 2-3 sub-system is q. The corresponding orbital angular momentum is λ and the spin of nucleon 1 is $\frac{1}{2}$, which couple to give the total angular momentum I.

The full and free propagators G and G_0 are defined as in the two-body scattering case. In addition, it is convenient to define the channel propagators

$$G_\alpha(E + i\epsilon) = \frac{1}{E + i\epsilon - H_\alpha}, \tag{2.20}$$

where $H_\alpha = H_0 + V_\alpha$ is called the channel Hamiltonian. Notice that the breakup channel is included if we allow the case $\alpha = 0$. In this case $V_0 = 0$. The full Hamiltonian written in

terms of the channel Hamiltonian becomes

$$H = H_\alpha + V^\alpha, \tag{2.21}$$

where $V^\alpha = \sum_{j \neq i} V_j$.

The eigenstates of the Hamiltonian for channel α are the states with particle α free and the other two either in a bound state, or in a scattering state, i.e.

$$\mid \psi_\alpha \rangle \;=\; \mid \phi_\alpha \rangle \mid \mathbf{q}_\alpha \rangle \qquad or \tag{2.22}$$

$$\mid \psi_\alpha \rangle \;=\; \mid \phi_\alpha^+ \rangle \mid \mathbf{q}_\alpha \rangle, \tag{2.23}$$

where the state $\mid \phi_\alpha \rangle$ is a bound state of the two particle subsystem in channel α. The state $\mid \phi_\alpha^+ \rangle$ is a state in the continuum of the interacting two-particle subsystem. In both states only the potential V_α is in action. The state $\mid \mathbf{q}_\alpha \rangle$ is a free state of particle α with definite momentum $\mathbf{q}_\alpha$ relative to the two-particle subsystem.

The solution of the full Hamiltonian in terms of the resolvent is, as in the two-body case,

$$\mid \Psi_\alpha^+ \rangle = \lim_{\epsilon \to 0} i\epsilon G(E + i\epsilon) \mid \phi_\alpha \rangle. \tag{2.24}$$

Using this result, the S-matrix elements can be defined in terms of the matrix elements of another operator analogous to the T-matrix of the two body case, called the U-matrix

$$\begin{aligned} S_{\alpha\beta} &= \delta_{\alpha\beta}\delta(\mathbf{q}_\alpha - \mathbf{q}_\beta) - 2i\pi\delta(E_\alpha - E_\beta)\langle \phi_\beta \mid V^\beta \mid \Psi_\alpha^+ \rangle \\ &= \delta_{\alpha\beta}\delta(\mathbf{q}_\alpha - \mathbf{q}_\beta) - 2i\pi\delta(E_\alpha - E_\beta)\langle \phi_\beta \mid U \mid \phi_\alpha \rangle. \end{aligned} \tag{2.25}$$

Using the resolvent equation and the relation between the channel potential and the two-body t-matrix of the two-particle subsystem, $G_\alpha V_\alpha = G_0 t_\alpha$, the U-matrix elements can be shown to obey the following set of coupled integral equations

$$U_{\beta\alpha} = V^\beta + \sum_{\gamma=0}^{3} U_{\beta\gamma} G_0 \overline{\delta}_{\gamma\alpha} t_\gamma, \tag{2.26}$$

where $t_0 = 0$, and $\overline{\delta}_{\beta\alpha} = 1 - \delta_{\beta\alpha}$. The kernel of this equation, $\overline{\delta}_{\gamma\beta} t_\gamma G_0$, is of the Faddeev type. Therefore, it is connected and compact as was shown by Faddeev [Fad65]. An example of

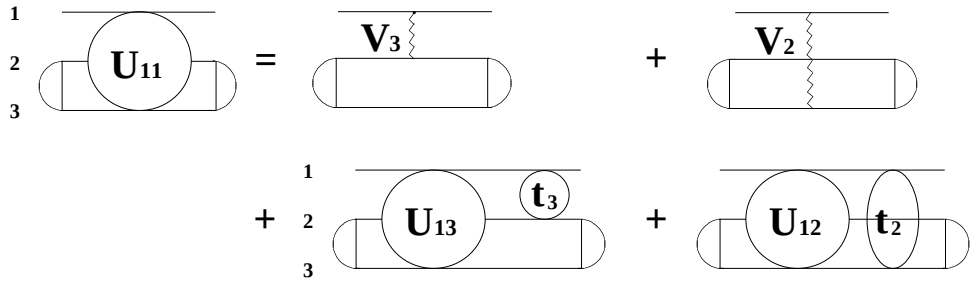

Figure 2.4: Example of the AGS equation for the U-matrix when particle 1 is a nucleon and particles 2 and 3 form the bound pair in both the entrance and exit channel. The wavy line indicates interaction between the connected particles through the channel potential. The t_i are the two-body t-matrices for the interaction between the connected particles.

the equation for the U_{11} amplitude is shown in Fig. 2.4. However, these set of equations still contain potentials and t-matrices. These equations can be expressed in terms of two-body t-matrices, by performing the following transformation

$$U_{\beta\alpha} \rightarrow \overline{\delta}_{\beta\alpha} G_{\alpha}^{-1} + U_{\beta\alpha}. \tag{2.27}$$

The new amplitudes are equal to the old ones on-shell. The new set of equations are called the Alt-Grassberger-Sandhas (AGS) [Alt67] equations, and they are as follows:

$$U_{\beta\alpha} = \overline{\delta}_{\beta\alpha} G_0^{-1} + \sum_{\gamma=0}^{3} \overline{\delta}_{\gamma\beta} t_\gamma G_0 U_{\gamma\alpha}. \tag{2.28}$$

2.3.3 Identical Particles

In nuclear physics, the isospin formalism allows neutrons and protons to be treated as identical particles. In this case, we need to use symmetrized wave functions. For this purpose we make use of the symmetrization operator

$$\mathcal{S} = 1 + P_{12}P_{23} + P_{13}P_{23} = 1 + P, \tag{2.29}$$

which when applied to a channel state (e.g. $\mid \phi_1 \rangle$) produces a fully antisymmetrized state

$$\mathcal{S} \mid \phi_1 \rangle = \mid \phi_1 \rangle + \mid \phi_2 \rangle + \mid \phi_3 \rangle. \tag{2.30}$$

The AGS equations reduce to

$$U \mid \phi \rangle = G_0^{-1} P \mid \phi \rangle + P t G_0 U \mid \phi \rangle. \tag{2.31}$$

We can define a three-body T-matrix as

$$T = t G_0 U, \tag{2.32}$$

and then from the AGS equation, we obtain an integral equation for T

$$T = tP + t G_0 P T. \tag{2.33}$$

The AGS equations for the case of breakup are related to the U operators in the rearrangement channels by

$$U_0 \mid \phi \rangle = (1+P) t G_0 U \mid \phi \rangle = (1+P) T \mid \phi \rangle. \tag{2.34}$$

The scattering cross section is related to the amplitude $\langle \phi_0 \mid U_0 \mid \phi \rangle$. The calculation of the cross section from the breakup amplitude will be explained in Section 2.4. The central problem is to find the solution of the integral equation for the T-matrix in Equation 2.33. Once the T-matrix is known, all other quantities can be calculated.

2.4 Breakup Cross Section

The breakup cross section can be calculated from the number of particles scattered into the momentum volume elements $d\mathbf{p_f}$ and $d\mathbf{q_f}$ per unit time, divided by the incoming flux. If we label the incoming neutron as particle 1 in the previous discussion, the initial state is an eigenstate of the channel 1 Hamiltonian

$$\mid \phi \rangle = \mid \varphi_d \rangle \mid \mathbf{q_0} \rangle, \tag{2.35}$$

where $\mid \varphi_d \rangle$ is the deuteron wave function (which is at rest in the lab system), and $\mid \mathbf{q_0} \rangle$ is a neutron of momentum $\mathbf{q_0}$ relative to the deuteron.

In the np FSI configuration, the final state has all the particles free.

$$\mid \phi_0 \rangle = \mid \mathbf{k_1} m_1 \mathbf{k_2} m_2 \mathbf{k_3} m_3 \rangle \tag{2.36}$$

where the $\mathbf{k_i}$ are the outgoing momenta of the nucleons in the lab system, and the m_i are the spin projections.

The scattered flux is then given by [Glö96]

$$\begin{aligned} dN &= 2\pi |\langle \phi_0 \mid U_0 \mid \phi \rangle|^2 \int d\mathbf{p} d\mathbf{q} \delta(\frac{3q_0^2}{4m} + \epsilon_d - \frac{p^2}{m} - \frac{3q^2}{4m}) \\ &= 2\pi |\langle \phi_0 \mid U_0 \mid \phi \rangle|^2 k_E d\Omega_1 d\Omega_2 dE_1, \end{aligned} \tag{2.37}$$

where k_E is the phase-space factor. It is more convenient to transform the phase space factor k_E from the density with respect to the energy of neutron 1 to the path length along the S-curve. In that case the density of states becomes

$$k_S \equiv k_E \frac{dE_1}{dS} = \frac{m^2 k_1^2 k_2^2}{\sqrt{k_1^2 (2k_2 - \hat{\mathbf{k}}_\mathbf{2} \cdot (\mathbf{q_0} - \mathbf{k_1}))^2 + k_2^2 (2k_1 - \hat{\mathbf{k}}_\mathbf{1} \cdot (\mathbf{q_0} - \mathbf{k_2}))^2}}. \tag{2.38}$$

Finally, using for the incoming flux

$$|\mathbf{j}| = \frac{3q_0}{2m}, \tag{2.39}$$

and the statistical factor

$$g = \frac{1}{(2s_d + 1)(2s_N + 1)}, \tag{2.40}$$

to average over all spins the cross section is given by

$$\frac{d^3\sigma}{d\Omega_1 d\Omega_2 dS} = \frac{1}{6}(2\pi)^4 \sum_{m_1, m_2, m_3} |\langle \phi_0 \mid U_0 \mid \phi \rangle|^2 \frac{2m}{3q_0} k_S. \tag{2.41}$$

Further details on the technical aspects of the calculations, accuracy tests and applications can be found in [Glö96] and [Fri95].

2.5 Three-Body Forces

Three-nucleon forces (3NF) depend in an irreducible way on the simultaneous coordinates, momenta and spins of the three interacting nucleons. These type of forces have been used in other fields of physics (e.g. the Axilrod-Teller-Muto force [Axi43], [Mut43]). They arise when the internal degrees of freedom of the interacting particles are hidden. An intuitive way to see how this comes about is to notice that the deformation of the internal constituents of a particle by the force from a second particle, will influence the interaction of the first particle with a third one.

In nuclear physics, QCD tells us that the nucleons have internal quark and gluon degrees of freedom. However, since it is not known yet how to make the transition from quarks and gluons to nucleons and mesons using QCD, nuclear physics uses potentials which treat the nucleons and mesons as elementary particles, thus hiding the quark and gluon degrees of freedom. There is no question then about the existence of 3NFs. What is not known is the form and strength of these forces. In nuclear physics there are several proposed 3NF potentials. The ones mainly used these days are the Tucson-Melbourne, the Brazilian,and the Ruhport three-nucleon forces.

In Section 2.3.2 the full Hamiltonian has the term V_4 representing a 3NF. One way to include 3NFs into the Faddeev equations for three-nucleon scattering, is to introduce a fourth transition amplitude U_{4i} defined as

$$U_{4i} \mid \phi_i \rangle = (V_1 + V_2 + V_3) \mid \Psi_i^+ \rangle. \tag{2.42}$$

A propagator and a t-matrix for the 3NF can also be defined,

$$G_4 = \lim_{\epsilon \to 0} \frac{1}{E + i\epsilon - H_0 - V_4} \quad and \tag{2.43}$$

$$t_4 = V_4 + V_4 G_0 t_4. \tag{2.44}$$

For the case of identical particles, the AGS equations for the rearrangement channels

are given by

$$\begin{aligned} U &= PG_0^{-1} + PtG_0U + t_4G_0U_4 \quad and \\ U_4 &= (1+P)G_0^{-1} + (1+P)tG_0U. \end{aligned} \tag{2.45}$$

Again, we can introduce T-matrix like operators T and T_4

$$\begin{aligned} T &= tG_0U \quad and \\ T_4 &= t_4G_0U_4, \end{aligned} \tag{2.46}$$

which, by using Equation 2.45, lead to the following coupled integral equations for T and T_4

$$\begin{aligned} T &= tP + tG_0T_4 + tG_0PT \\ T_4 &= (1+P)t_4 + (1+P)t_4G_0T. \end{aligned} \tag{2.47}$$

In terms of T and T_4 the transition amplitudes for elastic scattering and breakup become

$$\begin{aligned} U &= PG_0^{-1} + PT + T_4 \\ U_0 &= (1+P)T + T_4. \end{aligned} \tag{2.48}$$

The Bochum-Cracow group carried out calculations to test the sensitivity of np FSI cross sections to the Tucson-Melbourne (TM) 3NF using $j \leq 2$ for all NN and 3NF interactions (j is the total two-particle sub-system angular momentum). These 3NF cross section calculations used a standard form-factor cutoff parameter $\Lambda = 5.8\mu$ ($\mu = 139.6$ MeV), which when used in conjunction with the Bonn-B NN potential, overbinds the ^{3}H by 1.84 MeV. The Bonn-B OBEPQ was used for the NN part of the interaction [Wit96]. The results are shown in Fig. 2.5. The magnitude of the cross sections in these sensitivity calculations are lower than in a full calculation with $j \leq 3$. However, the comparison of the calculations with and without the TM 3NF, should give a reasonable estimate of the angular dependence of a_{np} due to a 3NF.

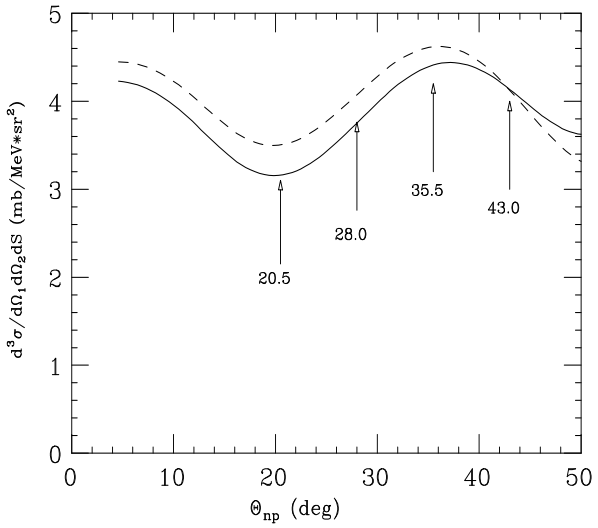

Figure 2.5: The curves are the cross section at the *np* FSI peak as a function of the production angle calculated with the Bonn-B potential with no 3NF (solid line), and with a 3NF (dashed line). The Tucson-Melbourne 3NF (cutoff parameter $\Lambda = 5.8\mu$ and $j \leq 2$) was used. If the TM model is correct, then for $\theta_{np} = 43.0^{\circ}$, the 3NF effect on the cross section vanishes. Therefore at this angle our experimental value of a_{np} should agree with the well-known a_{np}.

Chapter 3

Experimental Details

3.1 Overview

In this experiment differential cross sections for the neutron-induced breakup of the deuteron were measured for four different production angles of the neutron-proton final-state interaction (np FSI) kinematic configuration. The measurements were made in the shielded neutron source area at the Triangle Universities Nuclear Laboratory (TUNL). The momentum of each of the two neutrons and the energy of the proton from the breakup reaction were measured, completely defining the reaction kinematics. The two neutrons were detected in liquid-organic scintillators, and the proton was detected in the liquid C_6D_{12} scintillator cell, used as the scatterer. The energies of the neutrons were determined from time-of-flight (TOF) measurements, and the energy of the proton was determined from the pulse height of the signal from the C_6D_{12} scintillator.

This experiment was performed simultaneously with cross section measurements of the nn FSI for four production angles. Eight of the twelve neutron detectors used in the np FSI measurement were shared with the measurement of the nn FSI.

All measurements were made at an incident neutron energy E_0 of 13.0 MeV. The neutrons were produced by bombarding a deuterium gas target at 7.8 atm with a 10.0 MeV

deuteron beam. The neutrons emitted at 0° from the ^{2}H(d,n)^{3}He reaction, were collimated, and were used to bombard the deuterium scatterer. Details of the neutron production, the target, the shielding wall, and the collimator are given in Section 3.2. The floor plan of the accelerator bay and the target areas at TUNL is shown in Fig. 3.1. The deuterons used to produce the neutron beam were generated by a direct-extraction-negative-ion source (DENIS). A beam of negative deuterium was extracted from the duoplasmatron of DENIS at a transport energy of 50 keV, injected into the tandem accelerator, accelerated to an energy of 10.0 MeV, and transported to the neutron production target mounted at the end of the 20° beam line of the first beam energy analyzer magnet at the high-energy end of the accelerator bay. This area is shown in Fig. 3.1 as "Shielded Neutron Source". A description of the target area and the detector arrangement is presented in Section 3.3.

There are two neutrons produced in the neutron-induced breakup of the deuteron. For the *np* FSI kinematic condition, one of the neutrons goes in the same direction as the proton. This neutron will be called neutron 1 in subsequent discussions. In order to conserve momentum the two neutrons are emitted on opposite sides of the the incident neutron beam axis. Neutron 1 was detected in either an annulus shaped neutron detector placed at 1.5 m from the deuterium scatterer or in a cylinder shaped detector placed at 2.5 m from the scatterer, directly behind the ring detector and covering the solid angle of the opening in the ring detector. The other neutron, which will be referred to as neutron 2, was detected in a cylinder shaped neutron detector placed on the opposite side of the beam axis at an angle determined by the kinematics of the configuration. The distances of the four scintillator cells used to detect neutron 2 varied from 1.3 m to 2.1 m from the center of the scatterer. The protons produced were detected in the deuterated scintillator acting as the scatterer. The energy of the protons was determined from the pulse height of the signal from a photomultiplier coupled to the deuterated scintillator.

Data was also accumulated for neutron-deuteron (*nd*) elastic scattering. The recoil deuterons were detected in the center detector (the scatterer) in coincidence with the as-

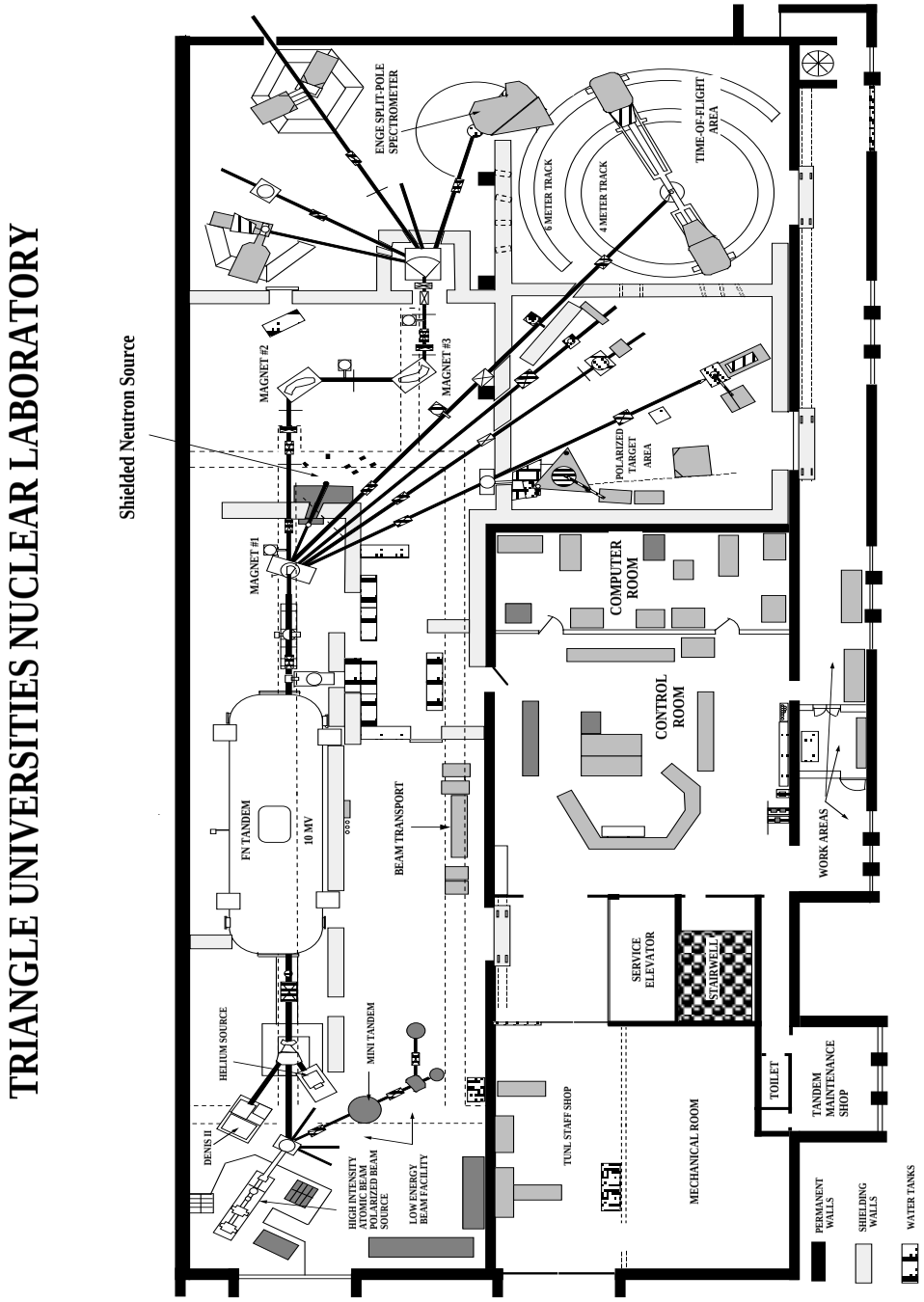

Figure 3.1: Triangle Universities Nuclear Laboratory (TUNL) floor plan. This experiment was performed in the "Shielded Neutron Source" area.

sociated neutron, which was detected in the neutron detector array. The cross section of *nd* elastic scattering at the energy of our experiment is known to an accuracy better than $\pm 1.5\%$. The elastic scattering data were used in the absolute normalization of the breakup data.

Light-emitting diodes (LEDs) were attached to some detectors to measure the dead time of the system for triple (n-n-p) and double (n-d) coincidence events. Pulser signals were introduced into the electronic circuit of ten detectors to measure the dead time of the trigger circuit and of the computer data acquisition system where 99.5% of the dead time occurred. The pulser frequency was 9.8 Hz, about 3.8% of the data trigger rate. The timing signal and the pulse-shape information for each detector were derived from the anode signals. The integrated and amplified dynode signals provided pulse-height information for each detector.

The experiment took about 2000 hours of beam time. Absolute neutron detection efficiencies for all detectors were determined at TUNL. The efficiency measurements are described in chapter 6.

3.2 Neutron Production and Collimation

Mono-energetic ($E_0 = 13.0$ MeV) neutrons were produced via the ^{2}H(d,n)^{3}He reaction in a deuterium gas cell (shown in Fig. 3.2) at 7.8 atm of pressure. This gas cell was the same one as described in [Set95]. The gas cell entrance was sealed with a 0.25 mil Havar foil, and its end consists of a gold beam stop with a thickness of 0.051 cm. The beam stop was soldered to the end of the gas cell to ensure good heat conduction. Copper tubes wound around the gas cell carrying 10°C circulating water cooled the body of the cell while a stream of compressed air was directed towards the beam stop to help remove heat. The complete assembly was electrically insulated from the rest of the beam pipe for accurate deuteron beam current integration.

The ^{2}H(d,n)^{3}He reaction has a large and very forward-peaked cross section for pro-

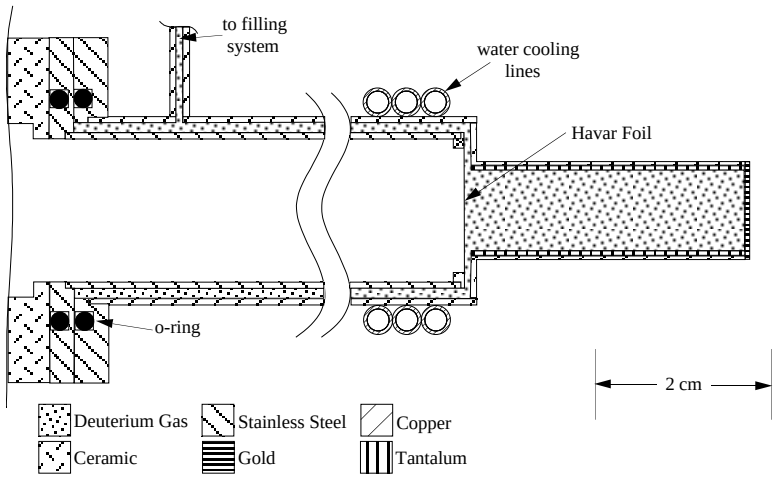

Figure 3.2: Lateral cross-sectional view of the neutron production gas cell used for the ^{2}H(d,n)^{3}He source reaction.

duction of nearly mono-energetic neutrons [Dro78]. The high positive Q-value (+3.3 MeV) of this reaction sets mono-energetic neutrons apart by ~ 5 MeV from the continuum energy spectrum of the breakup neutrons from deuteron breakup at the gold beam stop and from the ^{2}H(d,n)dp and ^{2}H(d,n)ppn reactions.

The target area was shielded from the deuterium gas cell by a multi-layered wall composed of concrete, steel, iron, lead and paraffin (see left side of Fig. 3.4). This wall shielded the target area from most background (particles that do not interact with the scatterer) neutron and gamma radiation produced at the gas cell. As shown in Fig. 3.4 an opening with a rectangular cross section allowed neutrons produced in the gas cell at $\sim 0^{\circ}$ to reach the center detector located on the opposite side of the shielding wall at a distance of 1.7 m. The opening was fitted with a double-truncated collimator. The collimator walls were made from tapered rectangular copper and polyethylene bars. The collimator has three segments, one for each taper, and four bars make up the walls of the collimator. Each bar was tapered in such a way that the part of the bar illuminated by the gas cell cannot be seen by the scatterer, while the part of the collimator facing the center detector cannot

be seen from the gas cell. This minimized the number of in-scattered neutrons impinging on the scatterer while allowing the scatterer to be exposed to a spatially homogeneous field of unscattered neutrons from the gas cell.

3.3 Detector Types

3.3.1 Center Detector

The center detector consists of a glass right cylinder 6 cm high and 4 cm in diameter filled with C_6D_{12} liquid scintillator (NE-232)[1]. The density of the deuterated scintillator is 0.96 g/ml, and it has a ratio of deuterium to carbon of 1.96. There is a small expansion chamber on the side of the cylinder. Neutrons from the gas cell incident on NE-232 may interact with deuterons through elastic scattering or the breakup reaction. The resulting charged particles (deuterons or protons) travel some distance within the center detector's active volume and lose kinetic energy, exciting the molecules in the NE-232 to states from which they decay in a matter of 2 to 3 nanoseconds while emitting light in the ultraviolet end of the spectrum with an intensity proportional to the energy deposited by the charged particles.

The exterior of the glass cylinder is covered with reflector paint except for the bottom surface, where light is allowed to escape. The cylinder rests on top of the window of an RCA 8575 photo-multiplier tube (PMT). The scintillator cell is optically coupled to the PMT with a film of BC-630 optical grease which matches the index of refraction of the glass cylinder to that of the PMT window. The PMT converts the flashes of light of the scintillator into electric current whose amplitudes are proportional to the light intensity.

[1]NE-232 is a trade name of Nuclear Enterprises, Edinburgh, Scotland

3.3.2 Neutron Detectors

Three types of neutron detectors were used in this experiment: Ring, Argonne and Bicron. A diagram of the three types of detectors is shown in Fig. 3.3. These detectors differ in shape, volume and type of liquid scintillator used. The Ring detectors were built at TUNL and filled with (NE-213)[2] liquid scintillator in an argon atmosphere to prevent oxygen contamination and loss of pulse-shape particle identification. The Argonne detectors were built at Argonne National Laboratory and filled at TUNL with (BC-501)[3] liquid scintillator in identical manner as the ring detectors. The Bicron detectors were ordered from Bicron Corporation. They are bubble-free aluminum cells filled with BC-501A liquid scintillator fluid.

The front view of a Ring detector is shown at the bottom of Fig. 3.3. They consist of a fluid cell built from two concentric 4 cm long cylinders. The inner diameter of the scintillator fluid cells is 7.6 cm, and the outer diameter is 13.44 cm. The inner wall is made of 1.5 mm thick aluminum, while the outer wall is made of 3.2 mm thick glass. The front and back of the detector is capped with 1 mm thick aluminum plates, which are attached to the cylinder ends with Torr Seal epoxy. The Torr seal epoxy was used because the liquid scintillators are not solvents for it, unlike most other epoxies. The end plates are annular in shape with an inner diameter of 7.3 cm and an outer diameter of 14.04 cm (see Fig. 3.3). A small filling pipe and a Teflon tube, used as an expansion chamber, are attached to the front and back plates, respectively. The inside of the fluid cell is coated with (BC-624)[4] reflector paint, except for two windows that allow light to be transmitted through lucite light guides into the PMTs. Four Ring detectors were placed at a distance of 1.5 m from the center of the deuterated scintillator at $43.0^\circ, 35.5^\circ, 28.0^\circ$, and 20.5° from the beam axis. They were used for the detection of neutron 1 in the *np* FSI measurements.

Five Bicron detectors were used in this work. The Bicron detector fluid cells are

[2]NE-213 is a trade name of Nuclear Enterprises, Edinburgh, Scotland
[3]BC-501 is a trade name of Bicron Corporation, Newbury, Ohio
[4]BC-624 is a trade name of Bicron Corporation, Newbury, Ohio

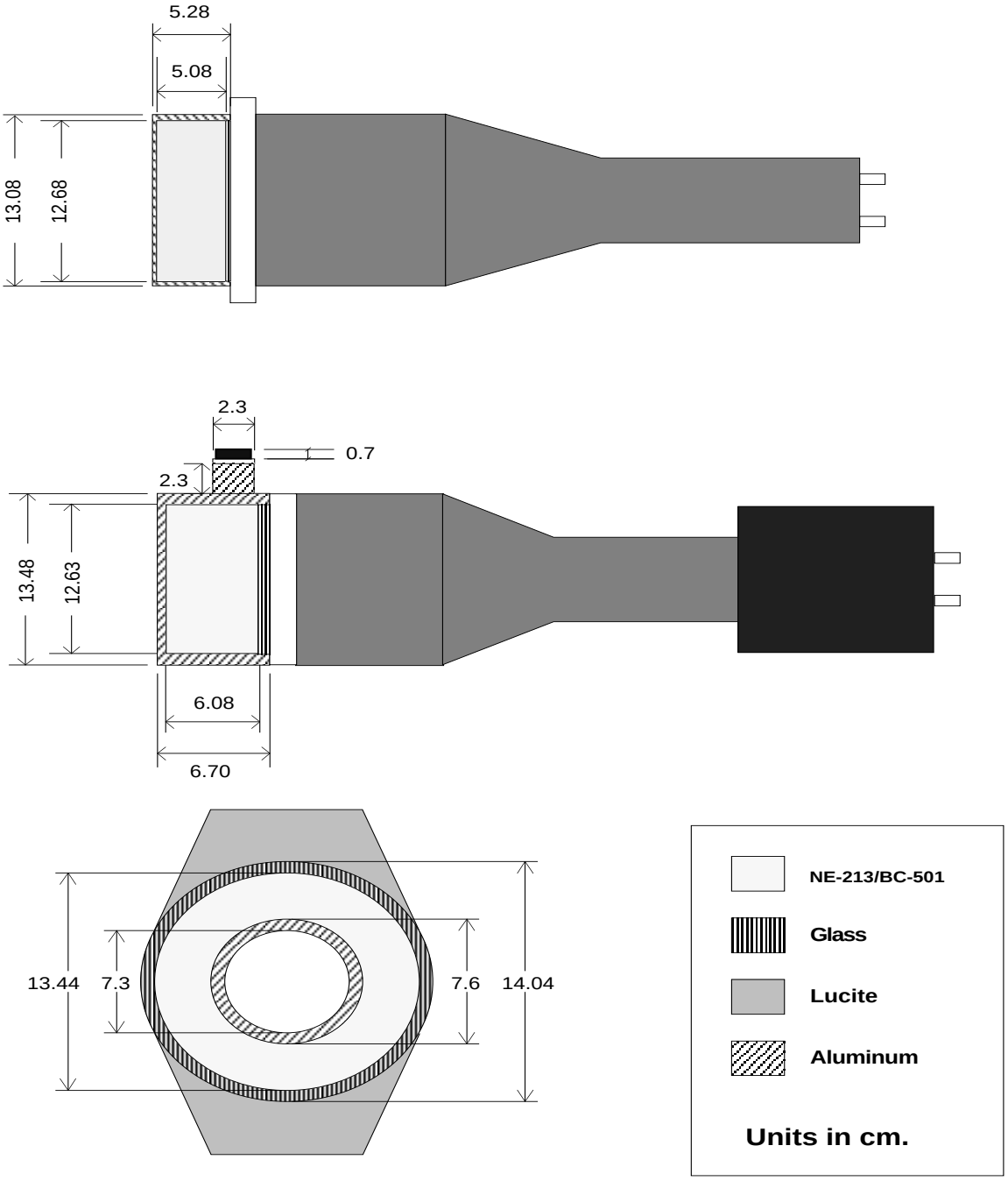

Figure 3.3: Dimensions of the three detector types used in the *np* FSI cross section measurements.

simple aluminum cylinders where one of the ends is a glass window and the opposite end is a 1 mm thick aluminum plate. The inner radius is 6.34 cm and the interior depth is 5.08 cm. The Bicron detector cells are bubble free. In the bubble free design, a long Teflon tube is coiled around the cell. The tube is partially filled with scintillator fluid, and functions as a fluid reservoir for the cell. A cross-sectional view of a Bicron detector is shown at the top of Fig. 3.3. These cells were mounted directly on the window of a PMT with optical grease between the glass surfaces.

Four of these detectors were placed at 2.5 m from the center of the deuterated scatterer at the same angles as the Ring detectors, covering the solid angle of the hole of the ring. The Bicron and Ring detectors were placed in this arrangement to measure the cross section of four nn FSI angles for the extraction of a_{nn}. The details of this experiment can be found in [GT97]. The two experiments were carried out simultaneously. The fifth Bicron detector is placed at 1.296 m, $\theta = 100.5^\circ$, and $\phi = 180.0^\circ$ to measure neutron 2 from the np FSI at 20.5°. The angles θ and ϕ are the normal polar and azimuthal scattering angles. The polar angles are indicated in Fig. 3.4.

The Argonne detectors are of very similar design as the Bicron detectors. One primary difference is that the Argonne detectors have an argon gas bubble trapped inside the cell to permit fluid expansion. A cross-sectional view of an Argonne detector is shown in Fig. 3.3. The Argonne detectors are aluminum cylinders with 0.39 cm walls. The front face of the cell is 0.28 cm thick. The bottom glass plate is 0.3 cm thick. The interior is also coated with reflective paint. A 5.0 cm thick plastic light guide is used to couple the scintillator cell to the 12.6 cm diameter spherical window of a PMT. The cell has a cubic aluminum snout of 2.3 cm on each side that is used for filling the detector. The fill hole is sealed with a brass bolt and a Teflon washer. The three Argonne detectors were placed at $\phi = 180.0^\circ$, $\theta = 83.5^\circ, 69.0^\circ$, and 55.7° to detect neutron 2 from the np FSI configurations at $\theta = 28.0^\circ, 35.5^\circ$, and 43.0°, respectively. The centers of these detectors were placed at distances of 1.486, 1.821, and 2.059 m, respectively, from the center of the deuterated

Table 3.1: Some basic properties of NE-213 and BC-501(A) scintillators.

Scintillator type	density(g/ml)	Hydrogen/Carbon ratio	Wave length of maximum light emission (nm)
NE-213	0.874	1.213	425
BC-501(A)	0.901	1.287	425

scintillator. The distances were the farthest possible, constrained by the presence of a beam pipe in the target area.

The Ring detectors were filled with NE-213 liquid scintillator fluid. The Bicron and Argonne detectors use BC-501 and BC-501A fluids (see Table 3.1), respectively. These organic liquid scintillators are similar to the NE-232 used in the center detector, except that they contain hydrogen instead of deuterium. Also, they allow pulse-shape discrimination (PSD) between detected gammas and neutrons, see Table 3.1.

3.3.3 Layout of Detectors

Eight *np* FSI configurations were investigated using twelve neutron detectors deployed as shown in Fig. 3.4. The cross section for each *np* FSI angle was measured by detecting neutron 1 in either a Ring or Bicron detector, and neutron 2 in a Bicron or Argonne detector. In Fig. 3.4, the detectors used to detect neutrons 1 and 2 from the same *np* FSI angle are joined by lines of the same type.

All detectors were mounted on aluminum holders and placed on iron stands bolted to the concrete floor. All detectors have their height adjusted so that the center of their faces are on the plane of the neutron beam (about 1.77 m from the lab floor).

Table 3.2 shows the configurations of interest.

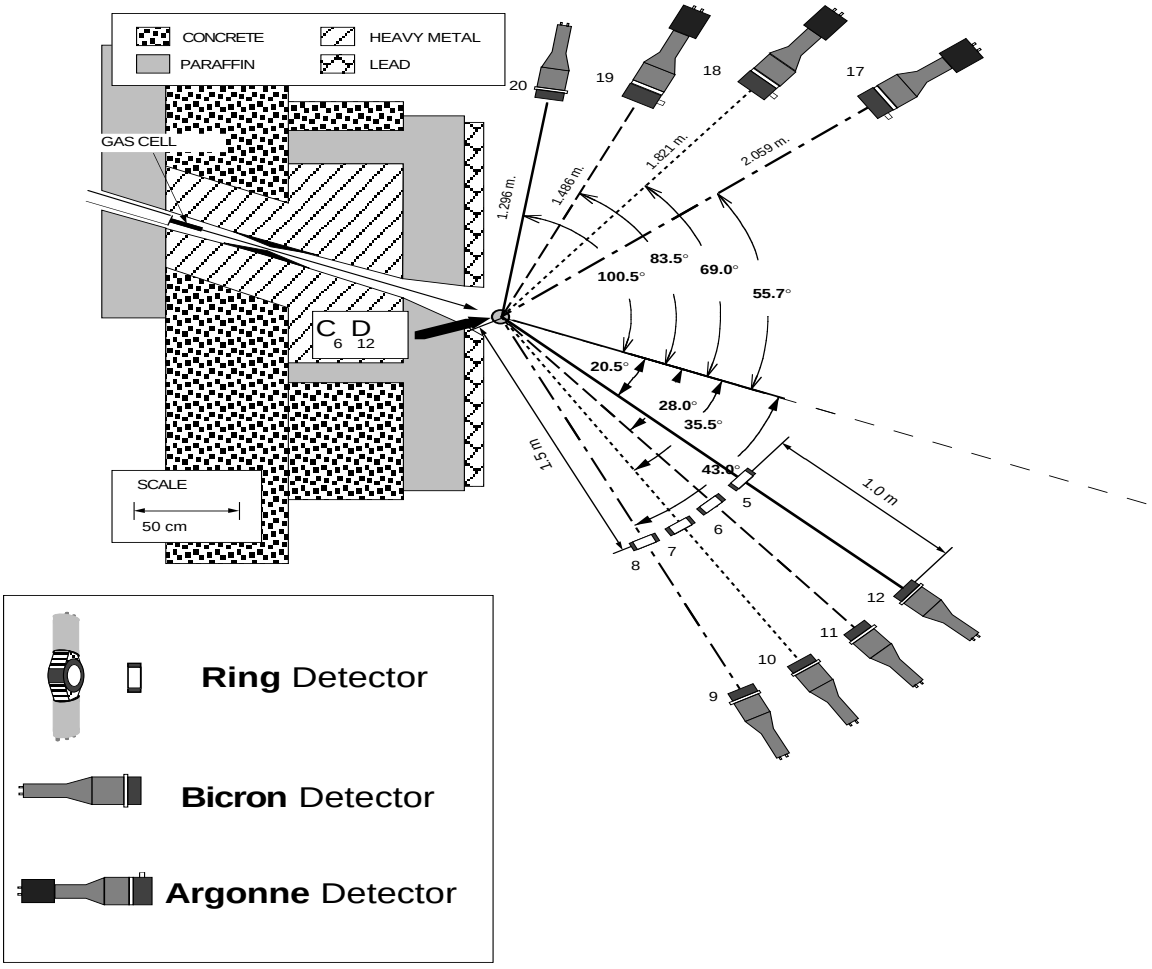

Figure 3.4: Detector layout for the *np* FSI cross section measurements in *nd* breakup at the TUNL shielded neutron source experimental area. Detectors used in the same *np* FSI production angle are joined by lines of the same type. The distances are measured from the center of the first detector to center of the second.

Conf.	neutron 1			neutron 2		
Name	θ_1	dist. (m.)	type	θ_2	dist. (m.)	type
npfsr1	43.0°	1.504	Ring	55.7°	2.059	Argonne
npfsr2	35.5°	1.498	Ring	69.0°	1.821	Argonne
npfsr3	28.0°	1.494	Ring	83.9°	1.486	Argonne
npfsr4	20.5°	1.504	Ring	100.5°	1.296	Bicron
npfs1	43.0°	2.491	Bicron	55.7°	2.059	Argonne
npfs2	35.5°	2.487	Bicron	69.0°	1.821	Argonne
npfs3	28.0°	2.497	Bicron	83.9°	1.486	Argonne
npfs4	20.5°	2.492	Bicron	100.5°	1.296	Bicron

Table 3.2: Detector setup for *np* FSI measurements at four angles defined by θ_1. All flight-path lengths are center-to-center distances.

3.4 Detector Electronics

3.4.1 Neutron Detectors

The signals from two neutron detectors were processed through the same electronics because of the limited availability of PSD NIM modules, and TDC and ADC channels. So for the twenty neutron detectors used in the *np* FSI and *nn* FSI measurements only ten sets of electronics were needed. Fig. 3.5 shows the detection electronics for detector pair #1, which consisted of detectors one (used in the a_{nn} measurement only) and five. A list of the electronic pairs is given in table 3.3.

Both the anode and the dynode signal of the neutron detectors were used in the electronic data acquisition circuit. The dynode signals of the neutron detectors were integrated by Ortec 113 or by TUNL preamplifiers. The two dynode signals from a Ring detector were summed either passively at the end of the two 60 cm long cables just before the input of an Ortec 113 preamplifier, or actively through the double inputs of a TUNL preamplifier. The output of the preamplifiers was then combined in pairs as explained above. The resulting integrated signal was amplified and shaped, and then was sent to an Analog-to-Digital Converter (ADC) to be used for pulse-height analysis.

Table 3.3: Electronic pair assignment.

Electronic Pair #	**Detectors**
1	1,5
2	2,6
3	3,7
4	4,8
5	9,13
6	10,14
7	11,15
8	12,16
9	17,19
10	18,20

Ring detectors have two PMTs whose anode signals were summed passively in the target area using a "T" coaxial junction. The anode signal from each neutron detector was first split by a "magic tee". A "magic tee" is a voltage divider used to keep the impedance matched in the two branches the signal is split into. One output was sent to a constant-fraction discriminator(CFD), and the other one was actively summed in a LeCroy 428 with the anode signal from the other detector in the pair. The output from the linear fan was the input of a pulse-shape-discriminator (PSD) module. One of the outputs from the CFD was sent to the TDC as a stop signal. The TOF signals were not paired, each individual detector had a TDC stop. The second output of the CFD of both detectors in a pair was sent to a logical OR module. One of the outputs of the OR module was used to strobe the PSD module. The output of the PSD module was then sent to the TDC as a stop signal. The other output of the logical OR module was sent to a logical AND module with the CFD output of the center detector. The center-neutron detector coincidence signal was used to build the event trigger. A schematic of the circuit for the neutron detectors is shown in

Fig. 3.5.

The anode signals from the neutron detectors were also used to set a hardware low-level threshold by adjusting the threshold setting in the CFD. This threshold was always set well below one-third of the pulse height of the Compton edge of ^{137}Cs and could be adjusted for each detector independently.

3.4.2 Center Detector

The anode signal of the center detector (CD) provided timing information from breakup and elastic scattering events. The CD anode signal was taken into a CFD. The CFD output was the time reference for the event trigger, and the "start" pulse for the TDC. The CFD threshold was typically set below one-tenth of the pulse height for the Compton edge of a ^{137}Cs gamma source.

Pulses from two gain stages in the PMT (Low and High) were necessary to cover the full range of CD pulse heights of interest. Pulses from the tenth and eleventh dynodes were independently amplified and selectively passed to the ADCs using a fast linear gate. The gate signals for the linear gate module were derived from the event trigger, denoted as "coincidences" in Fig. 3.7. This circuit reduced the frequency of CD linear signals from $\sim$ 400 kHz down to $\sim$ 400 Hz at the computer interface. Finally, the gated linear High and Low gain pulses were amplified and shaped (shaping time constant was set to 1 μs) and then were digitized by the ADCs.

The trigger circuit was set up to run in "beam" or "source" mode. In "source" mode the detector CFD signals (the single OR (SOR) logic signals) were used as the coincidence-center detector (CCD) signals to be used to form the event trigger. In "beam" mode the real CCD signals form the trigger. The switching between the real CCD signals and the SOR signals was done using the negative DC signal from the source/beam module, see Fig. 3.6. In the "source" mode every stop signal from the neutron detectors generates a computer trigger start and events are accepted without fulfilling the CD coincidence requirement. This

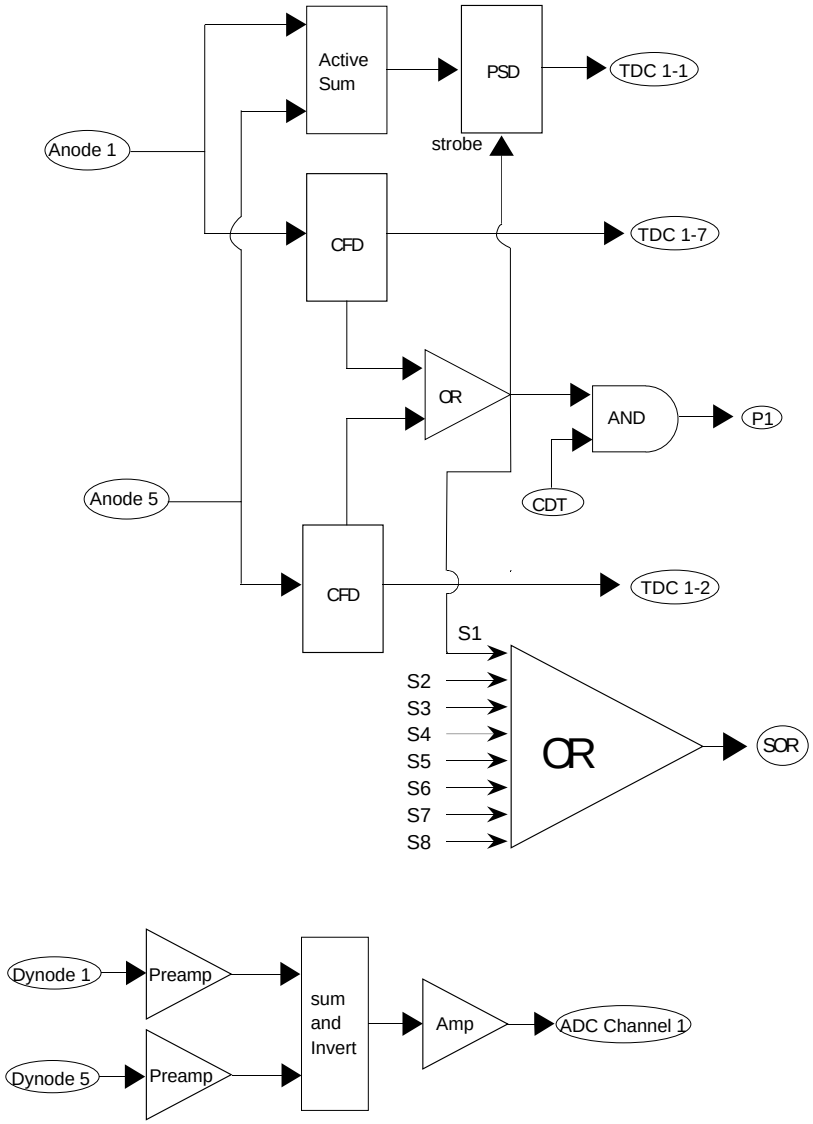

Figure 3.5: Simplified electronics diagram for neutron detector electronic pair #1.

mode was used to accumulate ^{137}Cs pulse-height spectra for every neutron detector every twelve hours. The stability of each neutron detector gain was monitored by determining the Compton edge of its ^{137}Cs pulse-height spectrum.

When running in "beam" mode, the center detector's CFD output was combined in a logical AND with the OR of the CFD signals of all neutron detectors. This introduced the requirement that any input signal for the computer trigger must be a coincidence between the center detector and at least one neutron detector. Changing between "beam" and "source" mode was done by means of a switch at the source/beam module.

3.4.3 Computer Trigger

The computer trigger circuit provided common start signals and gates for the TDCs and ADCs. The output of the trigger coincidence circuit was used by the fast linear gate modules to select CD linear signals.

The logical AND between the paired output of the neutron detector CFDs and the center detector CFD, referred to in Section 3.4.1, was the input to the trigger circuit. Pairs 1 through pair 4 were combined into a logical OR group. The same was done with pairs 5 through pair 8, and a third OR group was used for pairs 9 and 10 (see Fig. 3.7). All triple coincidences of interest (np FSI) occurred between two neutron electronic pairs not belonging to the same logical OR group.

The output signals from these three OR groups were either combined in a majority logic AND (for n-n-p triple coincidences) or a logical OR (for n-d double coincidences). When a triple coincidence was registered, the associated double-coincidence signals were vetoed so as not to double count an event as both a triple and a double-coincidence.

Double-coincidence events resulting from nd elastic scattering have a very large rate, which would introduce an unacceptably large dead time in the data-acquisition system. To deal with this problem, it was necessary to implement a divide-down circuit (see Fig. 3.7). A gate generator was used to widen the logical signal triggered by a double-coincidence

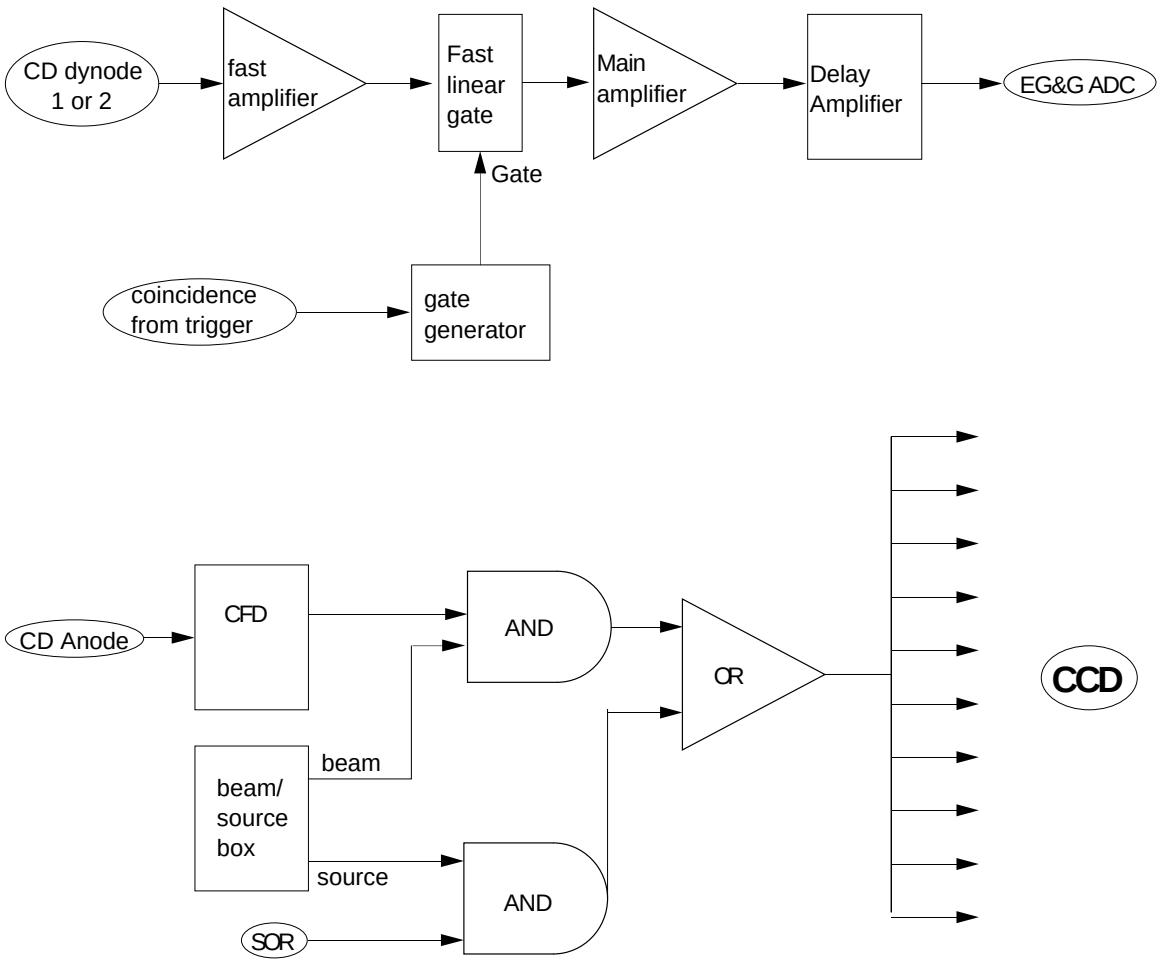

Figure 3.6: Electronics diagram for the center detector.

event, thus introducing an adjustable dead time which allowed us to regulate the rate of triggers from double-coincidence events. Two scalers were used to count the number of events before and after the divide-down circuit. The ratio of these two numbers gave the scale factor for double-coincidence events. The divide factors for the double-coincidence triggers during the experiment varied from ~ 18 to ~ 32.

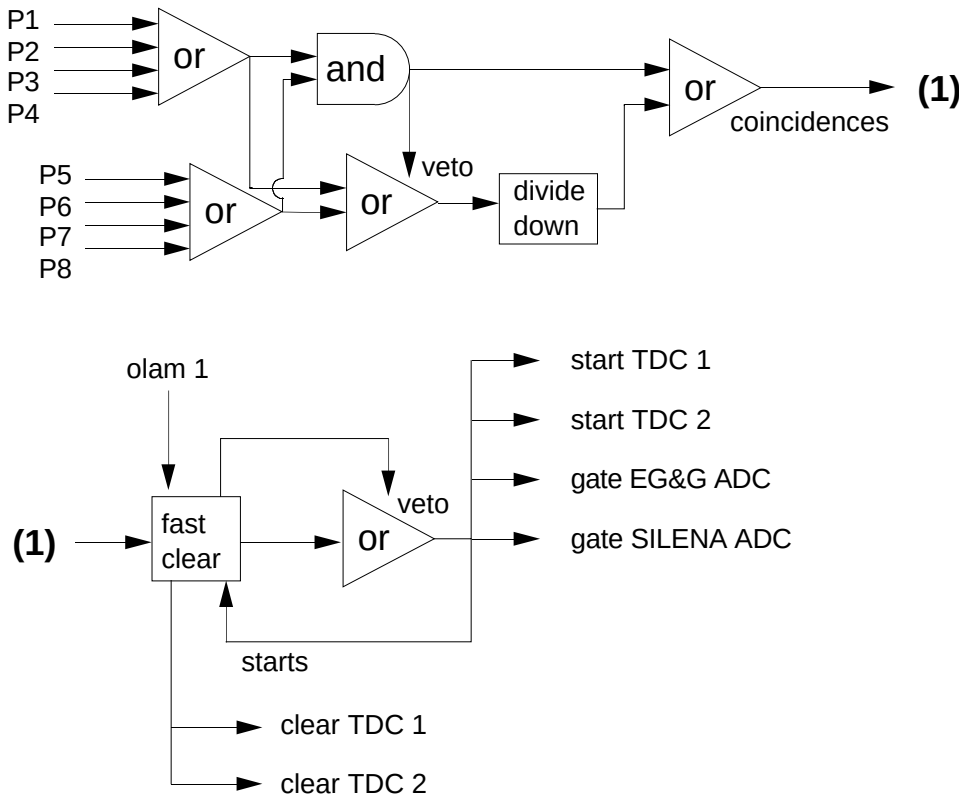

Figure 3.7: Simplified diagram of the computer trigger electronics.

A fast-clear circuit was implemented to insure that after every registered event, the TDCs were properly reset (see Fig. 3.8). The rise of the trigger veto signal was initiated by the TDC start signal. The OLAM signal, was set when the fastest digitizer had finished its processing, see Section 3.4.4, and was reset when all digitizers had been read and cleared. The fall of the OLAM signal was used to generate a hardware clear signal for resetting each

TDCs hit and data registers.

An LED pulser system was set up to determine the dead time losses for double- and triple-coincidence events (see Fig. 3.9). Two independent LED pulser drivers were used. The rate of each driver was about $\sim$ 6 Hz. Double-coincidence pulser events were obtained by simultaneously flashing the LED in the center detector and in neutron detector 9. Triple-coincidence pulser events were produced by simultaneously flashing the LED in the center detector, and in detectors 20 and 12. Trigger signals from both pulser drivers were sent to separate scaler channels.

Not all detectors were built to accept LED pulses. Therefore, in order to measure the dead time, ten electronically generated pulses were fed into the circuit right before the TDCs and ADCs, simulating time-of-flight, PSD and pulse-height signals for one detector in each pair. By counting the number of pulses processed by the computer and comparing them to the number of pulses counted by a scaler, a measurement of the TDC, ADC, and computer dead time was made. From comparisons between this dead time and the dead time measured using the LED pulsers, it was found that about 99.5% of the dead time was due to the data acquisition system (digitizers and computer interface).

3.4.4 CAMAC Electronics

TDCs and ADCs in a CAMAC (Computer Automated Measurements and Control) crate were used for data digitalization. Table 3.4.4 shows the arrangement of stop signals for time-of-flight (TOF) and PSD measurements made with two Phillips 876 TDCs. The trigger circuit provided the common start signal for the TDCs and master gates for the ADCs. The stop signals to the TDCs came from the neutron detector CFDs for the TOF measurements, and from the PSD modules for the pulse-shape measurements used for gamma-neutron identification.

A LAM (Look At Me) signal was raised by the TDCs or ADCs after conversion. The data-acquisition software can be configured to specify a particular combination of

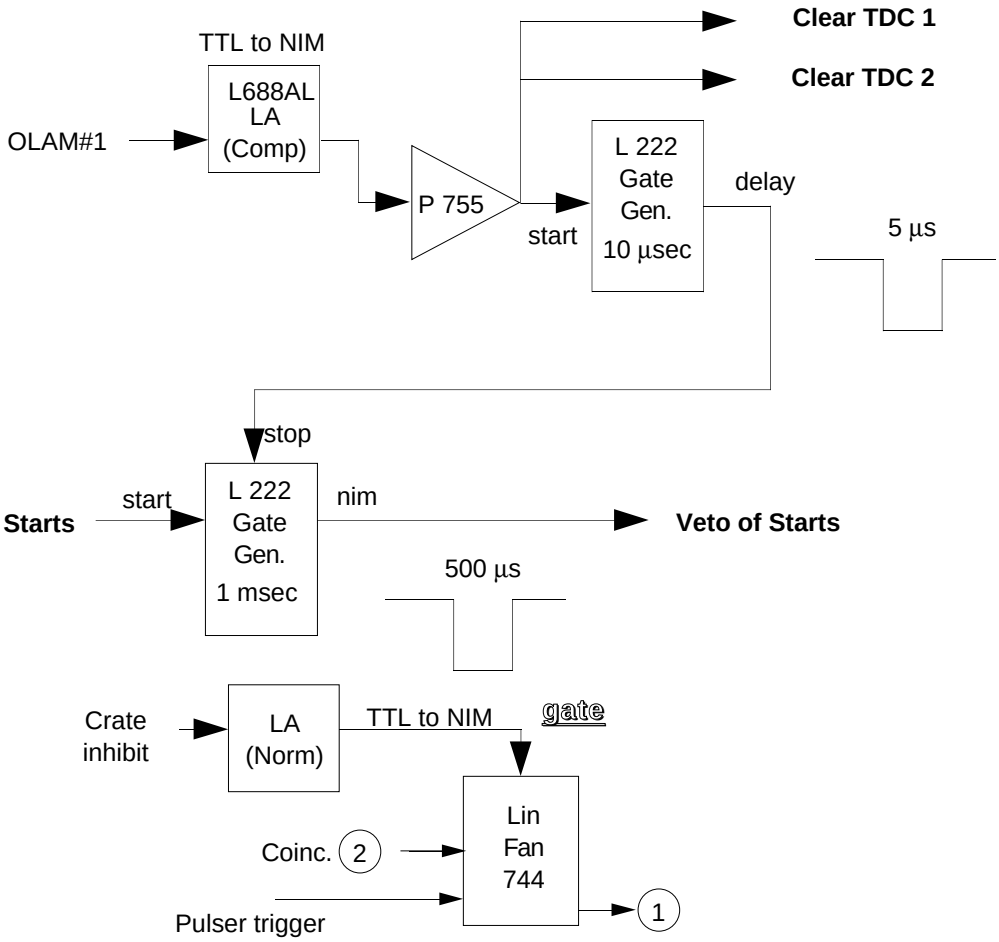

Figure 3.8: Fast-clear circuit for TDCs and trigger veto circuit.

Table 3.4: TDC configuration for TOF and PSD stop signals. The PSD signal number is the detector pair number (listed in Table 3.3), and the TOF signal number is the detector number given in Fig. 3.4.

TDC	TDC 1		TDC 2	
slot	PSD signal	TOF Signal	PSD signal	TOF signal
1	1		2	
2	3		4	
3	5		6	
4	7		8	
5	9		10	
6		Puls		Puls
7		1		2
8		3		4
9		5		6
10		7		8
11		9		10
12		11		12
13		13		14
14		15		16
15		17		18
16		19		20

LAM signals to constitute a valid trigger. For this experiment, LAM signals from any of the digitizers constituted a valid trigger for the computer read out. Once a valid computer trigger was generated, start signals were vetoed by the OLAM signal. The computer read out code then checked that the event had a valid conversion in at least one of the two TDCs before proceeding to execute the data read out list. If there were no hits in either TDC, the event was rejected. Once the OLAM signal fell, the fast-clear circuit reset both TDCs. A 5 μs delay followed to allow the TDCs enough time to reset before the trigger veto circuit allowed the next event signals to pass to the computer interface for digitization.

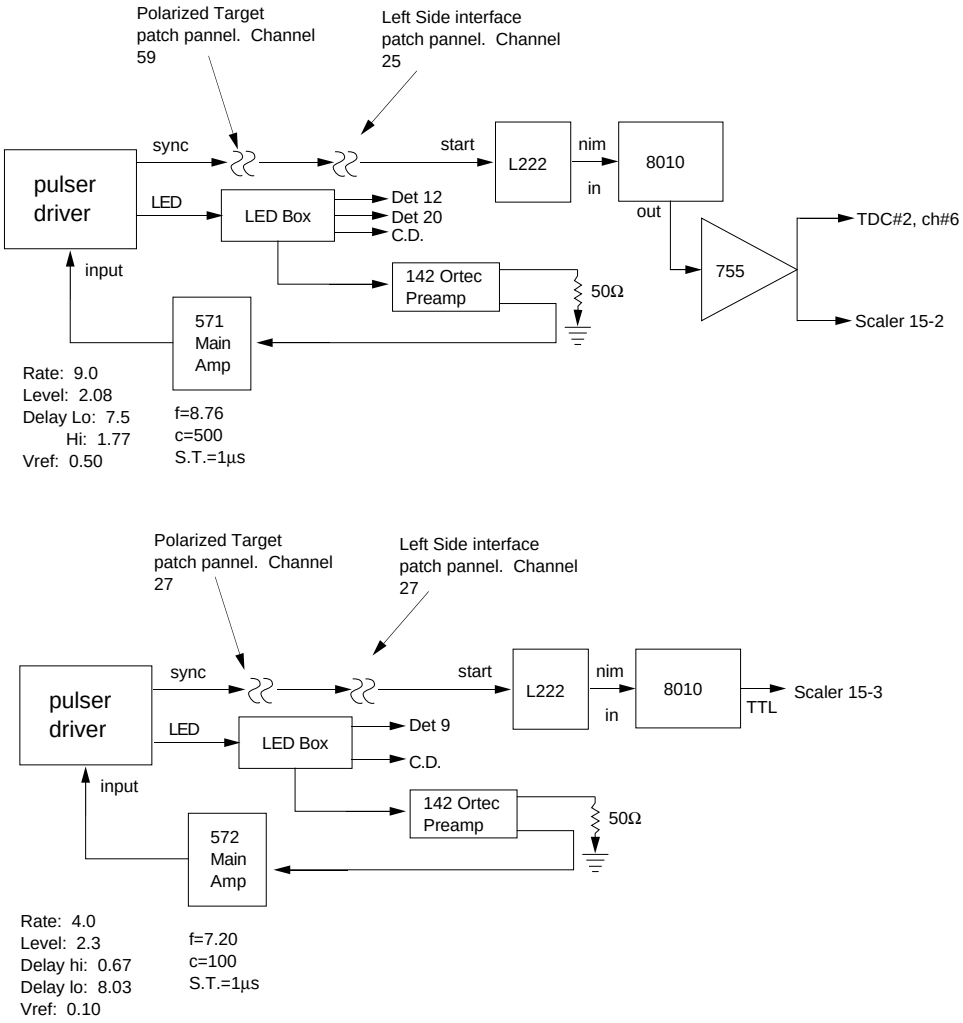

Figure 3.9: Electronic diagram for the LED pulser.

Chapter 4

Monte-Carlo Simulations

4.1 Introduction

The value of a_{np} was determined by fitting the measured cross sections for np FSI with the theoretical cross sections using a_{np} as the search parameter in a χ^2 analysis. To make legitimate comparisons between theory and data, complete simulations of the experiment for nd elastic scattering and nd breakup were performed. The simulations were based on Monte-Carlo (MC) techniques and used the point-geometry cross sections from rigorous three-nucleon (3N) calculations [Glö96]. A separate FORTRAN code was written to simulate each of the two processes, i.e. nd elastic and nd breakup . The codes were used:

1. To calculate the background in the center-detector (CD) pulse-height spectrum due to neutron multiple scattering (MS) in the CD for nd elastic scattering.

2. To simulate experimental spectra by accounting for finite-geometry and energy resolution effects of the experimental setup; and

3. To calculate theoretical np FSI cross sections for different values of a_{np} including finite-geometry and energy-resolution effects of the experimental setup.

The parameters in the energy and time resolution functions used in the simulations were adjusted to fit the experimental data. Once the simulated spectra were in good agreement with the experiment, simulations were run to high statistical precision. The simulated spectra were used to impose kinematic cuts on the events.

Because of the large energy spread in the incident neutron beam, about 400 keV, and the large angular acceptance of the detector system, $\Delta\theta \sim 9.0^\circ$ and $\Delta\phi \sim 10.0 - 16.0^\circ$, an extensive library of point-geometry cross sections were required for the simulations.

4.2 Cross-Section Libraries

Extensive libraries were created of differential cross sections for *nd* breakup covering the kinematic regions of the eight *np* FSI configurations measured in our experiment. The library stored cross sections at about 10^5 grid points. Each point is specified by E_0 the incident neutron beam energy, θ_1 the angle of neutron 1, θ_2 the angle of neutron 2, ϕ_{12} the azimuthal angle between the neutrons, E_1 the energy of neutron 1, E_2 the energy of neutron 2, and E_3 the proton energy.

A similar library was made for *nd* elastic scattering simulations. Of course, since *nd* elastic scattering is a two-body process, fewer grid points were needed to cover the full experimental acceptance and resolution than in the case of *nd* breakup . The library for *nd* elastic scattering contained about 500 grid points. Each point was specified by E_0 the incident beam energy, and θ_n the angle of the elastically scattered neutron.

We first describe the library used in the simulations of the *nd* breakup process. Differential cross sections were generated along kinematic S-curves for *nd* breakup configurations determined by the *np* production angles $\theta_1, \theta_2, \phi_{12}$, and the incoming neutron beam energy E_0. The cross sections were computed as a function of S, the distance along the kinematic curve.

The differential cross section $\frac{d^3\sigma}{d\Omega_1 d\Omega_2 dS}(S)$ is given as a function of the S-curve length in steps of 0.1 MeV, always starting at the point where $E_2 = 0$ MeV. The differential cross

Table 4.1: Values for σ-meson coupling constants and associated effective-range parameters.

$g_\sigma^2/4\pi$	a_{np} (fm)	r_{np} (fm)
8.6023	-10.0	3.06
8.6543	-11.0	3.00
8.6980	-12.0	2.96
8.7353	-13.0	2.92
8.7676	-14.0	2.88
8.7957	-15.0	2.85
8.8204	-16.0	2.83
8.8423	-17.0	2.81
8.8620	-18.0	2.79
8.8796	-19.0	2.77
8.8955	-20.0	2.76
8.9099	-21.0	2.74
8.9231	-22.0	2.73
8.9351	-23.0	2.72
8.9462	-24.0	2.71
8.9564	-25.0	2.70
8.9659	-26.0	2.69
8.9747	-27.0	2.68

section has a characteristic enhancement in the neighborhood of the S-curve point where $E_1 = E_3$. This enhancement is very sensitive to the $^1S_0$ part of the np interaction [Wit96]. The Bochum-Cracow group prepared a code that uses the Faddeev scheme to rigorously calculate the nd breakup differential cross sections based on the Bonn-B OBEPQ NN potential. The σ-meson coupling constant $g_\sigma^2/4\pi$ was modified in the code to alter the $^1S_0$ component of the np interaction, yielding different values of a_{np} (see Table 4.1 [Tor96]) while keeping the nn part of the interaction fixed using $a_{nn} = -17.7$ fm. All NN force components with total two-body angular momentum $j \leq 3$ are considered.

For each of the four experimental np FSI production angles measured in the present

Table 4.2: Angular span of *np* FSI libraries due to the finite geometry of the experimental setup.

configuration	θ_{np}	$\theta_1(^\circ)$	$\theta_2(^\circ)$	$\phi_{12}(^\circ)$	$\Delta\theta_1(^\circ)$	$\Delta\theta_2(^\circ)$	$\Delta\phi_{12}(^\circ)$
npfsr1	43.0	38.5–47.5	52.2–59.2	170-180	2.0	1.75	2.5
npfsr2	35.5	31.0–40.0	65.5–72.5	170-180	1.8	1.17	3.7
npfsr3	28.0	23.5–32.5	79.0–88.0	165-180	1.3	1.13	4.3
npfsr4	20.5	16.0–25.0	96.0–105.0	164-180	1.3	1.80	4.5

work, cross-section libraries were created for $a_{np} = -22.0$, -23.0, -23.75, and 25.0 fm. The following experimental factors were taken into account:

1. The library covered the full angular range due to the finite geometry of the experimental setup, given by the possible extreme values of θ_1, θ_2, ϕ_{12} (see Table 4.2).

2. Cross-section values for $E_0 = 12.8, 13.0$ and 13.2 MeV were calculated in order to account for the energy spread in the neutron beam produced in the gas cell.

3. The angle and the incoming-neutron energy were chosen so that the variation in the cross section between adjacent grid points (angle or energy) was less than 4%.

The calculation of all the libraries took approximately 70 hours of CPU time on Cray Y-YMP and T90 super computers[1].

4.3 Monte-Carlo Codes

4.3.1 *nd* elastic Scattering

The accurate measurement of yields for *nd* elastic scattering is of central importance in determining *nd* breakup cross sections. In our technique, the target-beam luminosity, β, was used to determine the cross section from the measured yields for *nd* breakup . The

[1]MCNC, Research Triangle Park, NC-27709-2889

β was determined from the yields from nd elastic scattering. The nd elastic yields Y_{el} are related to the nd elastic cross section by the following expression:

$$Y_{el}^{r} = (\frac{d\sigma_{lab}}{d\Omega}(\theta))\alpha(E_{el})\varepsilon(E_{el})\beta[BCI]_{r}d\Omega, \tag{4.1}$$

where

$$\beta = \frac{N_{n}^{r}N_{d}}{[BCI]_{r}}. \tag{4.2}$$

The N_{n}^{r} is the number of neutrons that hit the deuterated target, N_{d} is the number of deuterons in the target, and $[BCI]_{r}$ is the total charge deposited by the deuteron beam on the deuterium gas cell during the run r. The quantity $\alpha(E_{el})$ is the transmission probability of the elastically-scattered neutrons with energy E_{el}, taking into account the neutron attenuation in the deuterated scatterer, and in air. The $\varepsilon(E_{el})$ is the absolute detection efficiency of the neutron detector for scattered neutrons with energy E_{el}. The solid angle subtended by the neutron detector is denoted $d\Omega$. The nd elastic scattering differential cross sections $\frac{d\sigma_{lab}}{d\Omega}(\theta)$ are well established for the energy and scattering angles of our experiment [Wit89]. Once the yield Y_{el}^{r} has been determined from the experimental spectra, β can be found using Equation 4.1. In Chapter 5 we show how β is used to normalize the nd breakup yields to obtain absolute cross sections.

Because of the finite size of the deuterated target, it is possible for neutrons to elastically scatter more than once within the target. These multiply-scattered (MS) neutrons and the singly-scattered (SS) neutrons cannot be resolved completely by time-of-flight (TOF). Hence, the MS neutrons form a background beneath the prominent SS peak in the TOF spectrum (see Fig. 4.1) and the associated CD pulse-height spectrum (see Fig. 4.2). A MC code was written to simulate the MS neutron contribution to the experimental neutron TOF and CD pulse-height spectra for nd elastic scattering. In addition to simulating the MS events the following effects were modeled in the code:

1. The time resolution of the neutron detectors;

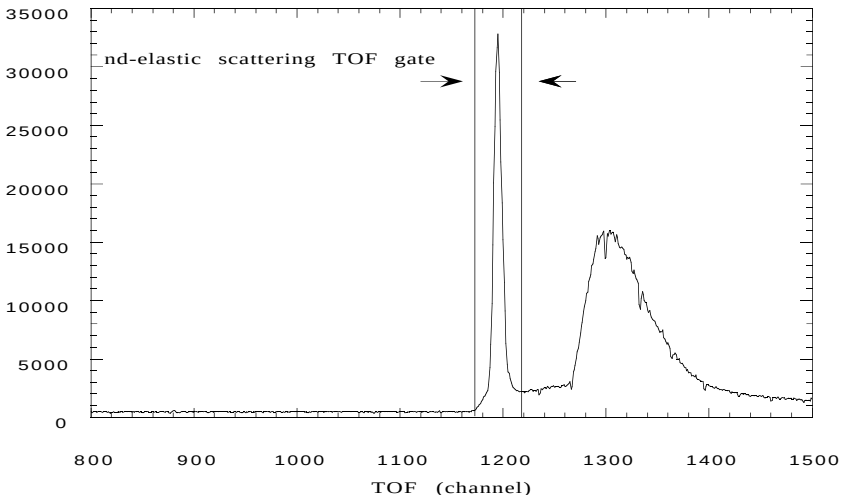

Figure 4.1: Time-of-Flight spectrum associated with detector 9 showing the gated *nd* elastic scattering peak. The resolution of the spectrum is 0.2 ns/channel.

2. the energy resolution of the CD;

3. finite-geometry effects due to the size of the CD and of the neutron detectors;

4. edge effects in the CD; and

5. the energy spread in the incident neutron beam.

The method used to extract the yields from the experimental spectra is described in Section 5.2.

4.3.2 *nd* breakup

The *nd* breakup experimental data inherently incorporates effects due to the finite pulse-height resolution of the center detector, the neutron detection efficiency, the attenuation of neutrons as they pass through the scatterer and in their flight through air, the time

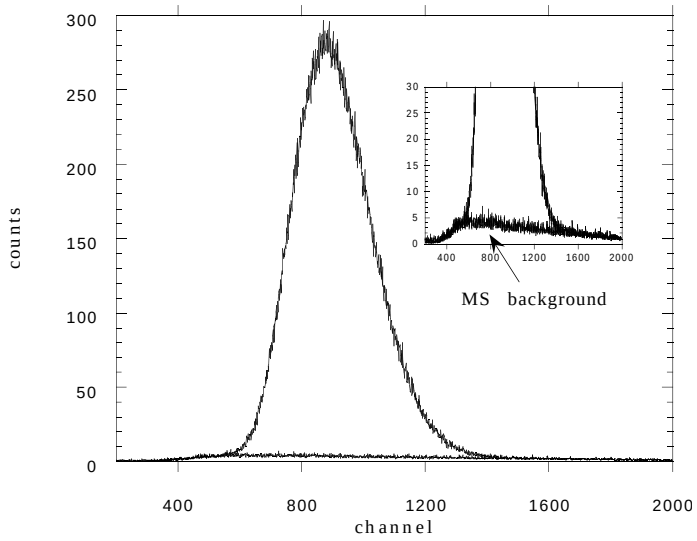

Figure 4.2: MC Center Detector pulse-height spectrum associated with the *nd* elastic scattering TOF peak of detector 9. The ratio of multiple-scattering to single-scattering counts is $\sim 1:12$ for all scattering angles observed.

resolution of the detectors, and the finite size of neutron detectors and the scatterer. Instead of trying to unfold these effects from the experimental data to extract point-geometry cross sections for *nd* breakup , we elected to fold these effects into the theoretical predictions. The effects were modeled in a full simulation of the experiment. The end result of the simulations were theoretical predictions that could be compared directly to the experimental data and the parameters needed to compute cross sections from the measured yields. Using E_1, E_2 and E_3 for the energies of the breakup neutron 1, neutron 2 and the proton, respectively, the simulations were used to compute:

1. the product of the transmission probabilities of both *nd* breakup neutrons emitted to the neutron detectors (neutron transmission product)

$$\bar{\alpha}(E_1, E_2, E_3) = \alpha_1(E_1)\alpha_2(E_2); \tag{4.3}$$

2. the absolute neutron detection efficiency product

$$\bar{\varepsilon}(E_1, E_2, E_3) = \varepsilon_1(E_1)\varepsilon_2(E_2); \tag{4.4}$$

3. the weight factor

$$\bar{\omega}(E_3) = \omega(E_3) \tag{4.5}$$

   to simulate the energy resolution of the center detector; and

4. the finite-geometry theoretical differential cross section $\frac{d^3\sigma_t}{d\Omega_1 d\Omega_2 dS}(E_1, E_2, E_3)$.

Only events in which the neutrons undergo single-scattering were considered in the simulation. Multiple-scattering events do occur but their effects are very small. This is because as was found in *nd* elastic only about 8% of the neutrons scatter more than once. Furthermore, the event does not belong to an *np* FSI kinematic configuration, so the cross section is greatly reduced. Additionally, the particle energies of very few MS events will meet all the kinematic constraints imposed on them.

In our experiment, the energies of the outgoing neutrons were determined by time of flight, where it was assumed that the neutrons travel from the geometric center of the deuterated scatterer to the center of the neutron detectors. To be able to directly compare experimental and simulated results, it was necessary to re-calculate the neutron energies of the simulation as if the flight path was from the center of the scatterer to the center of the neutron detector. The new energies are denoted by a prime (E_1', E_2',E_3'). They are calculated from the unprimed energies using

$$E_i' = (\frac{d_i'^2}{d_i^2})E_i, \tag{4.6}$$

where $i = 1$ or 2. The center-to-center distance from target to neutron detector is d_i', and d_i is the actual distance traveled by the simulated neutron. The proton energy does not need to be corrected for this effect, therefore for the proton primed and unprimed energies are the same.

In the simulation the proton energy E_3 was calculated from the two neutron energies E_1 and E_2 using

$$E_3 = E_{tot} - E_1 - E_2, \tag{4.7}$$

where E_{tot} is the total energy available to the three nucleons in the outgoing channel (10.775 MeV for a $E_0 = 13.0$ MeV neutron beam).

Events for the *nd* breakup reaction were generated as follows:

1. Interaction points were randomly selected within the deuterated scatterer and the neutron detectors that registered the *np* FSI event. This choice fixed the angles $\theta_1, \theta_2, \phi_{12}$, while the bombarding neutron energy E_0 was chosen from a distribution between 12.8 and 13.2 MeV. These steps defined the kinematic locus, i.e. the S-curve, in $E_1 - E_2 - E_3$ space.

2. A multi-parameter linear interpolation was used to obtain the cross section values $\bar{\sigma}(E_1, E_2, E_3)$ between grid points in the relevant cross section library (see section 4.2).

The interpolation parameters used were $\theta_1, \theta_2, \phi_{12}$, E_n, and the breakup nucleon energies E_1, E_2, E_3.

3. The values for $\bar{\varepsilon}(E_1, E_2, E_3)$, $\bar{\alpha}(E_1, E_2, E_3)$ and $\omega(E_3)$ were calculated for the event point. The individual neutron detection efficiencies $\varepsilon_1(E_1)$ and $\varepsilon_2(E_2)$ were put into the MC code in data tables.

4. The proton energy was chosen using conservation of energy (Equation 4.7). A normalized Gaussian function $\omega_3(E_3)$ was used to simulate the energy resolution of the center detector. The energy of the proton is shifted to a new value chosen based on the Gaussian distribution. The same procedure is used to simulate the time resolution of the setup. The new energies are denoted with double primes.

5. The weight factor elements

$$k(E_1'', E_2'', E_3'') = \bar{\alpha}(E_1, E_2, E_3)\bar{\varepsilon}(E_1, E_2, E_3), \tag{4.8}$$

and the cross section elements

$$s(E_1'', E_2'', E_3'') = \bar{\sigma}(E_1, E_2, E_3)\omega(E_3)\bar{\alpha}(E_1, E_2, E_3)\bar{\varepsilon}(E_1, E_2, E_3), \tag{4.9}$$

are calculated. The cross section $\bar{\sigma}(E_1, E_2, E_3)$ was obtained from the cross section libraries. These two factors are needed for the calculation of the simulated cross section along the S-curve as will be described below.

The theoretical *nd* breakup differential cross section $\frac{d^3\sigma^{MC}_{anp}}{d\Omega_1 d\Omega_2 dS}(S)$ was obtained for each *np* FSI configuration using the following procedure:

1. The point-geometry locus was calculated for each *np* FSI configuration. A set of points along the curve were chosen using the same procedure used in the analysis of the experimental data (see Section 5.4.3). The events will were projected on these set of points. This locus was calculated in momentum space.

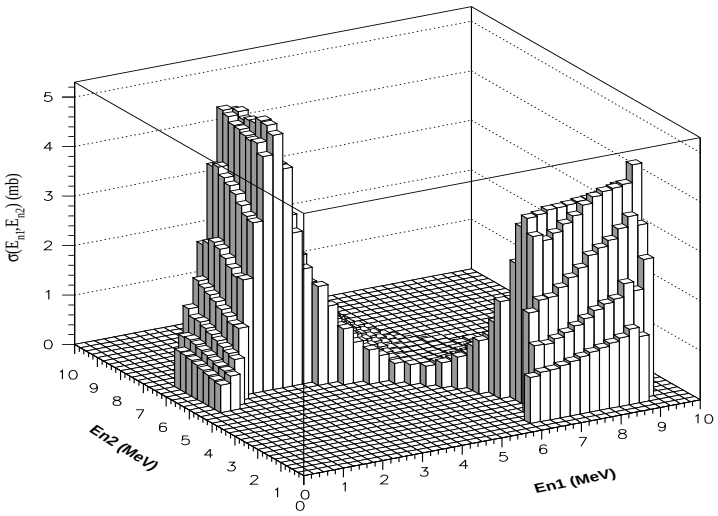

Figure 4.3: $\bar{\sigma}(E_1'', E_2'', E_3'')$ matrix projected onto the E_1' vs. E_2' plane for easier viewing (npfsr1 configuration).

2. The energies of the three particles were converted into momentum space using $k_i = \sqrt{2mE_i}$. Then the simulated events were projected onto the points chosen in the previous step along the kinematic locus. The value of each element $k(k_1'', k_2'', k_3'')$ and $s(k_1'', k_2'', k_3'')$ was assigned to the point which was closer in momentum space to the simulated event. In other words the quantity

$$K_{min} = \sqrt{\sum_{i=1,2,3} (k_i^{ideal} - k_i'')^2} \tag{4.10}$$

was minimized [Fin87]. The superscript *ideal* indicates the momenta along the point-geometry locus. From these projections we obtain the weight factor $\kappa(S)$ and the simulated yields curve $\bar{\Sigma}(S)$

$$\bar{\Sigma}(S) = \frac{\sum_{k_i''} s(k_1'', k_2'', k_3'')}{\sum_{k_i''} \bar{\omega}(k_1'', k_2'', k_3'')} \tag{4.11}$$

and

$$\kappa(S) = \frac{\sum_{k_i''} k(k_1'', k_2'', k_3'')}{\sum_{k_i''} \bar{\omega}(k_1'', k_2'', k_3'')}. \tag{4.12}$$

The summations go over the indices k_i'' that correspond to a point S on the ideal S-curve according to the criterion given by Equation 4.10.

3. Finally, the expression

$$\frac{d^3\sigma_{a_{np}}^{MC}}{d\Omega_1 d\Omega_2 dS}(S) = \frac{\bar{\Sigma}(S)}{\kappa(S)} \tag{4.13}$$

yields the theoretical *nd* breakup differential cross section for discrete values of S along the ideal *np* FSI kinematic locus $S(E_1^{ideal}, E_2^{ideal}, E_3^{ideal})$. The subscript a_{np} indicates the neutron-proton scattering length corresponding to the cross section calculation. Fig. 4.3 shows the cross section projected onto the E_1 vs E_2plane, while Fig. 4.4 shows a point-geometry cross section compared to a finite-geometry one for $a_{np} = -23.7$ fm.

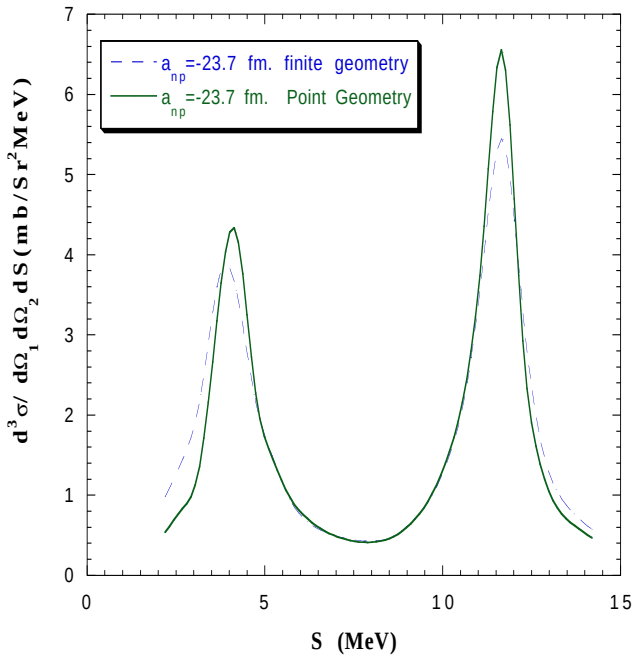

Figure 4.4: Comparison of finite and point-geometry *nd* breakup differential cross sections for the npfsr1 configuration.

Chapter 5

Data analysis

5.1 Introduction

Table 5.1 summarizes the data acquisition schedule of the experiment. There were ten sets of data taken during the experiment. The measurements were made over a 15-month period. Dividing the data acquisition part of the experiment into sets resolved several issues created by the large beam time requirements of the project. By spreading the data accumulation over 15 months, the impact on the tandem accelerator schedule was reduced. The interval between sequential sets was used to evaluate the most recent data and to make adjustments to the experimental setup if needed. In addition, a comparison of cross sections and experimental parameters (e.g. beam luminosity) determined in different data sets, gives a measure of the systematic uncertainties in our techniques.

Each data set consists of several hundred individual runs. The data-accumulation time for each run was about 45 minutes. A number of practical factors were considered in setting the run length. Among them were the overflow of some of our 24-bit hardware scalers, the amount of data lost in the event of a computer crash and the amount of disk space needed to store a run.

From this point, the different data sets will be referred to by their index number as

it appears in Table 5.1.

index	start date	end date	runs
1	6 June 94	16 June 94	108
2	12 August 94	24 August 94	284
3	21 October 94	3 November 94	353
4	22 January 95	5 February 95	365
5	28 February 95	8 March 95	239
6	27 March 95	3 April 95	215
7	10 May 95	19 May 95	327
8	2 July 95	17 July 95	494
9	23 August 95	31 August 95	250
10	14 September 95	22 September 95	269
		Total runs	2904
		Total hours [a]	2178

Table 5.1: The a_{np} experiment data acquisition summary.

[a] Using 45 minutes as the length of the average run

This was the first TUNL experiment performed using the IUCF (Indiana University Cyclotron Facility) version of the XSYS data acquisition package, which is a software engine for CAMAC based data acquisition and data analysis on a VAX-VMS operating system. The IUCF XSYS, which was mainly implemented by Neil R. Yoder of IUCF, is an enhanced version of the TUNL XSYS package. One feature of the IUCF XSYS that is not available in the TUNL version and that was important in the present work was the capability of having variable size events. This feature made it possible to do zero-suppressed readout of the CAMAC digitizers. It was decided to use the IUCF XSYS package because the number of detectors in the present experiment was too large to read in data from all detectors for every event. For *nd* elastic scattering triggers only one side neutron detector is involved and for breakup triggers only two neutron detectors are hit. Reading in the data for all detectors for each event trigger, would be a waste of CPU time and disk storage space. By reading the digitizers in "zero-suppression" mode, only the ADC (analog to digital converter) and TDC

channels with non-zero values are read into the event data stream. The zero-suppressed readout reduced the event size from 42 2-byte words down to an average of 10.

For each event trigger, the pulse height, pulse shape (PSD), and time-of-flight (TOF) of each neutron detector involved in the event and the pulse height of the center detector (CDPH) were stored. The online data analyzer was written in the XSYS Event Analysis Language (EVAL) and had some embedded Fortran subroutines. At the beginning of the event-analysis program a Fortran subroutine identifies the detectors which were hit and stores the detector parameters in variables with descriptive names for convenient access.

During the experiment the online computer processing of the data was kept to a minimum to reduce the dead time. The processing was just enough to produce histograms of the kinematic locus of the two outgoing neutrons for all the configurations of interest. The loci were clearly visible after a day of running. These histograms were a good indication that reasonable data was being accumulated. At the same time all the events were written to magnetic tape for offline processing. In total we accumulated 42 8-mm EXABYTE tapes of data. Each tape on the average contained about 1 Gigabyte of data.

This chapter describes in detail the offline analysis procedure used to extract a_{np}. The offline data analysis of the experiment was implemented in five stages.

1. The beam-target luminosity β, the product of the neutron flux times the number of scatterers in the target, was found by analyzing neutron-deuteron (nd) elastic scattering events. The luminosity is needed for absolute normalization of the nd breakup cross-section data.

2. The light-output function of the center detector (CD) was determined for deuterons from nd elastic scattering data. The function obtained for deuterons was used to derive the light-output function for protons in breakup events.

3. A reduced data set was written to summary tapes. The events that eventually were written to tape were highly constrained by conditions placed on the neutron time-

of-flight, the PSD, the pulse height, and the total energy of the three particles in nd breakup . This reduces the amount of data by several orders of magnitude.

4. Analysis of the summary tapes using Monte-Carlo (MC) simulations of the experiment (see Chapter 4). The probability distributions used in the simulations were derived from the results of exact three-body calculations. The calculations make use of the Bonn-B meson exchange potential. These calculations do not include a three-nucleon force. The event data were weighted according to the probability distributions and projected onto the kinematic locus. The cross sections were determined from the projected data.

5. A χ^2 analysis is performed to determine a value of a_{np} from the cross-section data. The cross-section data were compared to MC simulations made with different values of a_{np}. The value of a_{np} that gives the minimum χ^2 is the value reported in this work.

The first three steps were carried out on the TUNL VAX cluster using the IUCF XSYS software package. The last two steps were done on the TUNL SUN cluster using the PAW++ (Physics Analysis Workstation) data-analysis package from the CERN software library. In preparation of the two final steps, the events were converted to NTUPLE format. The NTUPLE format is a special data base created by the CERN software group specifically for the analysis of particle and nuclear physics data. It permits data to be constrained by conditions on any experimental parameters or functions of these parameters.

5.1.1 Accidentals

The high rate in the CD introduces the possibility of starting the TDC with the pulse of an event uncorrelated with the neutrons detected. These type of events are referred to as accidental coincidences, accidental events, or simply accidentals.

In the electronic setup we require a coincidence between the CD and at least one of the neutron detectors to trigger the start signal to the TDC. It is in this coincidence window

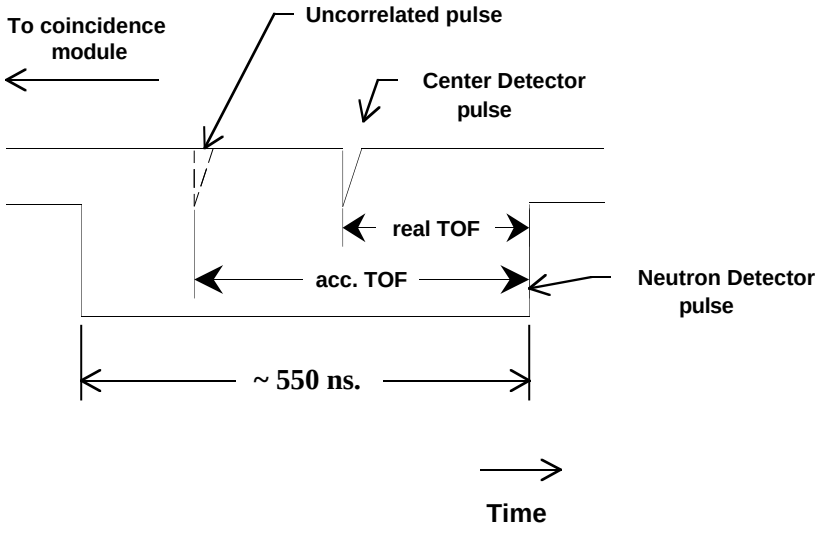

Figure 5.1: Accidental events occur when an uncorrelated signal arrives in the coincidence module and fulfills the coincidence requirement to generate a start signal for the TDC.

where we get accidental events. We can have an accidental if there is an uncorrelated CD pulse that comes to the coincidence module before the pulse associated with the neutron being detected, as illustrated in Fig. 5.1. Since the TOF is the time difference between the trigger signal and the signal from the neutron detector, the earlier the trigger is produced in the coincidence module, the larger the TOF value. In other words, accidental events are real events placed at a later TOF. There is also the possibility of the CD pulse coming later but for these events to trigger the digitizers, the real start pulse must be lost. The loss can occur due to dead time, but it was found that these events accounted for only a small percentage of all lost counts.

If we had events corresponding only to a definite energy, then the TOF spectrum would look like the one shown in Fig. 5.2. This is the distribution from an LED pulser fed into a neutron detector and into the CD. One can see the small number of accidental events due to pulses lost because of dead time (the ones appearing before the main peak in channel

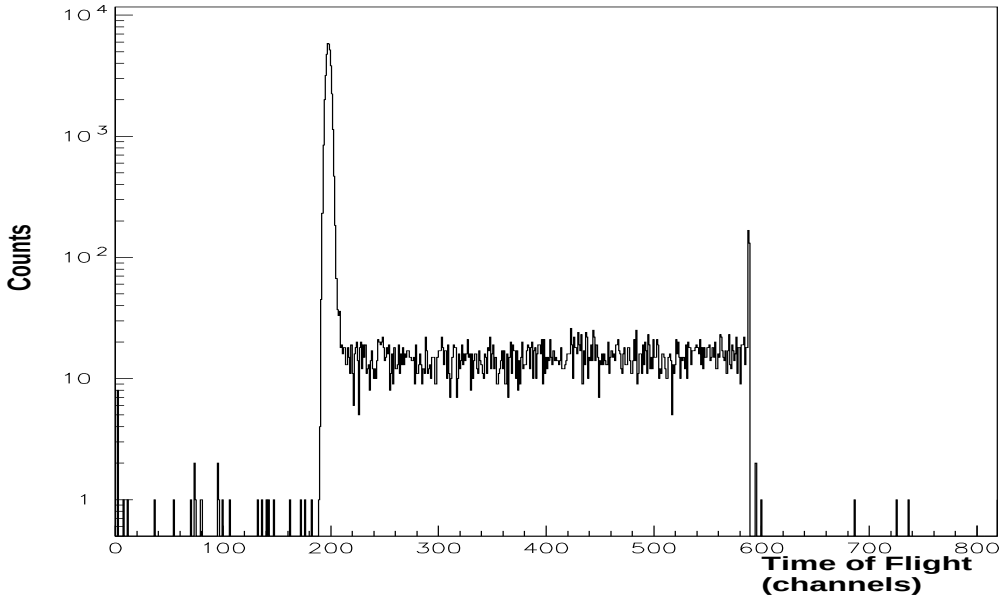

Figure 5.2: Accidental events for a mono-energetic source. The counts at times earlier than the main peak are due to accidental events in which the true signal is lost because of dead time and an uncorrelated pulse arrives some time later. The ones at times after the peak are because of an uncorrelated pulse arriving before the true pulse.

200). The percentage lost in this manner is about 0.06% of the total. The accidentals after the main peak are about 16% of the counts and so constitute by far the main source of accidental losses.

For a distribution of neutron energies the relationship between the measured spectrum $p_m(t)$ and the real spectrum $p(t)$ is given by ([Boe91]):

$$p_m(t) = p_r(t) + e^{-R_{CD}(\tau - t)} p(t) + e^{-R_{CD}(\tau - t)} R_{CD} \int_{t_{min}}^{t} p(t')\, dt'. \tag{5.1}$$

In the above equation R_{CD} is the CD rate ($\sim$ 0.4 MHz), τ is the time width of the coincidence window ($\sim$ 550 ns), and $p_r(t)$ is the flat accidentals distribution due to random background in the neutron detectors. The second term is the number of "true" counts left at time t. The number of counts lost to accidentals will then be $(1 - e^{-R_{CD}(\tau - t)})p(t)$. They are distributed from channel t, all the way down to the end of the coincidence window. In the TOF spectrum they show up as events distributed from the main peak to the end of

the TOF spectrum. The third term is the counts gained in the TOF spectrum at time t from events with TOF less than t due to accidental coincidences.

We solve Equation 5.1 for $p(t)$ by using an iterative procedure. Let $p'(t)$ be the best estimate of the true spectrum in the previous iteration. As a first guess we used $p'(t) = p_m(t) - p_r(t)$. Discretizing Equation 5.1 by changing the integral to a sum over finite time intervals we get

$$p(t) \approx e^{R_{CD}(\tau - t)}(p_m(t) - p_r(t)) + \sum_{t'=t_{min}}^{t} p'(t) R_{CD} \Delta t'. \tag{5.2}$$

The time interval chosen is the time per channel $\Delta t'$ (~ 0.2 ns). After each iteration one can test for convergence by comparison of $p(t)$ and $p'(t)$. The difference must be statistically consistent with zero.

5.1.2 Pulse-Shape Discrimination (PSD)

The liquid scintillators used in our work are also sensitive to gamma rays. The gamma ray will have the shortest TOF of all events, and show up as a sharp spike in the TOF spectrum before any of the neutron events. Unfortunately because of accidentals (see 5.1.1), a fraction of the gamma events are spread to all time channels after the gamma peak.

To get rid of this contamination in the spectra we chose a scintillator fluid that gives a different pulse shape for a gamma ray as compared to neutrons. The light response of the detector is made of slow and fast components due to the properties of the scintillator liquid. The proportion of these components in the total signal depends on dE/dx, the energy loss per unit length of fluid traversed by the particle that struck the detector. For NE-213 and BC-501 (the liquids in our detectors), there is a large proportion of the slow component for particles with large dE/dx. Therefore, the shape of the light pulses produced by neutron interactions extend for much longer times than those for gammas.

The detector anode signal is split between the constant-fraction discriminator (CFD), and the PSD module in the neutron detector electronics. The PSD module integrates the

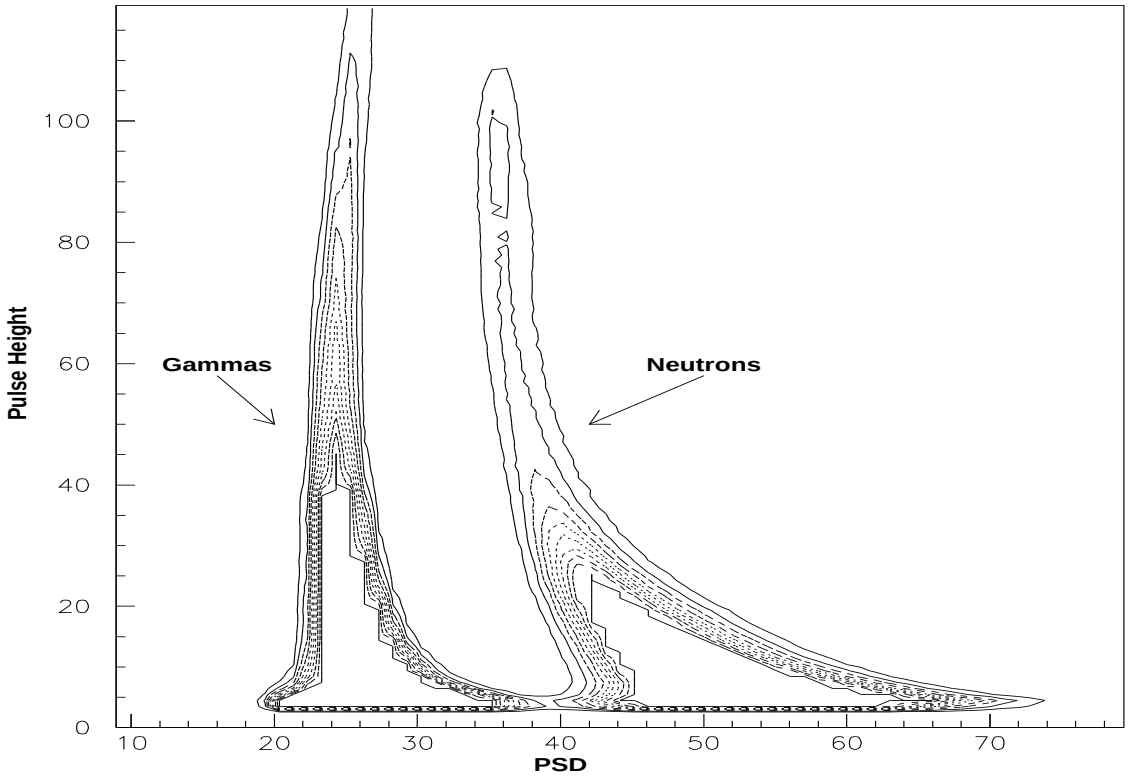

Figure 5.3: Two dimensional histogram of PSD time versus pulse height for one of the neutron detectors used in the *np* FSI cross-section measurements. The neutron mound is on the right, at larger PSD times.

charge in the anode signal. When the charge deposited reaches a certain value, the PSD module outputs a narrow signal. As stated above the signal from neutron interactions extend further in time than those from gamma interactions, therefore they take a longer time to deposit the charge needed to produce an output from the PSD module.

The output from the PSD module is sent to the TDC as a stop signal. The start signal is derived from the CD anode signal. To obtain the distributions of times taken by the signal in the PSD module, the TOF is subtracted from the CD-PSD time spectrum. The PSD values range from a few nanoseconds up to around 100 ns.

To better separate gammas from neutrons we make a two-dimensional histogram

of the PSD time versus the pulse height of the particle detected. Fig. 5.3 shows a sample histogram from one of our detectors. The PSD time bins were compressed by a factor of 8. The TDC was operated at 0.2 ns per channel, so this means 1.6 ns per channel. This time resolution is sufficient for clear separation between neutrons and gammas down to the hardware thresholds, about $\frac{1}{3}\times$Cs .

To eliminate gamma events, a two-dimensional (2D) gate was placed around the neutrons in the PSD vs PH histogram. The resulting TOF spectra show no sign of a gamma peak as can be seen in Fig. 5.4 where no peak is seen before the elastic scattering peak.

5.1.3 Dead Time Correction

The electronic pulsers described in Section 3.4.3 were used to correct for the losses due to the dead time of the system. The scalars reported the total number of pulses of each kind of pulser (LED or electronic) in the system, and the frequency was checked so that it agreed with the one reported by the pulser modules. The LED pulsers measure the dead time of the whole system. Only a few of our detectors were built to allow insertion of an LED signal. The dead time in the detectors themselves was expected to be very small compared to the dead time in the rest of the system, specially the computer dead time. Therefore, the LEDs were only used to check the accuracy of this expectation. Comparing the dead time obtained from both types of pulsers, it was found that the difference between the two was always smaller that 0.5%.

The pulser events were analyzed apart from the physics events. The synchronization signal from the pulser was used to tag the pulser-generated events in the TDC. For each event the pulse height in the side detectors, the PSD time, and the TOF values were stored. Histograms were incremented using the digitized parameters for pulser events. An additional TOF spectrum was conditionally incremented with the requirement that the pulse height signal be above the $\frac{1}{3}\times$Cs threshold cut. The dead-time correction for a particular detector

was calculated as the ratio of the pulser counts in the scalar to the number of counts in the pulser peak in the ungated TOF spectrum, i.e. the one with no $\frac{1}{3}\times$Cs pulse height requirement.

The ADCs used to record the pulse height of the dynode signal of the neutron detector sometimes loose counts. This is a well documented effect and is dependent upon the gate and signal alignment. These counts appear as zeroes in the pulse-height spectra. The correction factor for this electronic effect, referred to as the ADC-correction, is the ratio of the pulser counts in the ungated TOF spectrum to the counts in the gated one. This correction factor was $< 0.1\%$ for the detector pulse heights digitized by the Silena ADC. The detector pulse heights processed in the EG&G ADC, on the other hand, have a correction factor of around 4%.

For the analysis of *nd* elastic data, since we are looking at events from individual detectors separately, the correction factor is simply the product of the dead time and the ADC-correction.

The correction for breakup events is more complicated. For breakup events, the dead-time loss comes mostly at the interface. Therefore, the signals of both detectors in the breakup event are rejected at the same time. The dead-time correction for a particular configuration is then the maximum of the dead times of the two individual detectors involved in the event. Since the ADC on the other hand, independently looses events for each of the two detectors, the net ADC-correction factor is the product of the ADC corrections for both detectors.

5.2 Neutron-Deuteron Elastic Scattering Analysis

When calculating an absolute cross section one must know the beam-target luminosity, the product of the neutron flux and the target density, a quantity we call β. A simple way to obtain the beam target luminosity in our experiment was to analyze *nd* elastic scattering. The cross section of *nd* elastic scattering is well known, so comparison of

the yields obtained to the yields expected (taking into account our finite geometry, beam energy spread and the efficiency of our detectors) will be a measurement of β.

The *nd* elastic scattering data was accumulated concurrently with the breakup data by the neutron beam bombardment of the deuterated scintillator target. The deuterons were detected in the target scintillator and the neutron in one of the 20 scintillators in our setup. All the events must pass a $\frac{1}{3}\times$Cs pulse height threshold cut, and the PSD requirement was used to eliminate events in which a gamma ray was detected in the side detector as described in Section 5.1.2. The resulting TOF spectrum is shown in Fig. 5.4. The elastic scattering neutron peak is clearly visible. The second neutron mound comes from the secondary neutron beam produced by the ^{2}H(d,n)ppn and ^{2}H(d,n)dp source reactions. At forward angles the deuteron energy is below the center detector pulse height (CDPH) threshold, and only through pile-up are some of them detected. At these angles, the peak in the TOF spectrum is strongly suppressed due to the subthreshold losses. These detectors were not used in the calculation of β.

Some of the elastic events may occur at the same time as a background event in another detector. These events will be treated by the electronics as a triple-coincidence event as explained in Chapter 3. They constituted about 1–2% of the total elastic yields and were summed with the double-coincidence data to determine β.

To include the false triples in the total elastic counts, two effects must be taken into account. First, the TOF was corrected for the slight time shift between the double and triple-coincidence branches in the trigger electronics (see Section 3.4.3). The amount and direction of the shift in the detector TOF depends on the electronics of the other detector in the coincidence. Therefore, all possible combinations must be taken into account. The second effect was due to the divide-down circuit used to reduce the number of double-coincidence events. The trigger signal for triple-coincidence events did not go through such circuit. Therefore, the triple-coincidence events were scaled down in software to properly combine them with the double-coincidence events.

To determine the time shift for each detector combination, a TOF spectrum is accumulated for each neutron detector when it was in coincidence with any of the two detectors in one of the other nine pairs. The two detectors in a pair can be accumulated in the same spectrum because they follow the same branch in the trigger circuit. Therefore, the time shift should be the same for both detectors. This results in nine triple-coincidence spectra for each of the 20 detectors. The time shift for a neutron detector TOF when in coincidence with a specific pair of detectors was obtained by taking the difference between the channels of the centroid of the elastic scattering peak in the double-coincidence TOF spectrum and in the triple-coincidence spectrum for that pair. The average of the time shifts of the two detectors in a pair is the time shift used. A 10 by 10 table of time shifts for false triple-coincidence events was created. The entry at row i and column j in the table contains the channels to add to the TOF of a detector in pair i when in coincidence with one of the detectors in pair j to align it with the double-coincidence TOF spectrum.

To correct for the scale-down factor of double events, the effective divide-down factor N is calculated for each run batch being analyzed. This number is the ratio of the number of events before the divide-down circuit to the number of events after the divide-down. A scaler was used to count both numbers. The correction factor was computed by averaging the elastic-scattering count-down factor for all analyzed runs in the batch using the BCI for each run as a weighting factor. For every triple event received the software only completes processing of every Nth event, effectively applying the divide-down factor to the triples.

There are three physical processes that must also be taken into account to obtain the elastic yields.

1. A recoiling deuteron, especially one with a high energy or one located close to the edge of the scatterer, may not deposit all its energy in the CD.

2. There is the possibility that a neutron will scatter from more than one nucleus in the target. These multiple scattering (MS) events can occur from both deuterium and carbon.

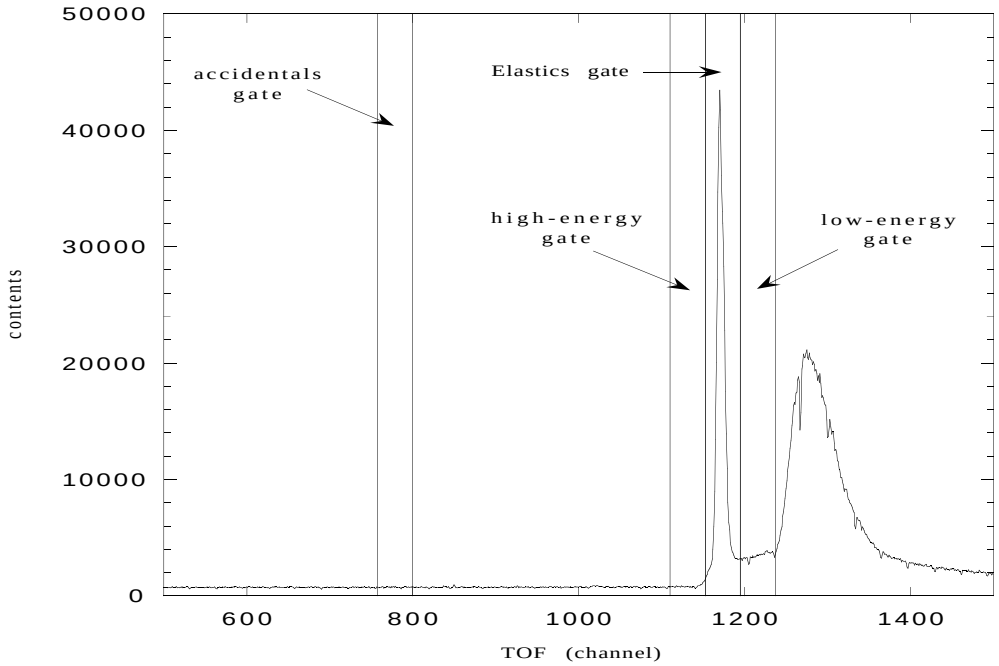

Figure 5.4: Gate around the elastic peak in the TOF spectrum. The accidental gate is placed in the region before the gamma peak where only accidental events can occur.

3. Neutrons produced in the ^{2}H(d,n)ppn and ^{2}H(d,n)dp reactions in the gas cell can have the same TOF as an elastically scattered neutron if they multiple scatter from carbon and deuterium. This background is called the sample-correlated background.

These three effects were separated from the *nd* elastic scattering events by a combination of Monte-Carlo (MC) simulations and data from experimental CDPH events from TOF gates adjacent to the elastic peak (see Fig. 5.4).

The *nd* elastic scattering yields were determined from the CDPH spectrum. Four conditional CD pulse-height histograms were incremented. The first histogram, shown in Fig. 5.5, was conditionally incremented with the requirement that the TOF value of the event had to fall within a gate set around the elastic peak in the TOF spectrum. The second CD pulse-height spectrum was incremented when the value of the TOF fell within a gate set in the flat region beyond the gamma-ray peak. This region of the TOF spectrum solely contains events in which the signals in the CD and the neutron detector are uncorrelated.

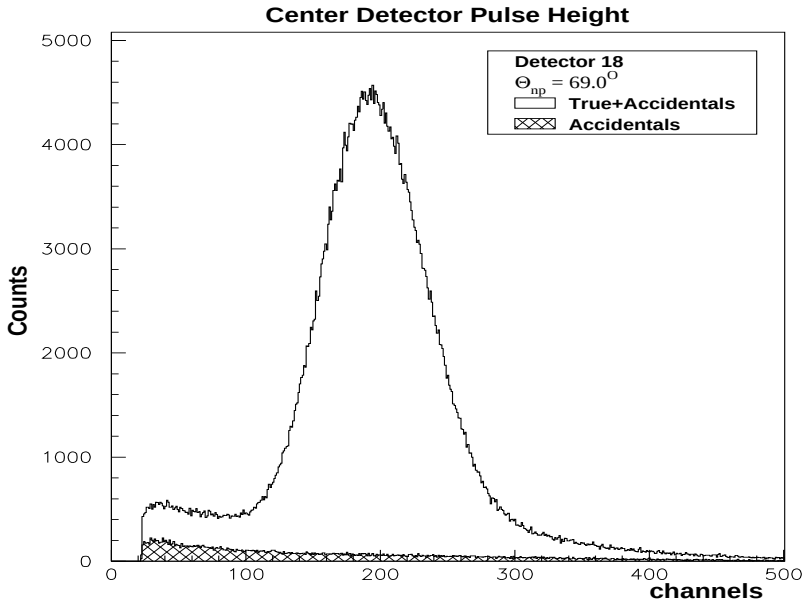

Figure 5.5: Center detector pulse height for deuterons associated with elastically scattered neutrons. The shaded area is due to accidental events.

These are accidental events. The CD pulse height due to accidental events are shown as the shaded portion of Fig. 5.5. The other two histograms are filled with events from the gates adjacent to the main elastic peak. One on the high-energy side and one on the low-energy side. These four gates are shown in Fig. 5.4.

The procedure used to obtain the yields for elastic scattering was as follows:

1. The experimental *nd* elastic TOF peak was Monte-Carlo simulated assuming only single-scattering. The input parameters of the simulation were adjusted to reproduce the centroid position and FWHM of the experimental elastic peak.

2. The MC was used to produce a CDPH histogram of events falling inside a gate on the simulated TOF spectrum equal to the gate around the elastic peak of the experimental TOF spectrum. The MC parameters were adjusted to match the experimental CDPH spectrum after subtraction of the experimental accidental histogram. For this an exponential background was added to the MC spectrum to simulate MS events and

sample-correlated background events.

3. MS contributions were simulated for events falling in the low-energy, elastic, and high-energy TOF gates. These MS histograms were normalized and subtracted from their corresponding experimental CDPH spectra.

4. The low-energy and high-energy CDPH spectra, after subtraction of accidental and MS events, were averaged channel-by-channel and normalized to fit the tail end and the beginning of the elastic CDPH spectrum. An exponential fit was made to the suggested background and then the fit was subtracted from the experimental spectrum. A sample CDPH histogram with the sample correlated background obtained by this procedure is shown in Fig. 5.6.

5. The resulting spectrum was integrated to obtain the net elastic yields.

The following equation was used to determine β, the beam-target luminosity, from the yields for elastic scattering:

$$\beta = \frac{Yields(\theta) \cdot ScaleFactor \cdot DTC}{\frac{d\sigma_{el}}{d\Omega}(\theta) \cdot d\Omega \cdot \epsilon(E_n) \cdot BCI \cdot \alpha(E_n)}. \tag{5.3}$$

In this equation, θ is the angle of the neutron detector. The scale factor is the divide-down factor electronically applied to the double events. The DTC is the dead-time correction multiplied by the ADC loss for double events (see Section 5.1.3). The α in the denominator is the attenuation of neutrons in the target and in air. It was obtained from a Monte-Carlo simulation using well-known neutron cross sections. The neutron detector efficiency $\epsilon(E_n)$ was measured as described in Chapter 6. The solid angle $d\Omega$, is the neutron detector area divided by the square of the flight path. The BCI is proportional to the charge deposited by the deuteron beam on the neutron production target, i.e. the deuterium gas cell. To get this number the signal from the beam stop was fed to a charge integrator and then counted by a scalar. Finally, $d\sigma_{el}/d\Omega(\theta)$ is the nd elastic scattering cross section at the angle of the neutron detector.

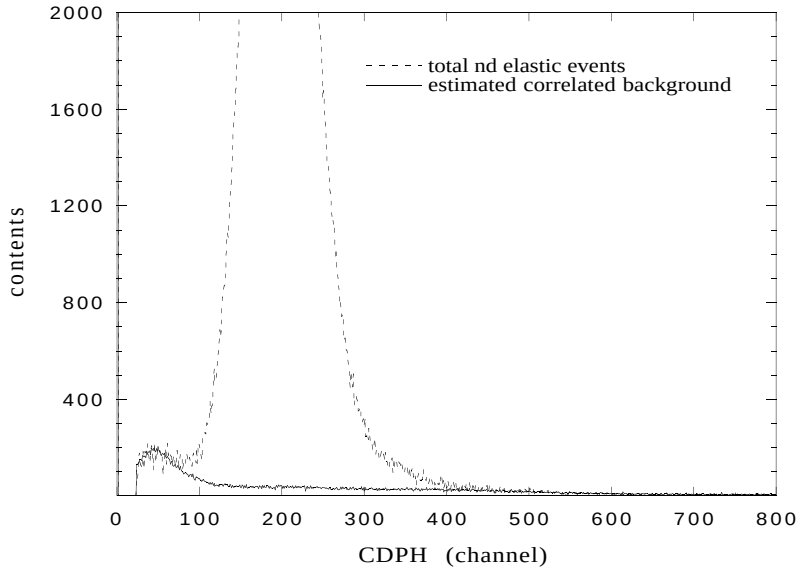

Figure 5.6: Experimental elastic CDPH histogram after subtraction of accidental and MS background. The solid curve is the sample-correlated background estimated from the TOF gates adjacent to the elastic peak corrected for accidental, multiple scattering, and normalized to match the experimental background.

In this manner β was measured using at least three neutron detectors for each run. The value obtained for all detectors should be the same, therefore the deviation in the values was a measure of the systematic uncertainty in our technique for determining the elastic yields. The results are shown in Table 5.2.

run	β_r	standard deviation of the mean	% standard deviation of the mean
4	1538.	14.	0.9
5	1524.	26.	1.7
6	1894.	21.	1.1
7	1764.	8.	0.5
8	1696.	40.	2.3
9	1577.	41	2.6
10	1632.	35.	2.1

Table 5.2: Beam-target luminosity, β, for all runs.

5.3 Center Detector Light-Output Function

The light-output function for protons in the CD was needed to convert pulse height to particle energy. Our setup did not permit the direct determination of this function for protons, so we measured the deuteron light curve and derived the one for protons from it. The light-output function for deuterons in the CD was obtained from the elastic scattering data. This function was used to calculate the energy of the protons in the breakup events. The relationship between the light-output function for protons and deuterons in our deuterated scintillator (NE-232) is

$$L_p(E) = \frac{1}{2} L_d(2E). \tag{5.4}$$

A CDPH histogram was accumulated for nd elastic scattering to each angle in our neutron detector array. The centroid of the peak for elastic scattering to all angles greater than 20° was recorded. At 20° or less some nd elastic events were lost because the finite

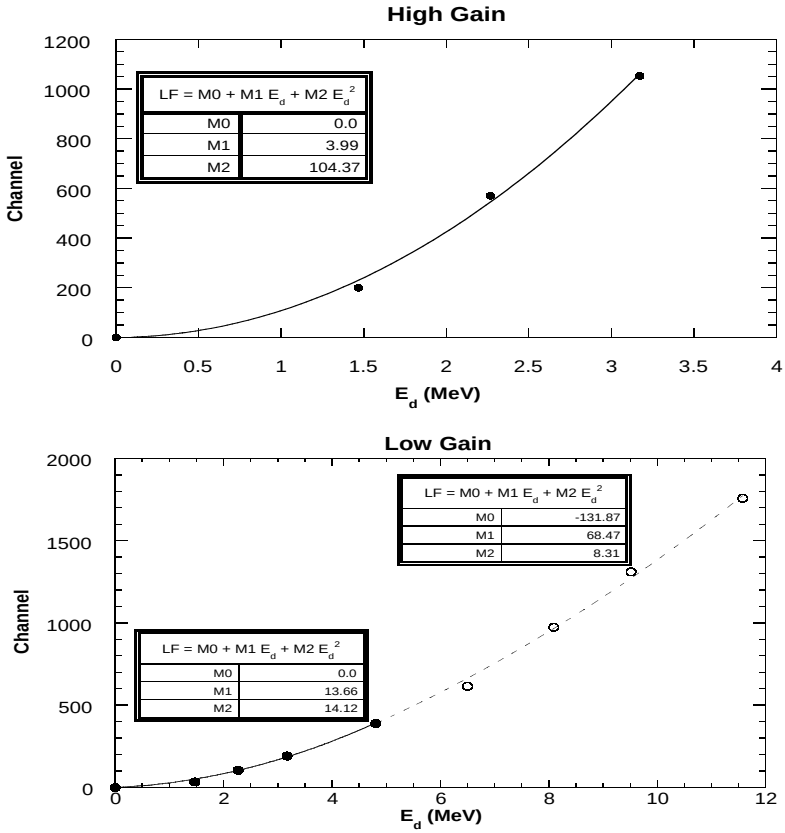

Figure 5.7: Center detector pulse height as a function of the deuteron energy for the high- and low-gain center detector dynodes. Quadratic functions were used to fit the data. For the low-gain LOF, two fits were used. Both fits coincide in value and in slope at 4.81 MeV.

resolution of the CD put a fraction of the pulse heights below the hardware threshold. The clipping of the pulse-height distribution by the hardware threshold distorted the shape of the distribution and made the forward-angle data unusable in the extraction of the light-output function.

The light-output functions for the low- and high-gain dynodes is shown in Fig. 5.7. To obtain a continuous function for the low-gain pulse height, the data was fit using one or two quadratic functions. Two functions were necessary to fit the whole range of energies for some runs. In those runs, the high-voltage setting in the CD phototube was high enough to cause saturation. When saturation occurs the slope of the light-output curve decreases

with increasing deuteron energy. For the runs where no saturation was observed, only one quadratic function was necessary.

5.4 Breakup Analysis

5.4.1 Summary Tapes

The first stage in the breakup-data analysis is the reduction of the event set into summary tapes. Every event was required to fulfill several requirements. This reduced the size of the event files by a factor of 10,000, allowing for faster analysis of the data. Only triple events corresponding to the 8 configurations of interest were written to the summary tapes.

For each event, the pulse-height and pulse-shape parameters of both neutron detectors had to fulfill the $\frac{1}{3}\times$Cs and the PSD requirements explained in the previous sections. A lower threshold of 0.6 MeV was put on the CDPH. This was the lowest energy at which we had confidence that all events of that energy were being counted. The 0.6 MeV threshold was lower than required by any of the configurations of interest.

The energy of both neutrons was calculated from their TOFs. The proton energy was determined using the light-output function of the CD. A histogram of the sum of the energies of the three detected particles (two neutrons and the proton) was accumulated. Energy conservation requires the sum of these three energies to be 10.775 MeV, the energy remaining from the 13.0 MeV initial energy after breaking the deuteron. Accounting for experimental energy spreads, all events were required to have their total energy within $\pm$4.0 MeV of this value. Fig. 5.8 shows a plot of the total energy spectrum for the four *np* FSI configurations with ring detectors. The centroid of the main peak in all cases was at 10.8 MeV.

Only events that met all of the requirements detailed in the previous two paragraphs were written to magnetic tape. Each event that passed the requirements was stored in

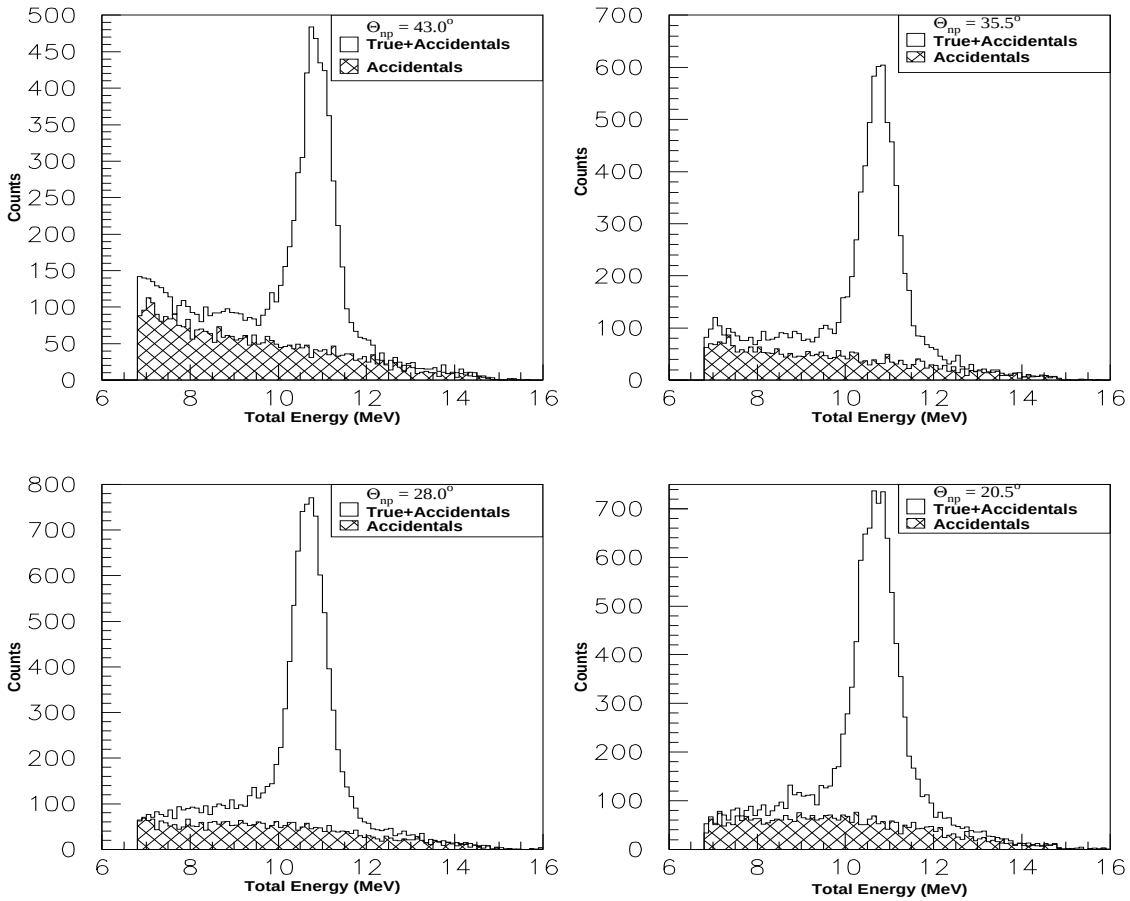

Figure 5.8: Total-energy spectra for the four configurations with ring detectors. The shaded area comes from accidental events. The centroid of the peak is at 10.78 MeV.

magnetic tape. The parameters stored were: the configuration to which it belonged, the event type with regards to accidentals (the four types enumerated in Section 5.4.2 under random background), the TOF of both neutrons, and the low- and high-gain CDPHs. For preparation of the final stage of the analysis, the event files were converted to PAW ntuples.

5.4.2 Accidentals in *nd* breakup Analysis

During the recording of events to the summary data tapes, accidental events were tagged so they could be subtracted from the total yields. In *nd* breakup we look for coincidences between two neutron detectors and the CD. This makes the situation more complicated for the subtraction of accidental events than what was described in Section 5.1.1 for double-coincidences.

There are two main kinds of accidental events. The first kind are accidentals due to time uncorrelated events that are misidentified as breakup events. In these events one or both neutron detectors fire because of room background neutrons. Since these neutrons are randomly distributed in time, some of these events fall within the kinematic region of valid breakup events. The second kind of accidentals are those where the event is a valid breakup event but the start signal to the triple-coincidence trigger comes from an uncorrelated event prior to the true event. This is the extension to triple-coincidences of the false-start accidentals discussed in the double-coincidence case. The following sections detail the procedure to identify these events.

Random Background

The main contribution to accidentals comes from events where one or both of the neutron detectors fire because of the constant bombardment of room background neutrons. To measure the accidental background we left some room in the TOF spectra in the region before where gamma events appear. Events with TOF values earlier than that of the time-correlated gamma rays must be unphysical and caused by accidental coincidences. In the

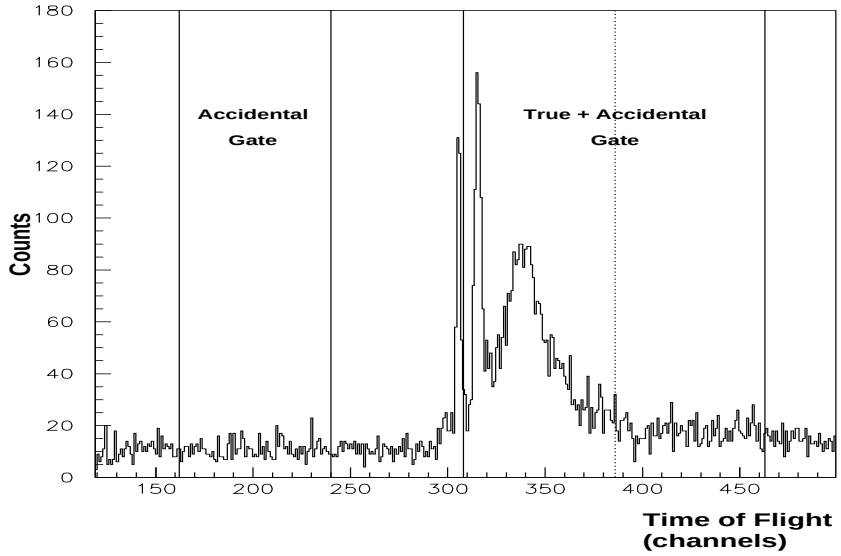

Figure 5.9: Accidental and True + accidental gates in the TOF spectrum for detector 9 at 43°, when in coincidence with detector 17 at 55.7°.

data replay the events with TOF values earlier than the prompt gamma rays were used to determine the accidental events in all parts of the TOF spectra.

To determine the random accidental background, two gates were put in the triple-coincidence TOF spectra for both of the detectors involved in the configuration of interest. The first gate extended from ten channels after the elastic peak all the way up to the channel for the $\frac{1}{3}\times$Cs neutron energy threshold. This gate surrounds the region where true and accidental events are both present and is shown in Fig. 5.9. The second gate was set around the events that come before the gamma peak, and it was half as wide as the first one. It was chosen only half as wide because of the constraint of the 560 ns wide coincidence window.

The events were classified into four categories according to which of the above TOF regions the TOF value in each of the detectors involved in the configuration fell. The following types are identified:

1. The TOF of both detectors falls inside the "true + accidental" gate.

2. Detector 2 TOF is inside the accidental gate, and detector 1 TOF is inside the "true + accidental" gate.

3. Detector 1 TOF is inside the accidental gate, and detector 2 TOF is inside the "true + accidental" gate.

4. The TOF of both detectors falls inside the accidental gate.

Events of type 2–4 were kept separate and were subtracted from the events of type 1 after projection onto the locus in the final stage of the analysis. However, events of type 4 also form an accidental background underneath events of types 2 and 3. Therefore, the projected yields due to events of type 4 were subtracted from the projected yields due to events of types 2 and 3 prior to the subtraction of the total accidental background.

False-Start Accidentals

In every *nd* breakup event, the two neutron signals come at a defined time difference. The CD signal however can come from an uncorrelated event and trigger the coincidence requirement to generate a start signal to the TDC. These false-starts increase the time difference between the start and the two stop signals coming from the neutron detectors by a random amount. However, both TOFs are shifted by the same amount. In a two-dimensional plot of TOF 1 vs. TOF 2, these events appear along a 45° diagonal starting at the true time coordinates of the event. Therefore, we have exactly the same situation as in the one dimensional TOF case but along a 45° line in the TOF1 vs TOF2 plane. This situation is illustrated in Fig. 5.10 (left plot).

To correct for losses we have to use the same exponential correction factor $e^{R_{CD}(\tau-t)}$ derived for the one dimensional case. However, this correction factor enters in the normalization factor β also, since it should affect the elastic scattering events the same way. The only difference will be the time t of the breakup event compared to the time of elastic events. The effect on the cross section is of the order of 1–2% depending on the position of

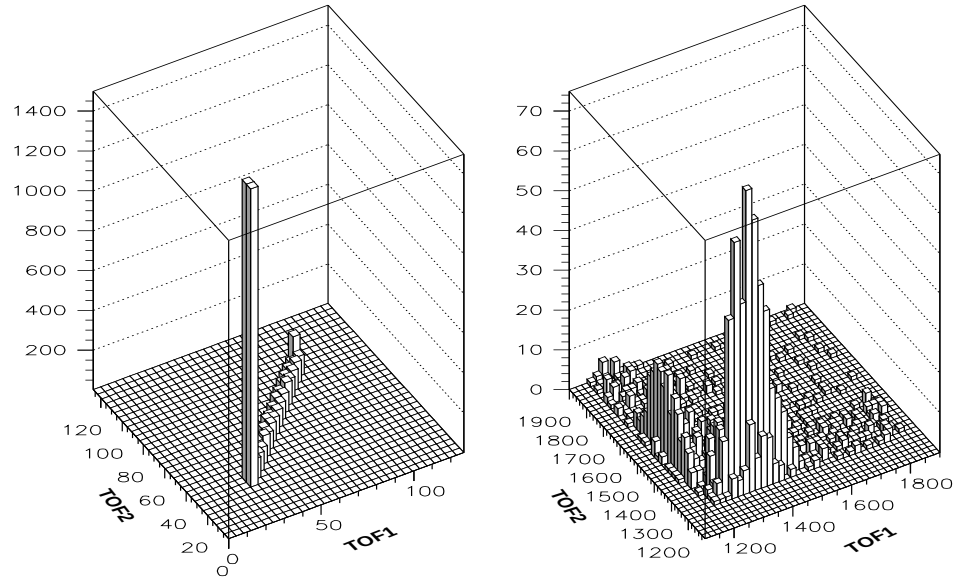

Figure 5.10: The left plot shows the TOF of a synchronized LED pulser into detectors 12 and 20. The main peak is the location of the true TOF, the tail is due to false-start accidentals. The plot on the right shows an experimental 2D TOF spectrum. The *np* FSI locus is clearly visible. This plot contains random accidentals and false-start accidentals. Notice that there are few events before the locus (time increases with channel number). Therefore, the contribution of false-start accidentals is negligible.

the event in the TOF 1 vs. TOF 2 plane.

The correction for gains is more complicated but the effect is very small for two reasons:

1. The counts lost from each real event (13–15%) are spread over many channels($\sim$ 1500), so the contribution to each channel is very small.

2. There is no structure before the *np* FSI locus in the TOF 1 vs TOF 2 plane, therefore few events contribute counts to the locus.

This was tested using an experimental spectrum with only triple events (all accidentals due to random background subtracted), and spreading the counts lost from every channel to the rest of the TOF 1 vs TOF 2 plane along a 45° line. The correction was never above 0.01%.

5.4.3 Extraction of the Cross Section and of a_{np}

In the final stage of the analysis, using the ntuples generated from the summary tapes as described in Section 5.4.1, the TOFs of the two neutrons were converted into energy, and the center detector pulse height was used to find the proton energy.

To obtain cross sections along the ideal kinematic locus, the events in the three-dimensional (3D) energy space were projected onto the ideal locus. The kinematic locus is parameterized in terms of S, the path length along the ideal kinematic curve. The origin of S, i.e. the S=0 point, is chosen where $E_2 = 0$. The direction of increasing S is counter-clockwise.

For projection of the counts onto the locus, a set of points along the S-curve were chosen. The point on the kinematic locus where the theoretical cross section reaches its maximum value was chosen first. Starting from this point the other points were selected by going along the S-curve in both directions in steps of 0.5 MeV. Fig. 5.11 shows the points chosen for the configuration with $\theta_1 = 43.0°$,$\theta_2 = 55.7°$, and $\phi_{12} = 180°$, projected onto the

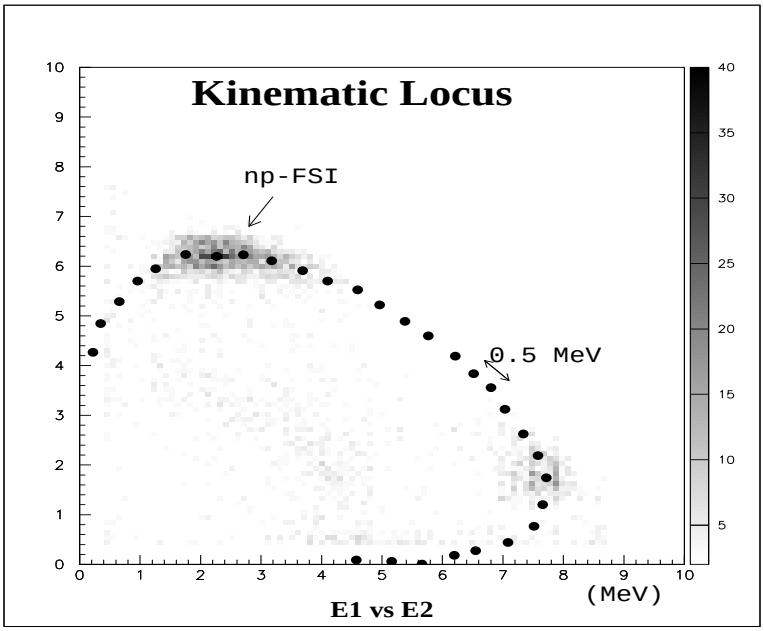

Figure 5.11: Events on the E_1 vs. E_2 plane around the point geometry kinematic locus, for the for the *np* FSI configuration with $\theta_1 = 43.0°$, $\theta_2 = 55.7°$, and $\phi_{12} = 180°$. The black circles are the centers of the bins along the S-curve where the events are projected.

E_1 vs. E_2 plane. Next, the counts were projected from the three-dimensional energy space into the selected set of S-curve bins by finding the closest bin. In other words we minimized:

$$K = (E_1 - E_1^{ideal})^2 + (E_2 - E_2^{ideal})^2 + (E_3 - E_3^{ideal})^2, \tag{5.5}$$

where (E_1, E_2, E_3) are the coordinates of the event in the 3D energy space, and the *ideal* energies are the coordinates of the center of one of the S-curve bins used in the projection. Thus we obtain the yields along the S-curve.

The same procedure was followed to obtain the accidental yields along the locus. The net yields were obtained by subtracting the "accidental" yields from the "true + accidental" ones. Fig. 5.12 shows a plot of both these yields along the S-curve for the configuration with $\theta_{np} = 43°$ involving the ring detector.

The cross section along the S-curve is given by:

$$\frac{d^3\sigma}{d\Omega_1 d\Omega_2 dS} = \frac{Y(S) \cdot DTC}{d\Omega_1 \cdot d\Omega_2 \cdot dS \cdot \overline{\beta} \cdot \overline{\alpha} \cdot \overline{\epsilon} \cdot BCI}, \tag{5.6}$$

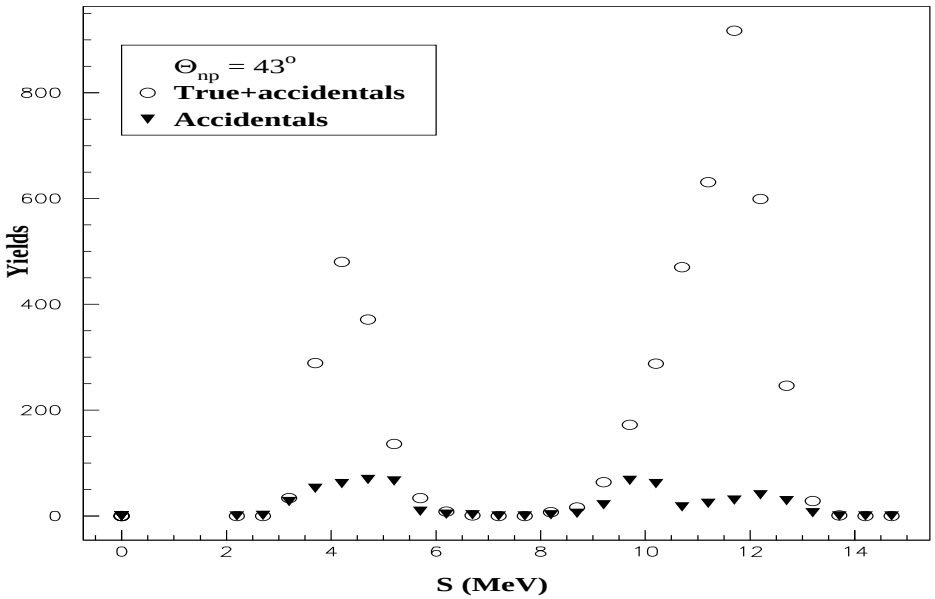

Figure 5.12: "True + accidental" and "accidental" yields along the S-curve.

where $Y(S)$ are the net yields along the S-curve. The calculation of the solid angles, $\overline{\beta}$ (the beam-target luminosity), and the BCI are described in Section 5.2. The dead-time correction DTC was obtained as described in Section 5.1.3.

The effective neutron attenuation ($\overline{\alpha}$) and the neutron detection efficiencies ($\overline{\epsilon}$) are obtained from the Monte-Carlo simulation. The simulation generates three arrays in energy space as explained in chapter 4. These three arrays were used to further restrict the event set, and to calculate the effective attenuation and efficiencies along the S-curve. Only events where the product of the three arrays is non-zero were projected. This in effect puts a 3D cut on the kinematic locus. To calculate the effective attenuation and efficiencies for the cross section equation, two functions along S are calculated:

$$\begin{aligned} F(S) &= \sum_i (\overline{\alpha} \cdot \overline{\epsilon} \cdot w)_i \quad and \\ G(S) &= \sum_i w_i. \end{aligned} \tag{5.7}$$

The index i runs over all the energy bins in the three-dimensional energy space that were

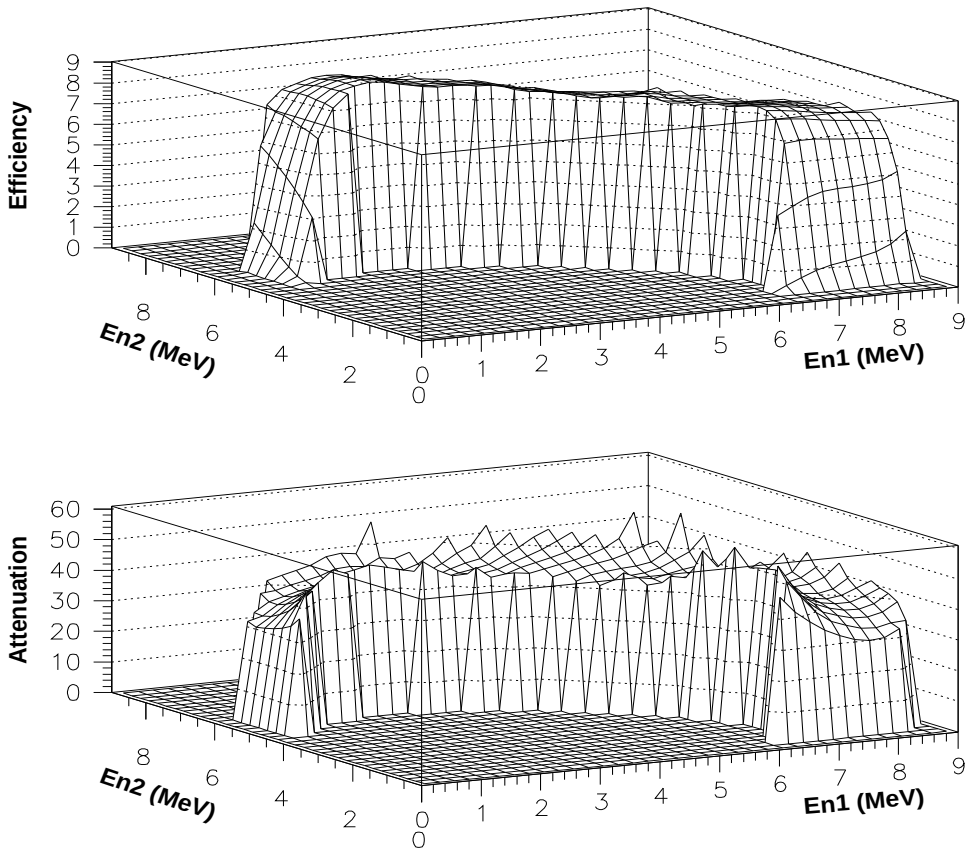

Figure 5.13: Efficiency and attenuation matrices projected on the E_1 vs E_2 plane.

projected onto S. The effective attenuation times efficiency along S is given by:

$$\overline{\alpha} \cdot \overline{\epsilon} = \frac{F(S)}{G(S)} = \frac{\sum_i (\alpha \cdot \epsilon \cdot w)_i}{\sum_i w_i}. \tag{5.8}$$

Fig. 5.13 shows these two matrices projected onto the E_1 vs E_2 plane.

A cross section for each *np* FSI configuration is extracted for each batch of runs, and the statistical average of them is calculated to obtain the final cross section values.

A χ^2 analysis between data and theory was performed to determine a value of a_{np} from each measured *np* FSI configuration. To find a_{np} from the experimental cross section

data, several Monte-Carlo simulations of the experiment were run for different values of a_{np} as described in chapter 4.

The expression

$$\chi^2(a_{np}) = \sum_S \frac{(\frac{d^3\sigma^{MC}_{a_{np}}(S)}{d\Omega_1 d\Omega_2 dS} - \frac{d^3\sigma(S)}{d\Omega_1 d\Omega_2 dS})^2}{(\Delta\frac{d^3\sigma(S)}{d\Omega_1 d\Omega_2 dS})^2} \tag{5.9}$$

gives χ^2 as a function of a_{np}. In this equation $\Delta\frac{d^3\sigma(S)}{d\Omega_1 d\Omega_2 dS}$ is the statistical error associated with the experimental cross section. The total χ^2 of the experimental values with respect to each one of the simulations was computed. A plot of the χ^2 value as a function of a_{np} is shown in Fig. 5.14. A quadratic fit was made to the function. The experimentally extracted a_{np} is the value where the χ^2 fit has its minimum value. The statistical error in the determination of a_{np} is given by

$$\Delta a^{stat}_{np} = \mid a_{np}(\chi^2_{min}) - a_{np}(\chi^2_{min} + 1) \mid \tag{5.10}$$

5.4.4 Breakup Cross Section Uncertainties

The systematic errors in our the experimental *nd* breakup cross sections originate from several sources:

1. The error in the solid angles Ω_1 and Ω_2 is due in part to the uncertainty in the distance of the neutron detectors from the CD ($\pm$0.5 cm). In the case of the ring detectors, there is an additional uncertainty due to the error in the radius. These solid angle errors are assumed to have a normal distribution, i.e. we believe the central value to be the most probable.

2. The systematic uncertainty in the absolute neutron-detection efficiency of each detector is mainly due to the uncertainty in the normalization of the ^{2}H(d,n)^{3}He reaction cross section [Dro78] (see Section 6.2). This normalization uncertainty is $\pm$1.5%. In addition, there are some less important uncertainties in the efficiencies measurements

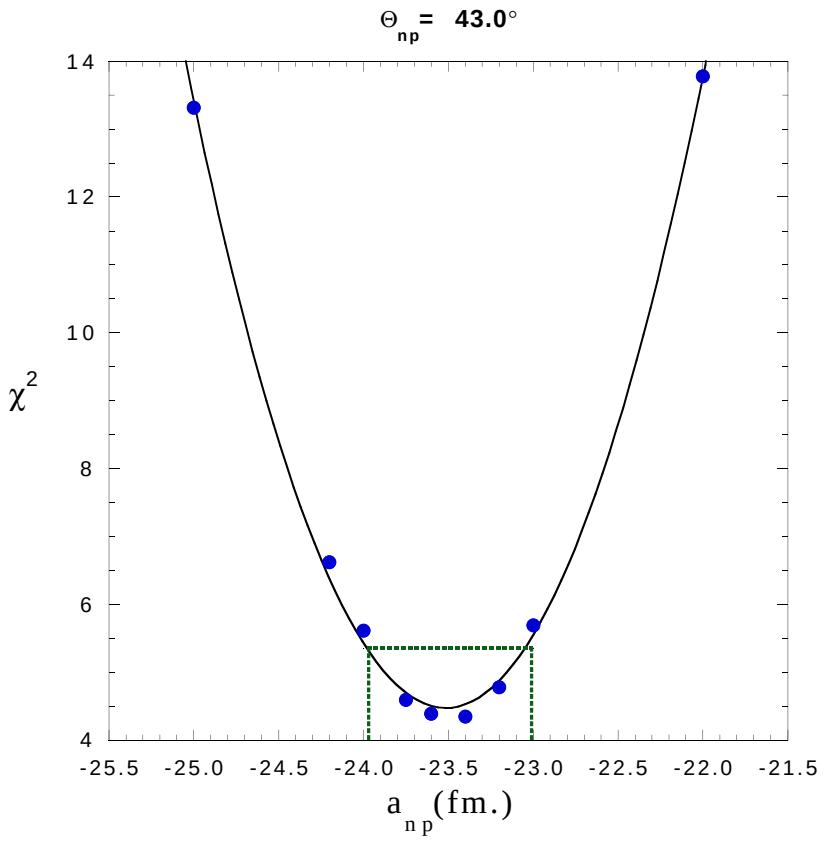

Figure 5.14: Total χ^2 between the experimental and the simulated cross sections as a function of a_{np} for the np FSI configuration with $\theta_1 = 43.0°$, $\theta_2 = 55.7°$, and $\phi_{12} = 180°$. The location of the minimum gives the experimental value of a_{np}. The horizontal dashed line is the point where $\chi^2 = \chi^2_{min} + 1$. The intercepts of this line with the fit give the statistical error in a_{np}.

due to errors in the measurement of the deuterium pressure in the gas cell and due to beam heating effects in the gas cell. These uncertainties amount to about ($\pm 1.0\%$). The sources of error in the absolute detector efficiency are uncorrelated and assumed to have a normal distribution. Therefore, we combine them in quadrature. The total is $\pm 1.8\%$ ($\sqrt{(1.5)^2 + (1.0)^2}$). This uncertainty has the same sign and magnitude for all detectors.

3. There is about a $\pm 1.0\%$ uncertainty in our determination of the shape of the efficiency curve for each neutron detector. This uncertainty was determined by comparing the efficiency measurement taken with the ^{2}H(d,n)^{3}He reaction, to those made using the neutrons from the spontaneous fission of a ^{252}Cf source. As with the other uncertainties, this uncertainty is assumed to be normally distributed.

4. The error in the threshold setting (± 7 keV in electron energy) for the pulse height of the neutron detectors has an effect on the efficiency shape and magnitude. This is a small effect about $\pm 0.5\%$. There is no correlation between detectors in this uncertainty, and it is assumed to have a normal distribution.

5. The attenuation factors α_i (where "i" is the detector number) have an uncertainty of $\pm 1.5\%$ due to the error in the absolute neutron total cross sections of deuterium and carbon. These cross sections were used in the simulations to compute the attenuation of the neutron flux for each detector.

6. The uncertainty in the yields for *nd* elastic scattering is caused mainly by the error in our background subtraction technique. The uncertainty in extracting the elastic yields from the experimental spectra (see Section 5.2) was taken as the standard deviation of the beam-target luminosity β determined at three scattering angles. The net uncertainty is the statistically weighted average of the standard deviation obtained during each run period (see Table 5.2). The net uncertainty in the elastic yields is $\pm 1.62\%$.

7. The systematic error in the elastic scattering cross section in the calculation of the beam-target luminosity β. This error is ($\pm 1.5\%$).

In the computation of the breakup cross section, the beam target luminosity was factored into its constituents so that correlations could be explicitly accounted for in the calculation of the uncertainties. The systematic error in the *nd* breakup cross section follows from Equations 5.6 and 4.2 by adding the uncorrelated errors for all factors in quadrature. However, the correlated errors have to be treated separately. There is a cancellation between correlated errors for factors that appear in the numerator and denominator. For example, the attenuation factors were computed using the same library of cross sections for the calculation of the *nd* breakup cross section and for the calculation of β. The attenuation factor by which the elastic yields are divided to obtain β ends up in the numerator of the equation for the *nd* breakup cross Section 5.6. Therefore, the errors in the attenuation in the β factor cancel in part the error in the attenuation factor of one of the two neutrons in the breakup reaction. These errors are added linearly with a sign indicating whether the factor is in the numerator or in the denominator. The equation for the error due to the attenuation factors is given by

$$(\frac{\Delta\alpha}{\alpha}) = (\frac{\Delta\alpha_\beta}{\alpha_\beta}) - (\frac{\Delta\alpha_1}{\alpha_1}) - (\frac{\Delta\alpha_2}{\alpha_2}). \tag{5.11}$$

A similar equation applies for the error in the absolute detection efficiency.

The total systematic uncertainty is obtained combining the correlated and uncorrelated sources of error in quadrature

$$\begin{aligned}\left(\frac{\Delta\sigma^{sys}}{\sigma}\right)^2 = &\left(\frac{\Delta Y_{el}}{Y_{el}}\right)^2 + \left(\frac{\Delta\sigma_{el}}{\sigma_{el}}\right)^2 + \left(\frac{\Delta d\Omega_1}{d\Omega_1}\right)^2 + \left(\frac{\Delta d\Omega_2}{d\Omega_2}\right)^2 + \\ &\left(\frac{\Delta d\Omega_\beta}{d\Omega_\beta}\right)^2 + \left(\frac{\Delta\alpha}{\alpha}\right)^2 + \left(\frac{\Delta\epsilon^{abs}}{\epsilon^{abs}}\right)^2 + \\ &3\times\left(\frac{\Delta\epsilon^{shape}}{\epsilon^{shape}}\right)^2 3\times\left(\frac{\Delta\epsilon^{thrsh}}{\epsilon^{thrsh}}\right)^2,\end{aligned} \tag{5.12}$$

where Y_{el} is the elastic neutron yields, σ_{el} is the elastic scattering cross section. The Ω_1, Ω_2, and Ω_β are the solid angles of neutron 1, neutron 2 and in the detectors used in

the calculation of β respectively. The α and the ϵ^{abs} are the errors in the attenuation and efficiency after correlations have been taken into account (equation 5.11). The terms involving ϵ^{shape} and ϵ^{thrsh} are the errors in the shape and in the threshold setting in the pulse height of the neutron detectors respectively. The factor of 3 in front of the error terms in these last two quantities correspond to the addition in quadrature of the errors in the two neutron detectors, and in the detectors used in the calculation of the beam-target luminosity.

To find the effect of the error in a_{np} due to the systematic error in the cross section, the values of the cross section along the locus were scaled upwards and downwards by the systematic error and a new χ^2 analysis was made for the new cross sections. The error in a_{np} was given by

$$\Delta a_{np}^{sys} = \frac{1}{2} \mid a_{np}^{max} - a_{np}^{min} \mid . \tag{5.13}$$

The a_{np}^{max} and the a_{np}^{min} are the values obtained with the maximum and minimum cross sections respectively.

The systematic uncertainties in the cross section measurements are summarized in Table 5.3. The final systematic uncertainty was obtained by adding the uncertainties in this table in quadrature (equation 5.12). The total systematic uncertainty in our determination of a_{np} is ± 0.78 fm.

Source	%uncertainty in cross section	uncertainty in a_{np} (fm)
Solid Angle	$\pm$1.03	$\pm$0.21
Efficiency (absolute)	$\pm$1.80	$\pm$0.36
Efficiency (shape)	$\pm$1.73	$\pm$0.35
Det. threshold setting	$\pm$0.87	$\pm$0.17
Attenuation	$\pm$1.50	$\pm$0.30
Elastic Yields	$\pm$1.62	$\pm$0.32
Elastic Cross Section	$\pm$1.50	$\pm$0.30
Total Uncertainty	$\pm$3.87	$\pm$0.78

Table 5.3: Contribution to the systematic error from all sources on the cross section and its effect on the value of a_{np}

Chapter 6

Neutron Detector Efficiencies

6.1 Introduction

The neutron detectors used in the neutron-proton final-state interaction (np FSI) cross-section measurements do not detect all of the neutrons that reach the liquid scintillator cell. It is of paramount importance for an accurate count of np FSI events to measure the proportion of neutrons detected relative to the number of neutrons that hit a detector, i.e. the neutron detection efficiency.

Neutrons are electrically neutral and do not ionize the liquid scintillator directly. Instead, they are detected from the secondary charged particles emitted from nuclear interactions with the scintillator material. For neutron energies below 20 MeV, the neutron may interact with scintillators in the following ways:

1. single and multiple elastic scattering on hydrogen nuclei,
2. single and multiple elastic and inelastic scattering on carbon,
3. breakup of excited carbon into ^{8}Be ($\tau_{\frac{1}{2}} = 0.07$ fs) and α nuclei, and
4. breakup of excited carbon into three α nuclei.

The charged particles emitted transfer their kinetic energy to the liquid scintillator molecules by collision with the atomic electrons. The atoms are excited directly by the ionizing particles or indirectly by the secondary electrons ejected in the ionization process. Upon de-excitation these molecules emit light in the ultraviolet region with an intensity proportional to the energy transfered from the charged particle. The characteristic time periods of light emission are on the order of nanoseconds [Leo94].

The liquid scintillator cell is optically coupled to a photomultiplier (PMT) tube which collects the light and transforms it to an electrical pulse. The PMT amplifies this signal through a cascade of secondary emission electrodes or *dynodes*. The last dynode is called the anode. The voltage of the signal at the anode is proportional to the kinetic energy of the charged particle hit by the neutron. The energy of the charged particles in turn is related to the energy deposited by the neutron in the scintillator fluid.

To measure the neutron detection efficiency of a detector one needs a source that emits a known flux of neutrons. The efficiency is easily calculated by taking the ratio of the neutrons detected to the neutrons incident on the detector, which is computed from the known neutron flux. Two methods were used to measure the efficiency of the detectors used in this experiment. In the first method, the calibrated neutron flux was produced using the ^{2}H(d,n)^{3}He reaction. This reaction was chosen because its cross section has been measured to high precision over the energy relevant to the present work. The ^{2}H(d,n)^{3}He neutron cross sections at different angles and energies were taken from M. Drosg's compilation of values for the ^{2}H(d,n)^{3}He reaction [Dro78]. In our setup for the efficiency measurements, neutron detectors were placed at 0° and 60° relative to the incident deuteron beam axis. The second method used to measure the detector efficiencies employed the neutrons from the spontaneous fission of ^{252}Cf . A ^{252}Cf source emits neutrons isotropically in an energy range from 0 to 10 MeV. The energy distribution of neutrons emitted from ^{252}Cf has been thoroughly investigated and the shape of the spectrum is well known [Cub89].

6.2 The ^{2}H(d,n)^{3}He Measurements at TUNL

6.2.1 Experimental Setup

The ^{2}H(d,n)^{3}He reaction was used to produce neutrons in the time-of-flight (TOF) target area at TUNL. A 50-keV direct extraction negative ion source (DENIS) was used as a source of deuterons. The beam was chopped by deflecting it with a set of plates to which a 2.5 MHz sinusoidal voltage was applied. Beam particles that passed through the deflection plates within the $\pm$20 ns of the zero-crossing of the applied voltage were transported through a rectangular aperture that followed. Particles passing through the plates at all other times were scraped off by the aperture. Subsequently, the beam fragments were bunched into pulses using a double gap buncher. The buncher device consists of a cylindrical conducting tube with a conducting collimator at each end. The collimators were grounded to the beam pipe and there was a gap between each collimator and the center tube. A 5-MHz sinusoidal voltage was applied to the center tube. The buncher compresses the 40 ns beam segments from the chopper into 2 ns wide pulses on target. The time compression is achieved as follows. As the head of the negative beam enters the buncher tube, the polarity of the applied voltage is negative and the head of the beam is slowed down. As the center segment passes the collimator-tube gap, the applied voltage is crossing zero and no force is exerted on the ions. Then the tail of the beam is accelerated by the positive applied voltage. in summary, the buncher slows the head of the beam segment and accelerates the tail so that the segment coalesces into a narrow pulse at the target.

The pulsed beam was accelerated using the FN Van de Graaff Tandem accelerator. The deuteron beam pulses were directed through the 38° beam leg to the neutron Time-of-Flight target area (see Fig. 3.1) and onto a cell filled with deuterium gas at 1.00$\pm$0.005 atm. of pressure. The gas cell was identical in design as the one described in Section 3.2 used in the *nd* breakup experiment.

The neutron detectors were mounted on two steel stands placed at 0° and 60° with

respect to the deuteron beam axis. The cross section of the ^{2}H(d,n)^{3}He reaction at those two angles varies slowly with angle. This feature minimizes the effects caused by errors in the placement of the detectors. Both detectors were placed at the same height as the gas cell. The distance from the center of the gas cell to the center of the liquid scintillator cell was 4.75 m at 0° and 4.15 m at 60°. A diagram of the detector layout is shown in Fig. 6.1.

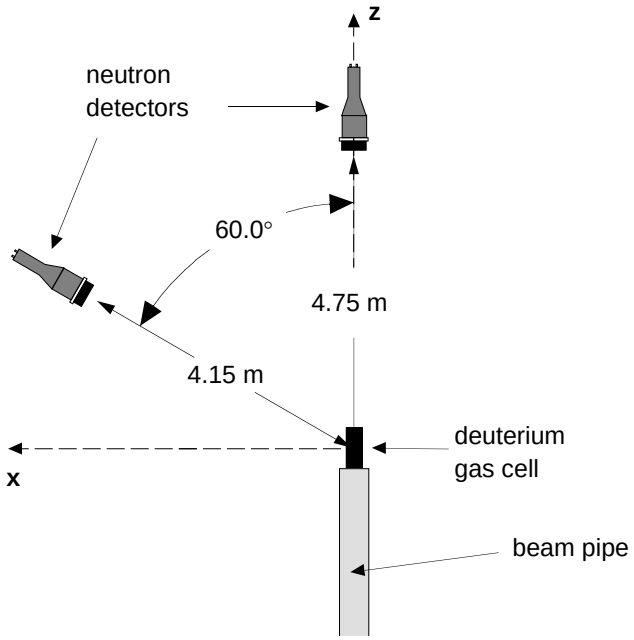

Figure 6.1: Top view of the general layout of neutron detectors for the TUNL efficiency measurements.

The deuteron beam energy was varied from 1.96 MeV to 10.0 MeV by changing the terminal voltage of the tandem accelerator. The deuteron energies used in the measurements and the corresponding neutron energies at 0° and at 60° are shown in Table 6.2.1 (the ^{2}H(d,n)^{3}He reaction has a Q-value of +3.269 MeV.)

With one detector mounted at 0° and the other one at 60°, a first sweep was made

E_{deut}	$E_{neutron}(0°)$	$E_{neutron}(60°)$
1.96	5.20	3.92
3.02	6.29	4.51
3.50	6.77	4.77
4.00	7.26	5.03
4.50	7.75	5.30
5.00	8.24	5.56
5.50	8.73	5.82
6.00	9.21	5.98
6.20	9.40	6.08
7.00	10.17	6.59
8.00	11.13	7.11
9.00	12.08	7.62
10.00	13.03	8.12

Table 6.1: Energy range covered in the ^{2}H(d,n)^{3}He efficiency measurements.

from 1.96 MeV to 10.0 MeV deuteron energy. Then the two detectors were swapped and a second sweep was done from 10.0 MeV down to 1.96 MeV. Thus, the neutron detection efficiency of each detector was measured from a neutron energy of 3.92 to 13.03 MeV.

The neutron energies were measured using the TOF technique. The start signal was generated from the neutron detector anode signal using a constant fraction discriminator (CFD). The stop signal was provided by the pulse generated by the deuteron beam passing through a capacitive pickoff located immediately before the gas cell. These two signals were input to an Ortec 467 time-to-amplitude-converter (TAC). The anode signal of each neutron detector was also processed using a Canberra 2160A PSD module to separate neutron induced signals from those caused by gamma-ray interactions in the scintillators. A TAC was used to convert the PSD information into a voltage. The start signal to the PSD TAC was given by the anode CFD and the stop signal came from the PSD module output. The outputs of the TOF and the PSD TACs were sent to an EG&G AD413A ADC. The single-channel-analyzer (SCA) outputs from both TACs were sent to a coincidence module

to generate a TTL gate for the ADCs. The gate signal went from logical low to high when both TACs were done processing. In addition to the TAC outputs, the dynode signal of each neutron detector after being integrated and amplified, was sent to the ADC. The pulse-height (PH) signal was used to set a lower level threshold, so that the efficiency could be determined for any threshold above the hardware threshold set by the anode CFD.

The PH thresholds were determined using a ^{137}Cs gamma source. The convention used at TUNL is to set the 1×Cs Compton edge channel at one-half the height of the maximum near the Compton edge. This point is equivalent to an electron recoil energy of $0.47 \lesssim E \lesssim 0.55$ MeV, depending on the detector resolution. A ^{137}Cs gamma PH spectrum was taken for each detector roughly every 8 hours to check the stability of the electronics and of the PMT.

6.2.2 Data Analysis

Only events with pulse-heights larger than that corresponding to $\frac{1}{3}$×Cs recoil edge were processed. This requirement was imposed by setting a software gate in the PH spectrum. The events that passed the PH threshold requirement were used to form a two-dimensional histogram of PH vs PSD as explained in Section 5.1.2. A two-dimensional (2D) gate was set in this spectrum around the neutrons. The events falling within the 2D gate were used to increment a TOF histogram. Sample TOF histograms are shown in Fig. 6.2.

The efficiency for each detector was calculated using the following equation

$$\varepsilon(E_n) = \frac{\eta_f Y_d}{T_{gc} \frac{d\sigma}{d\Omega}(E_n, \vartheta_{lab})}, \tag{6.1}$$

where Y_d is the yields per kBCI. The Beam Current Integrator (BCI) counts are proportional to the charge deposited on the gas cell by the beam. The factor $\frac{d\sigma}{d\Omega}(E_n, \theta_{lab})$ is the cross section for the ^{2}H(d,n)^{3}He reaction as a function of neutron energy E_n and lab neutron production angle θ_{lab} [Dro78], T_{gc} is the neutron attenuation factor due to the deuterium

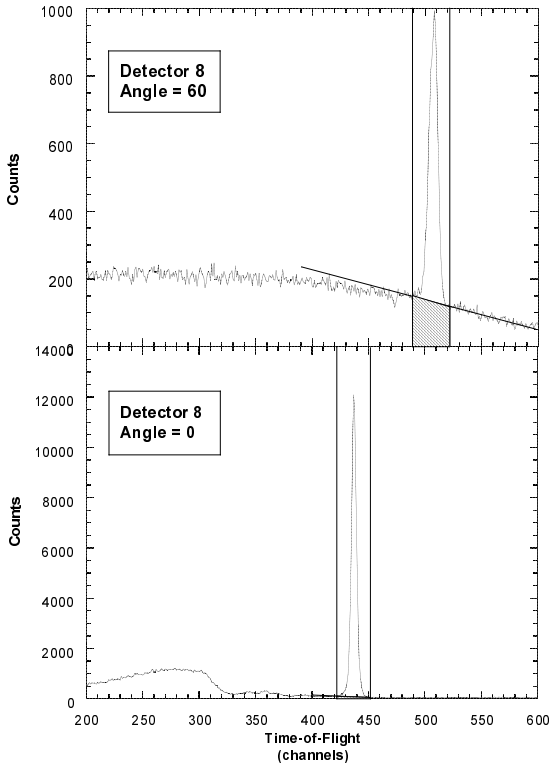

Figure 6.2: Sample TOF spectrum of the ^{2}H(d,n)^{3}He experiment at 0° and at 60° for $E_d = 9.0$ MeV. The number of neutrons detected is the number of counts under the peak inside the gate shown, after background subtraction. The background is the shaded region in the figure.

gas and the construction materials of the gas cell for all neutron energies and emission angles considered [Ped86]. The net neutron yield/kBCI Y_d is corrected for dead time and the background is subtracted using a linear fit in the vicinity of the neutron peak in the TOF spectrum as shown in Fig. 6.2. The factor η_f is given by

$$\eta_f = \frac{1}{\Omega N_t N_i}, \tag{6.2}$$

where Ω is the solid angle subtended by the neutron detector, N_i is the number of deuterons per BCI incident on the gas cell, and N_t is the density of deuterium atoms in the gas cell.

To calculate N_t, the deuterium in the gas cell is considered an ideal gas. The number of deuterons is given by the ideal gas law

$$N_t = \frac{lP}{RT}, \tag{6.3}$$

where l is the length of the gas cell (3.1±0.05 cm), P is the deuterium gas cell pressure in pounds-per-square-inch (PSI) (∼14.75±0.1 PSI), T is the ambient temperature during the measurement (∼293.6±0.5° K), and R is the ideal gas constant (1205.94 cm^3-PSI/mol-K).

6.2.3 Results

Neutron detection efficiencies were determined for all neutron detectors used in the a_{np} experiment. The efficiencies for detectors 8, 9 and 19 are compared with the results of Monte-Carlo calculated efficiencies in Fig. 6.3. The Monte-Carlo code was obtained from the Physikalisch-Technische Bundesenstalt (PTB) and has already been used in other experiments with good results. A normalization of ∼0.98 was applied to the calculated efficiencies to bring them in closer agreement with the experimental efficiencies.

6.3 The ^{252}Cf Measurements at TUNL

6.3.1 Experimental Setup

This measurement was carried out in the Time-of-Flight target area at TUNL. A well calibrated ^{252}Cf source was bought from PTB. The ^{252}Cf was deposited on a circular smooth platinum disk (15 mm in diameter), positioned with insulators inside a parallel plate ionization chamber (25 mm in diameter) used to detect the ^{252}Cf fission fragments. The plates were 2 mm apart. During operation a continuous flow of methane was used as the counter gas. The ionization chamber was mounted on an aluminum frame. The frame was in turn secured to a steel post and bolted to the floor.

Two neutron detectors were placed at ±15° with respect to the normal to the source disk. The distance between the center of the source and the center of each scintillator cell

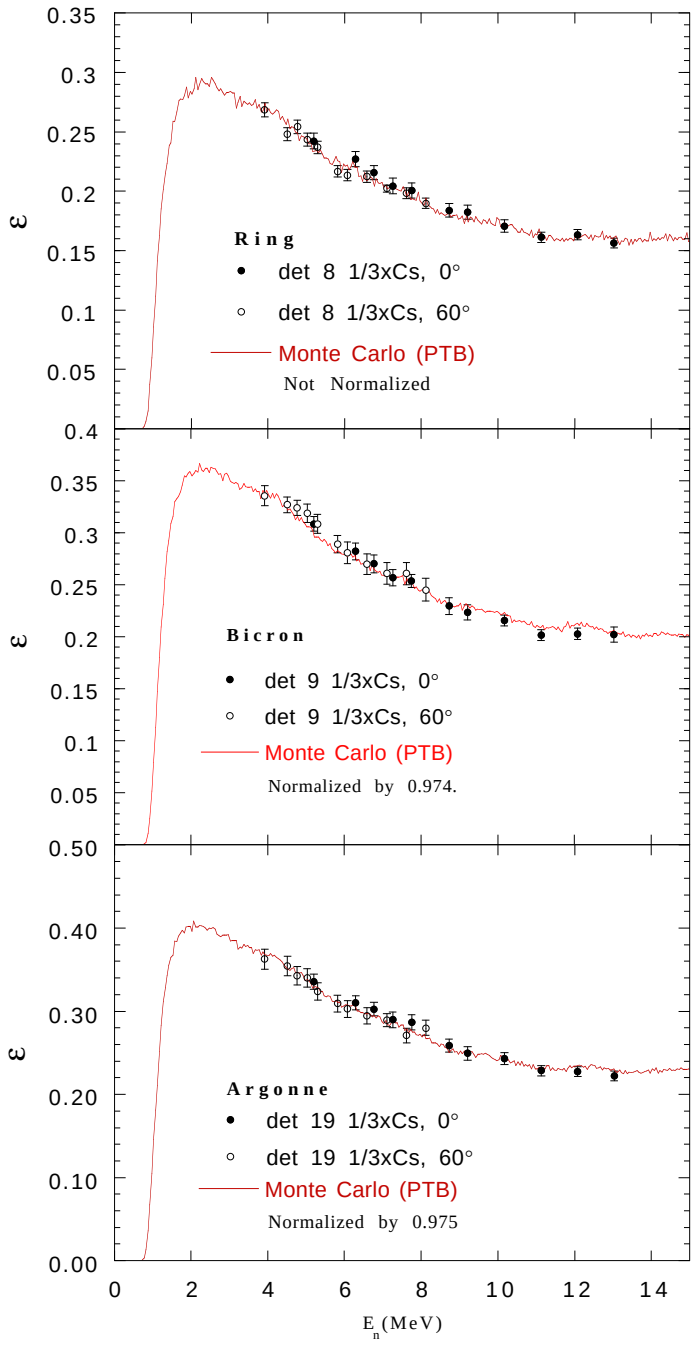

Figure 6.3: Comparison of the efficiency obtained from the ^{2}H(d,n)^{3}He measurement and Monte-Carlo simulations for the three types of neutron detectors used in the a_{np} experiment. The Monte-Carlo simulations are normalized to the data.

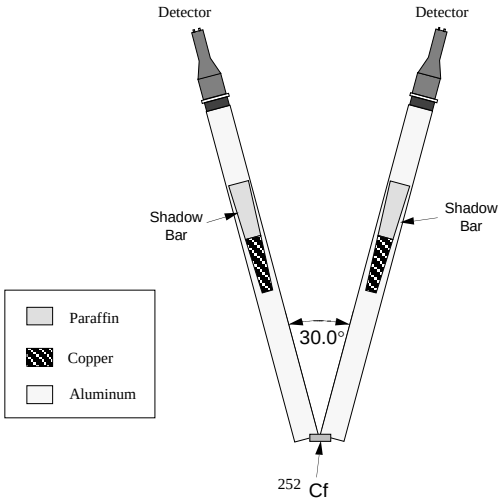

Figure 6.4: Experimental setup for the ^{252}Cf efficiency measurement. The ^{252}Cf source is not drawn to scale.

was about 3.00 m. The detectors were mounted on aluminum frames and placed on steel posts. Two aluminum I-beams were used to connect the source's steel post with the posts of the two detectors. These I-beams were used to place the shadow cones, which were used to measure the amount of neutrons that reach the detectors indirectly through scattering from materials in the target room and from air. The shadow cones consisted of a truncated copper cone to stop gamma rays and neutrons, followed by a truncated cone of paraffin to stop neutrons. The copper cone had a length of 50.8 cm, the top radius was 2.78 cm, and the bottom radius was 3.73 cm. The paraffin cone had a length of 45.7 cm, the top radius was 3.92 cm, and the bottom radius is 4.76 cm. With these dimensions, the shadow cones reduced the flux of 10 MeV neutrons on the detectors by a factor of 6000. A diagram of the setup is shown in Fig. 6.4. To obtain a $\pm 1\%$ statistical accuracy for neutron energies between ~ 3.0 and ~ 6.0 MeV, data was accumulated for at least 48 hours without shadow cones and 24 hours with shadow cones.

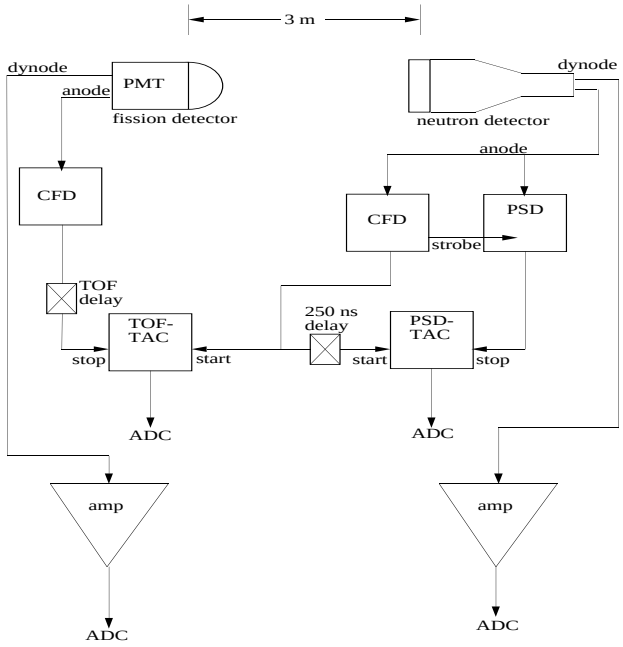

Figure 6.5: Electronics setup for the efficiency measurement with the ^{252}Cf source.

The signal from the ^{252}Cf source was inverted, integrated and amplified by an Ortec VT-120B fast preamplifier in series with a fast Phillips 771 fast amplifier. A Canberra 1428 CFD working in leading-edge mode set a hardware threshold on the pulse-height signal from the source, minimizing undesired noise and the signals from alpha particles. The PH signal from the source was sent to an ADC.

The anode signal from each neutron detector was sent to a Canberra 2160A PSD module, and to a Canberra 1428 CFD. One output signal of the CFD strobed the PSD module and started the two Ortec 467 TACs. One TAC was stopped by the output of the PSD module. The second TAC was stopped by the output signal of CFD used for the source pulses after a 650 ns delay. The output of this TAC was 650 ns minus the TOF of neutrons and gammas from the source to the detector. The outputs of both TACs were sent to an EG&G AD413A ADC. The single-channel analyzer (SCA) outputs of both TACs were sent

to an Ortec 418A universal coincidence set to the logic AND position. The output of the universal coincidence was used to gate the ADC. The dynode of the neutron detectors was amplified in Ortec 572 amplifiers and then sent to the EG&G ADC to be digitized. A diagram of the electronics of this measurement is shown in Fig. 6.5. Scalers were used to measure the fission rate, and the dead time in the whole circuit.

6.3.2 Data Analysis

The PH signal was used to set software thresholds at $\frac{1}{3}\times$Cs in the same way as in the ^{2}H(d,n)^{3}He measurement. Gamma rays were almost completely eliminated by setting a two-dimensional gate in a histogram of PH vs PSD time. A TOF histogram was accumulated with those events satisfying the PH and the PSD requirement.

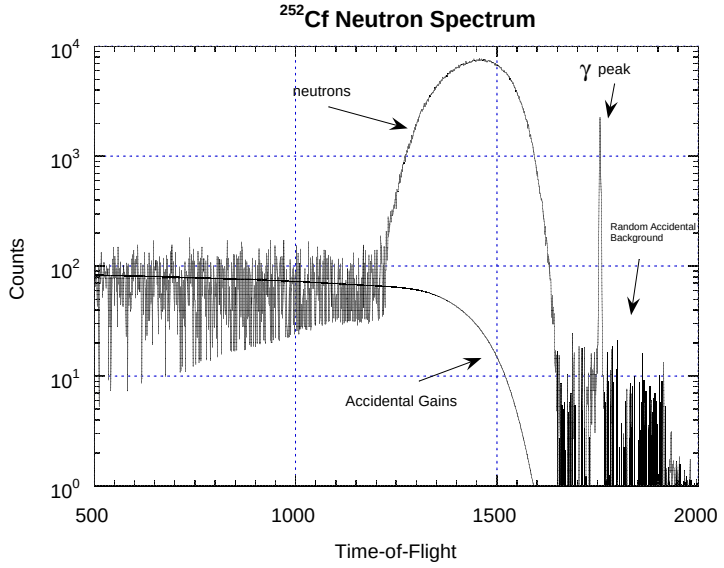

Figure 6.6: ^{252}Cf Neutron Time-of-Flight spectrum for detector 8. Time increases from right to left. The solid curve represents the accidental gains from false start events. The first sharp peak are the gamma events. Events prior to the gamma peak are the random accidentals. Time increases towards the left.

A combination of FORTRAN programs and histogram manipulations using the

TUNL XSYS data analysis package was used to determine the efficiency for each detector. The accidental background due to purely random coincidences (see Section 5.1.1) in the TOF spectra of the foreground and background measurements, was subtracted by creating a flat histogram of height equal to the average height of the flat background that appears before the gamma peak. This region is shown in Fig. 6.6 as "random accidental background". To subtract the correlated background due to false starts we used a FORTRAN code called ACCALC.FOR, which implements the iterative procedure explained in Section 5.1.1. This code created two histograms, one for losses and one for gains for both the foreground and the background spectra. The losses histogram was added, and the gains subtracted from the corresponding spectra. After the correction for accidental gains and losses, the background spectra were normalized by the ratio of the number of hours of data taken in the foreground configuration to the hours of data accumulated for the background configuration. Then the foreground and background spectra were corrected for dead time and subsequently the background was subtracted from the foreground. The resulting TOF spectrum is used to calculate the efficiency.

The efficiency was calculated using a FORTRAN code called EFCALC.FOR. The code first took the TOF spectrum corrected for accidentals and background neutrons, and subdivided it into bins of equal energy. The counts in each bin was the number of neutrons detected at the energy of the centroid of the bin. Next the code calculated the number of neutrons hitting the detector for each bin. For this the program used the known energy distribution of the neutrons produced by ^{252}Cf . This distribution was normalized by the measured fission rate and then corrected for the attenuation of neutrons in air, the attenuation in the detector face, and the efficiency of the detection of fission fragments correlated with neutrons detected at $\pm 15^{\circ}$ [Cub89]. The efficiency at the energy of the bin was taken as the ratio of the number of detected neutrons to the number of neutrons incident on the detector.

6.3.3 Results

Efficiencies were measured for two detectors of each of the three types used in the *np* FSI cross-section measurements. Fig. 6.7 shows the measured efficiencies calculated for the three different types of detectors used in the a_{np} experiment compared to the Monte-Carlo simulations discussed earlier in this chapter. The efficiencies determined using the ^{252}Cf source agree within the error bars with the results from the ^{2}H(d,n)^{3}He calibration. The advantage of the ^{252}Cf method is that the efficiency can be measured for neutron energies close to the $\frac{1}{3}\times$Cs threshold. There was a discrepancy between the efficiency measured for Argonne detectors and the results of the simulation at energies below 4.0 MeV. For the analysis of the *nd* breakup data, a table with the experimental efficiency for that type of detector was used instead of the PTB efficiencies.

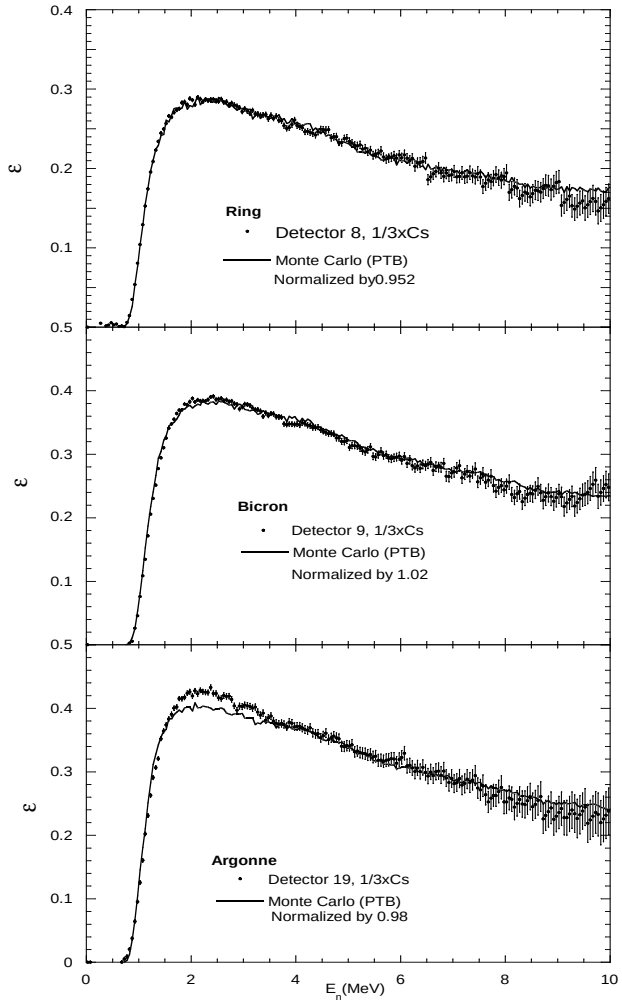

Figure 6.7: Comparison of efficiency from the ^{252}Cf measurement for the three types of neutron detectors used in the a_{np} experiment to a Monte-Carlo simulation. The Monte-Carlo simulation is normalized to the data.

Chapter 7

Results and Conclusions

Cross sections have been measured for the *np* FSI at four emission angles (20.5°, 28.0°, 35.5°, and 43.0°) of the *np* pair in *nd* breakup at an incident neutron energy of 13.0 MeV. All measurements were made at TUNL and used the shielded neutron source in the high-energy bay area of the tandem laboratory. Two detector configurations were used at each angle. For each angle, the cross sections measured with the two detector configurations were compared. The data for the two configurations at all angles were in agreement within their statistical accuracy. The statistical uncertainty of each data point at the maximum of the *np* FSI enhancement was less than 4.8% in every configuration. The cross-section data were used to determine a value of the $^1S_0$ *np* scattering to a statistical uncertainty of ±0.2 fm and a systematic uncertainty of ±0.78 fm. Our results and findings are presented in the sections to follow.

7.1 The Experimental Cross Sections

Cross sections were determined from the experimental data for the eight configurations in our experimental setup. The cross sections were extracted using the techniques described in chapter 5 and are reported as a function of the distance S along the point-geometry kinematic locus. The proportion of the kinematic S-curve measured in each

configuration was determined by the threshold settings of the detectors used in that configuration. The counts in $E_1 - E_2 - E_3$ space were projected into 0.5 MeV wide bins along the S-curve. Only the data points along the curve where the particle energies of all events projected on them were above the experimental thresholds are reported. For all configurations considered here, the points on the *np* FSI peak meet this requirement, perhaps with the exception of the distribution for $\theta_{np} = 20.5^\circ$. Details are given below.

For all the configurations, the points used in the χ^2 analysis were the ones at the peak and two points on each side of the peak. This was done because only those points are sensitive to the variations in a_{np}.

The data were accumulated in 10 beam-time periods (see Table 5.1). However, only the data from the last seven periods were used. The data from the first three experimental runs were left out of the analysis because of irregularities in the center detector pulse-height distribution. This problem made the uncertainty in the extraction of the beam-target luminosity too large for those runs. Nevertheless, the data from the other seven runs provided the intended statistical precision in the cross-section measurement. Additionally, the data from the sixth run was not used in the determination of the cross section for both configurations at 28.0°. During that run period there were problems with the base of the photomultiplier tube of detector #19. This back-angle detector was common to both configurations at that angle.

The experimental cross sections are shown in Figs. 7.1, 7.2, 7.3 and 7.4 in comparison with theoretical predictions from 3N Faddeev calculations for a_{np} values of -22.0, -23.0, -23.75, and -25.0 fm. The error bars are statistical only. The finite-geometry effects, the energy spreads and the detector energy resolutions of our experiment have been folded into the theoretical predictions using Monte-Carlo simulations.

The cross section data for both 20.5° *np* FSI configurations are in strong disagreement with the theoretical predictions. Though part of the motivation for making these measurements is to identify discrepancies between data and theory, we do not believe the

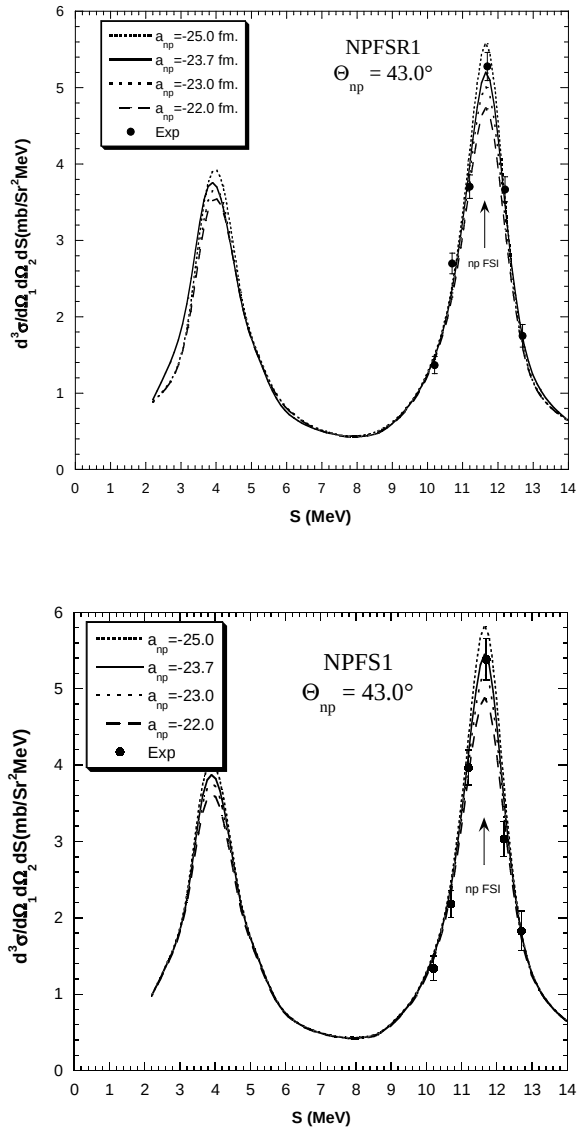

Figure 7.1: Cross section for $\theta_{np} = 43.0^\circ$ ($\theta_1 = 43.0^\circ, \theta_2 = 55.7^\circ, \phi_{12} = 180^\circ$). The data in the top plot were taken with the annular detector, and those in the bottom plot were taken with the back (Bicron) detector. The curves are finite-geometry theoretical predictions from 3N Faddeev calculations for $a_{np} = -22.0, -23.0, -23.75$, and -25.0 fm.

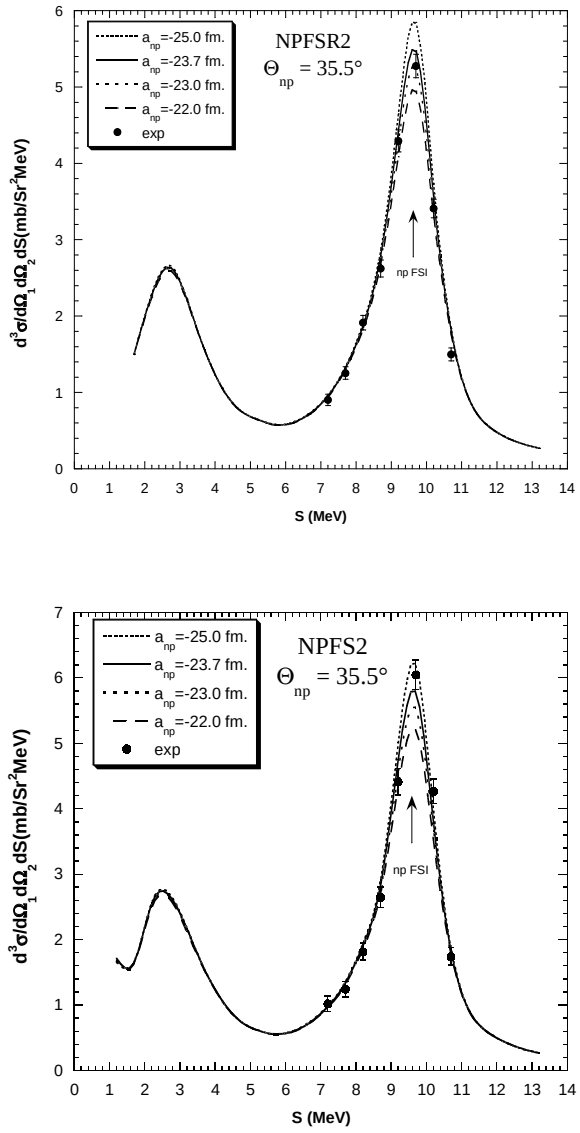

Figure 7.2: Cross section for $\theta_{np} = 35.5°$ ($\theta_1 = 35.5°, \theta_2 = 69.0°, \phi_{12} = 180°$). The data in the top plot were taken with the annular detector, and those in the bottom plot were taken with the back (Bicron) detector. The curves are finite-geometry theoretical predictions from 3N Faddeev calculations for $a_{np} = -22.0, -23.0, -23.75$, and -25.0 fm.

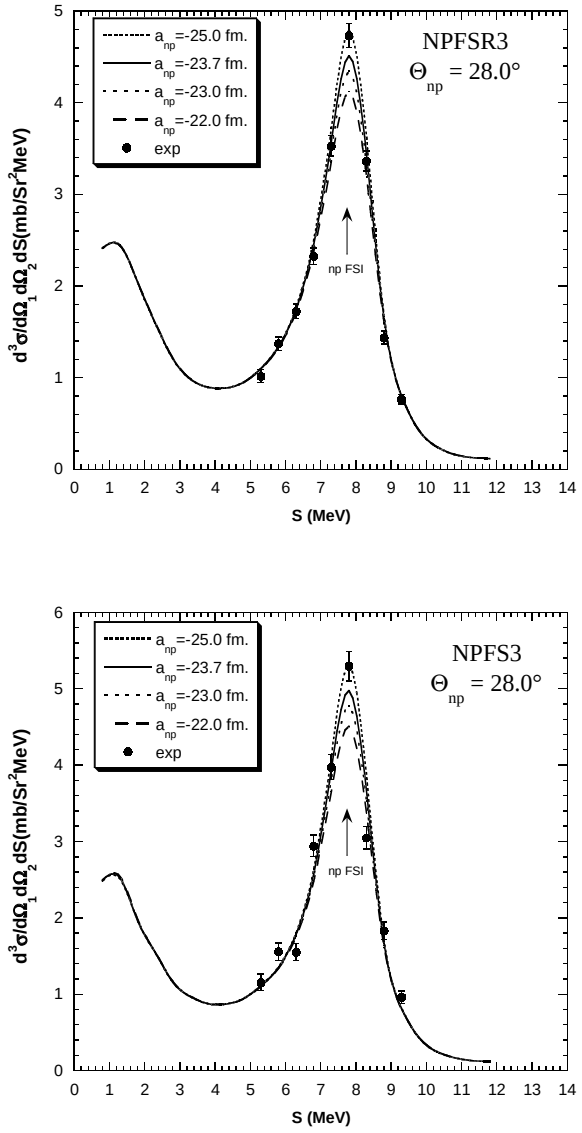

Figure 7.3: Cross section for $\theta_{np} = 28.0^\circ$ ($\theta_1 = 28.0^\circ, \theta_2 = 83.5^\circ, \phi_{12} = 180^\circ$). The data in the top plot were taken with the annular detector, and those in the bottom plot were taken with the back (Bicron) detector. The curves are finite-geometry theoretical predictions from 3N Faddeev calculations for $a_{np} = -22.0, -23.0, -23.75$, and -25.0 fm.

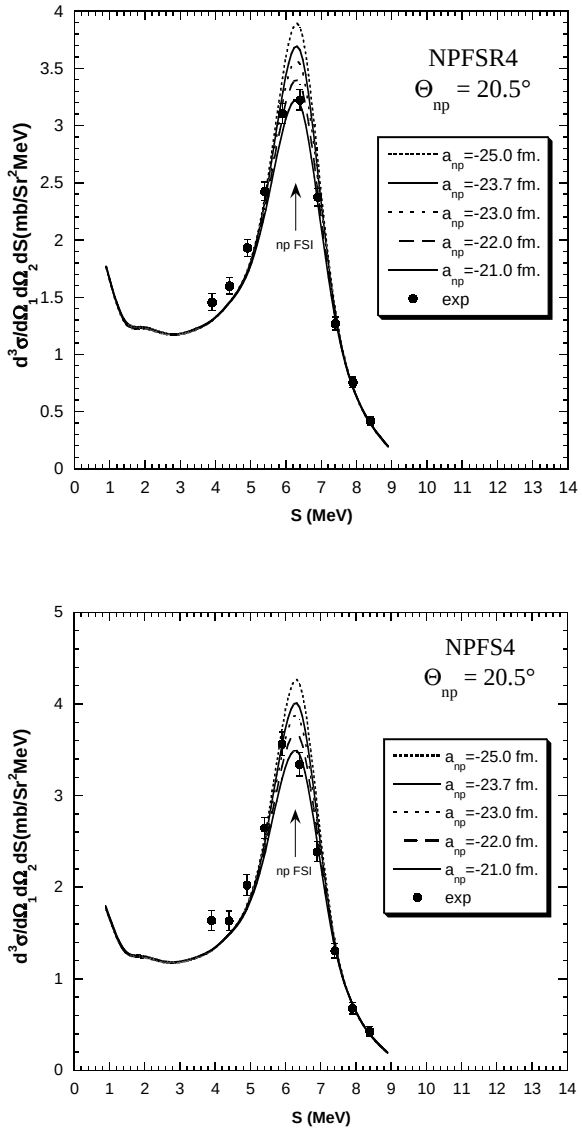

Figure 7.4: Cross section for $\theta_{np} = 20.5^\circ$ ($\theta_1 = 20.5^\circ, \theta_2 = 100.5^\circ, \phi_{12} = 180^\circ$). The data in the top plot were taken with the annular detector, and those in the bottom plot were taken with the back (Bicron) detector. The curves are finite-geometry theoretical predictions from 3N Faddeev calculations for $a_{np} = -22.0, -23.0, -23.75$, and -25.0 fm.

observed difference is a real physics effect. Instead, it is most likely an instrumentation problem. This conclusion is based on two observations. First, the magnitude of the measured cross section at the maximum of the *np* FSI peak dropped too abruptly in the 7.5° from 28.0°. The measured cross section at the *np* FSI peak differs by only 11% between 35.5° and 28.0°, with the cross section at 28.0° being lower. Whereas, between 28.8° and 20.5° it falls by 39%. The change in the point geometry cross section must be even greater. It is difficult to imagine a physics process in the *nd* system that could cause such a drastic change in the breakup cross section in only a 7.5° span. The second reason we believe the effect to be instrumental is the inability of the theoretical predictions to fit the shape of the *np* FSI at 20.5° for the configuration that uses the back (Bicron) detector. The configuration with the annular detector is well fit by the theory but it is in strong disagreement with other configurations.

The reason for the discrepancy is that for this configuration the energy of neutron 2 is close to the steep slope of the neutron detection efficiency curve. Small errors in the determination of the threshold for the back detector in this configuration lead to large errors in the neutron detection efficiency which translate into large errors in the determination of the cross section. For this reason the results from this configuration are not used in the calculation of the final result.

7.2 Resulting a_{np} from the TUNL Experiment

The value of a_{np} for each configuration was obtained from a χ^2 comparison between the experimental cross section and rigorous 3N calculations for the *np* FSI . The details of the analysis are described in Section 5.4. Simulated cross-sections for $a_{np} = -22.0, -23.0, -23.75$ and -25.0 fm were used in the χ^2 analysis. Between the above points a linear interpolation was made to find the cross section in steps of 0.2 fm.

Our results for each of the eight configurations measured are shown in Table 7.2. The errors are statistical only.

i	$\theta_{np}(^\circ)$	a^i_{np} (fm)	$(\Delta a^{stat}_{np})_i$ (fm)
1	43.0°	-23.9	± 0.40
2	35.5°	-22.7	± 0.39
3	28.0°	-23.7	± 0.41
4	20.5°	-21.7	± 0.35
5	43.0°	-22.6	± 0.67
6	35.5°	-24.1	± 0.49
7	28.0°	-23.6	± 0.52
8	20.5°	-21.3	± 0.48

Table 7.1: The a_{np} values extracted from the np FSI cross sections.

The statistically-weighted average of a_{np} for each of the four production angles is calculated using

$$a_{np} = \frac{\sum_i \frac{a^i_{np}}{(\Delta a^{stat}_{np})_i{}^2}}{\sum_i \frac{1}{(\Delta a^{stat}_{np})_i{}^2}}, \tag{7.1}$$

and the statistical error of the mean [Bev69] was given by

$$\Delta a_{np} = \sqrt{\frac{1}{\sum_i \frac{1}{(\Delta a^{stat}_{np})_i{}^2}}}. \tag{7.2}$$

The results of the averaging are shown in Table 7.2,

$\theta_{np}(^\circ)$	a_{np} (fm)	Δa^{stat}_{np} (fm)
43.0°	-23.6	± 0.34
35.5°	-23.2	± 0.31
28.0°	-23.7	± 0.32
20.5°	-21.6	± 0.28

Table 7.2: The a_{np} average values for each production angle.

The results of the first three production angles were averaged statistically. The resulting value was $a_{np} = -23.5 \pm 0.2$ fm. The systematic error of the average a_{np} was cal-

culated using the procedure described in section 5.4.4 and was found to be ± 0.78 fm. Combining the statistical and systematic uncertainties our final value is $a_{np} = -23.5 \pm 0.8$ fm.

7.3 Conclusions

7.3.1 Absence of a Strong Three-Body Force

It has been suggested that the a_{nn} discrepancy between $\pi^- - d$ and kinematically-complete nd breakup experiments could be due to a three-body force present in the exit channel of the latter reaction [Šla89]. The value of a_{np} extracted from this experiment is in good agreement with the accepted value of a_{np} measured in two-nucleon reactions [Koe75] for the configurations at $\theta_{np} = 28.0°$, $35.5°$, and $43.0°$. This result indicates that in nd breakup , the presence of the third nucleon does not affect the nucleon-nucleon interaction significantly at those angles. The 2.1 fm difference needed to solve the discrepancy in the measurements of a_{nn}, is clearly ruled out by this experiment.

The result at $20.5°$ does show a strong disagreement with the two-nucleon value. However, because of the region in energy space of this configuration this result should not be used in the determination of a_{np} in nd breakup . Small errors in the determination of the threshold in the pulse height of neutron 2 lead to large errors in the cross section for this configuration.

Additionally, we do not observe a significant angular dependence of a_{np} as suggested by the Tucson-Melbourne three-nucleon force using a cutoff parameter $\Lambda = 5.8 m_\pi$ [Wit96]. The value extracted for a_{np} does not exhibit a systematic dependence on the angle. This represents a further constraint on the effect a three-nucleon force should have on this system.

Appendix A

nd breakup Cross-Section Tables

The following tables show the cross sections measured in this experiment. The cross sections were used to determine the value of a_{np} for all detector configurations. The tables also show theoretical predictions for the cross sections from Monte Carlo simulations for four values of a_{np}.

	experimental cross sections ($\frac{mb}{sr^2 MeV}$)		calculated finite-geometry cross sections ($\frac{mb}{sr^2 MeV}$)			
S (MeV)	$\frac{d^3\sigma(S)}{d\Omega_1 d\Omega_2 dS}$	stat. error	-22.0 fm	-23.0 fm	-23.7 fm	-25.0 fm
npfsr1 configuration ($\theta_{np} = 43.0°$)						
10.20	1.37	0.11	1.44	1.46	1.47	1.50
10.70	2.70	0.13	2.26	2.31	2.36	2.41
11.20	3.70	0.15	3.70	3.87	3.98	4.19
11.70	5.28	0.18	4.72	5.00	5.19	5.58
12.20	3.67	0.16	3.15	3.27	3.46	3.50
12.70	1.75	0.15	1.59	1.61	1.73	1.65
npfsr2 configuration ($\theta_{np} = 35.5°$)						
7.20	0.90	0.07	0.94	0.95	0.95	0.96
7.70	1.25	0.08	1.30	1.31	1.32	1.33
8.20	1.91	0.10	1.83	1.85	1.87	1.90
8.70	2.62	0.11	2.67	2.74	2.79	2.86
9.20	4.29	0.14	4.09	4.29	4.42	4.65
9.70	5.28	0.15	4.95	5.25	5.48	5.85
10.20	3.41	0.12	3.34	3.47	3.57	3.73
10.70	1.50	0.08	1.76	1.78	1.80	1.84
npfsr3 configuration ($\theta_{np} = 28.0°$)						
5.30	1.02	0.07	1.10	1.10	1.10	1.10
5.80	1.37	0.07	1.33	1.33	1.34	1.34
6.30	1.72	0.08	1.72	1.74	1.75	1.76
6.80	2.33	0.09	2.38	2.42	2.46	2.51
7.30	3.52	0.11	3.36	3.48	3.57	3.72
7.80	4.74	0.13	4.12	4.35	4.51	4.79
8.30	3.36	0.11	3.19	3.33	3.43	3.60
8.80	1.44	0.07	1.60	1.62	1.64	1.67
9.30	0.76	0.05	0.79	0.80	0.80	0.80
npfsr4 configuration ($\theta_{np} = 20.5°$)						
3.90	1.46	0.07	1.30	1.30	1.30	1.29
4.40	1.60	0.07	1.46	1.46	1.46	1.46
4.90	1.93	0.07	1.71	1.72	1.72	1.73
5.40	2.43	0.08	2.28	2.31	2.34	2.38
5.90	3.10	0.09	3.09	3.20	3.28	3.42
6.40	3.23	0.09	3.37	3.53	3.66	3.86
6.90	2.38	0.08	2.45	2.53	2.60	2.70
7.40	1.27	0.06	1.34	1.35	1.36	1.38
7.90	0.75	0.05	0.71	0.71	0.71	0.71
8.40	0.42	0.04	0.39	0.39	0.39	0.39

Table A.1: Experimental and Monte-Carlo calculated *nd* breakup cross sections for the configurations using an annular detector for the detection of neutron 1.

	experimental cross sections ($\frac{mb}{sr^2 MeV}$)		calculated finite-geometry cross sections ($\frac{mb}{sr^2 MeV}$)			
S (MeV)	$\frac{d^3\sigma(S)}{d\Omega_1 d\Omega_2 dS}$	stat. error	−22.0 fm	−23.0 fm	−23.7 fm	−25.0 fm
npfsr1 configuration ($\theta_{np} = 43.0°$)						
10.20	1.34	0.16	1.46	1.49	1.51	1.53
10.70	2.18	0.18	2.33	2.38	2.41	2.48
11.20	3.97	0.23	3.88	4.04	4.17	4.40
11.70	5.39	0.27	4.87	5.19	5.44	5.81
12.20	3.04	0.23	3.32	3.46	3.56	3.73
12.70	1.83	0.26	1.72	1.76	1.79	1.81
npfsr2 configuration ($\theta_{np} = 35.5°$)						
7.2	1.02	0.12	0.96	0.97	0.98	0.99
7.7	1.25	0.12	1.31	1.33	1.34	1.35
8.2	1.82	0.13	1.86	1.89	1.91	1.94
8.7	2.65	0.16	2.71	2.78	2.83	2.91
9.2	4.41	0.20	4.36	4.58	4.75	5.01
9.7	6.05	0.22	5.21	5.54	5.78	6.21
10.2	4.27	0.19	3.51	3.66	3.78	3.96
10.7	1.74	0.13	1.78	1.81	1.83	1.86
npfsr3 configuration ($\theta_{np} = 28.0°$)						
5.3	1.16	0.11	1.10	1.11	1.11	1.11
5.8	1.56	0.12	1.34	1.35	1.35	1.36
6.3	1.55	0.11	1.75	1.77	1.79	1.80
6.8	2.94	0.14	2.48	2.54	2.57	2.64
7.3	3.98	0.17	3.66	3.82	3.95	4.12
7.8	5.30	0.19	4.51	4.77	4.98	5.32
8.3	3.05	0.15	3.37	3.53	3.65	3.84
8.8	1.83	0.11	1.61	1.64	1.66	1.69
9.3	0.96	0.08	0.80	0.80	0.81	0.81
npfsr4 configuration ($\theta_{np} = 20.5°$)						
3.9	1.58	0.11	1.32	1.32	1.31	1.31
4.4	1.57	0.11	1.49	1.49	1.49	1.49
4.9	1.97	0.11	1.77	1.78	1.79	1.80
5.4	2.63	0.12	2.40	2.44	2.47	2.53
5.9	3.56	0.13	3.32	3.45	3.55	3.72
6.4	3.31	0.13	3.64	3.83	3.97	4.22
6.9	2.38	0.11	2.59	2.69	2.76	2.89
7.4	1.27	0.08	1.37	1.39	1.40	1.43
7.9	0.66	0.06	0.72	0.73	0.73	0.73
8.4	0.42	0.05	0.40	0.40	0.39	0.39

Table A.2: Experimental and Monte-Carlo calculated *nd* breakup cross sections for the configurations using a Bicron detector for the detection of neutron 1.

Appendix B

Kinematic Plots

The following plots show the kinematic loci for the four production angles of our experiment, projected onto the E_1 vs E_2 plane (solid), the E_1 vs E_3 plane (dashes), and the E_2 vs E_3 plane (dotted dashes). The location of the *np* FSI peak is indicated with the large marker on each curve. The small marker is used to indicate the position of the small peak in the *np* FSI cross section.

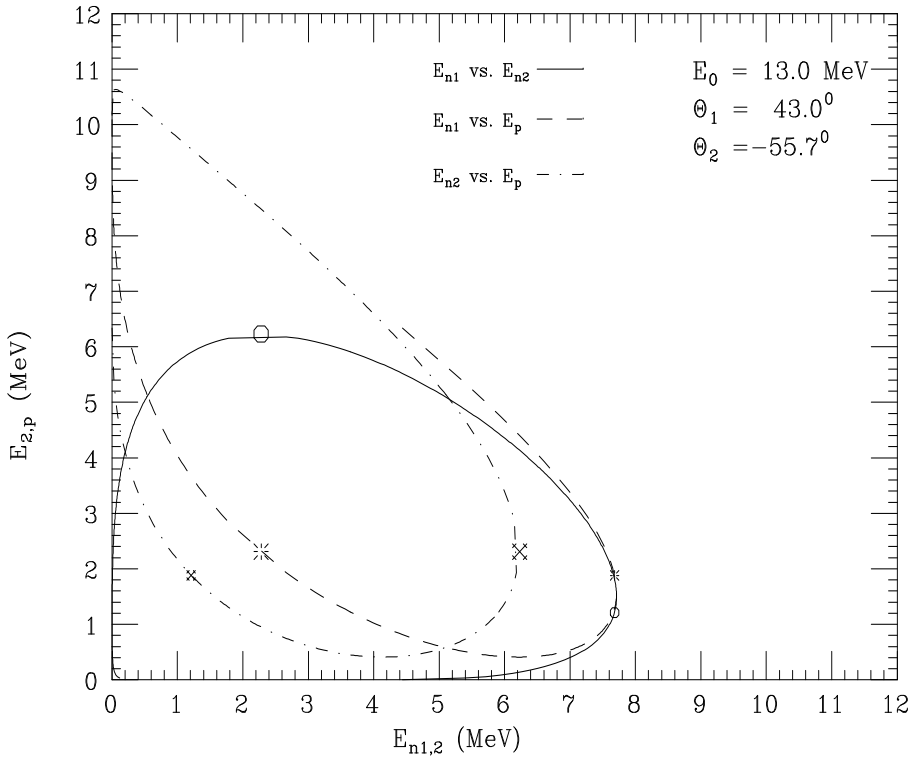

Figure B.1: Kinematic curves for E_2 (solid) and E_3 (dashes) as a function of E_1, and for E_3 as a function of E_2 (dotted dashes) for $\theta_{np} = 43.0^\circ$.

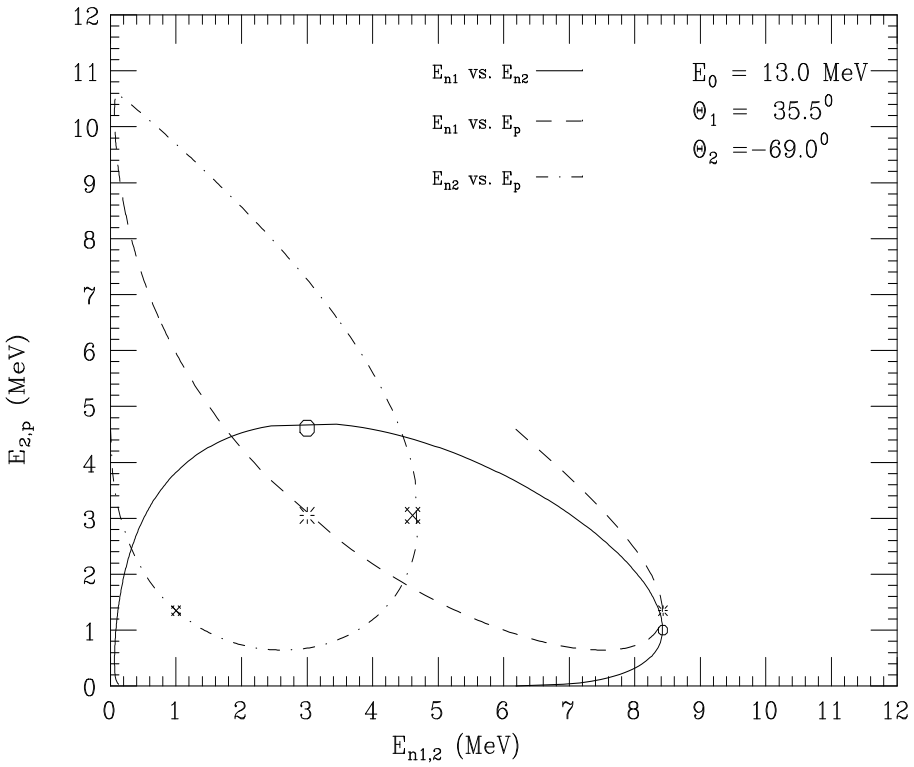

Figure B.2: Kinematic curves for E_2 (solid) and E_3 (dashes) as a function of E_1, and for E_3 as a function of E_2 (dotted dashes) for $\theta_{np} = 35.5^\circ$.

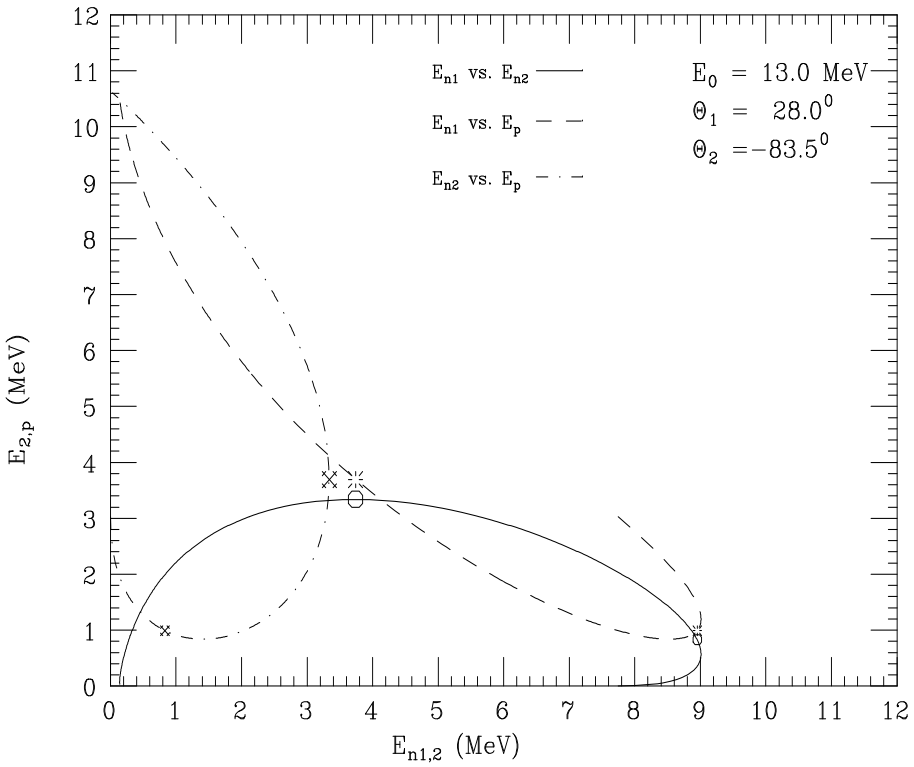

Figure B.3: Kinematic curves for E_2 (solid) and E_3 (dashes) as a function of E_1, and for E_3 as a function of E_2 (dotted dashes) for $\theta_{np} = 28.0^\circ$.

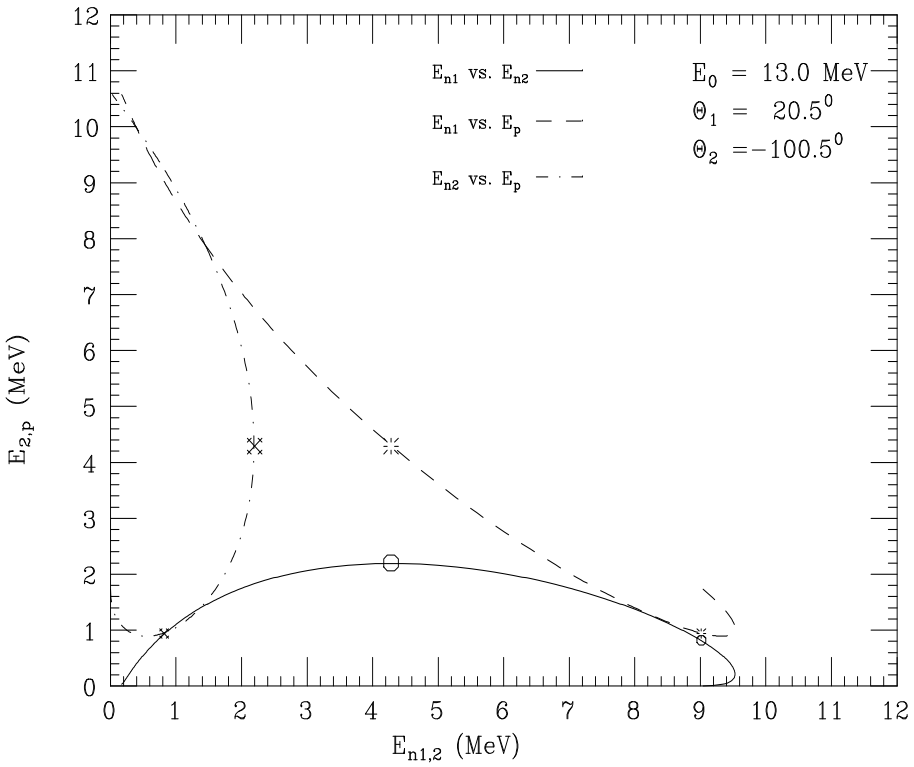

Figure B.4: Kinematic curves for E_2 (solid) and E_3 (dashes) as a function of E_1, and for E_3 as a function of E_2 (dotted dashes) for $\theta_{np} = 20.5^\circ$.

Bibliography

[Alt67] E. O. Alt, P. Grassberger, and W. Sandhas. *Reduction of the Three-Particle Collision Problem to Multi-Channel Two-Particle Lippmann-Schwinger Equations.* Nuclear Physics, **2**(1967) 167.

[Axi43] B.M. Axilrod and E. Teller. Journal of Chemical Physics, **11**(1943) 299.

[Bev69] P. R. Bevington. *Data Reduction and Error Analysis for the Physical Sciences.* McGraw-Hill, 1969.

[Boe91] R. Boettger, H. Klein, A. Chalupka, and B. Strohmaier. *Investigation of the Spectral Fluence of the Neutrons from the Spontaneous Fission of ^{252}Cf by means of Time-of-flight Spectrometry.* Technical Report PTB-ND-22, Physikalisch-Technische Bundesanstalt, Bundesallee 100, W-3300 Braunschweig, 1991.

[Brü70] H. Brückman, W. Kluge, H. Matthäy, L. Schanzler, and K. Wick. *The Angular Distribution of Final State Interacting n-p Pairs in the reaction $p+d \to p+p+n$.* Nuclear Physics, **A**(1970) 209–230.

[Cub89] J. Cub, E. Finckh, K. Gebhardt, K. Geissdörfer, R. Lin, and J. Strate. *The Neutron Detection Efficiency of NE213 Detectors measured by Means of a ^{252}Cf source.* Nuclear Instruments and Methods in Physics Research, **A274**(1989) 217–221.

[Dro78] M. Drosg. *Unified Absolute Differential Cross Sections for Neutron Production by the Hydrogen Isotopes for Charge-Particle Energies Between 6 and 17 MeV.* Nuclear Science and Engineering, **67**(1978) 190–220.

[Fad61] L.D. Faddeev. *Scattering Theory for a Three-Particle System.* Journal of Experimental and Theoretical Physics (U.S.S.R.), **12**(1961) 1014–1019.

[Fad65] L.D. Faddeev. *Mathematical Aspects of the Three-Body Problem in the Quantum Scattering Theory.* Israel Program for Scientific Translations, (1965) 1014–1019.

[Fin87] E. Finckh, K. Geissdörfer, R. Lin, S. Schindler, and J. Strate. *Method for Data Analysis of Three Particle Experiments by Monte Carlo Simulation.* Nuclear Instruments and Methods in Physics Research, **A262**(1987) 441–443.

[Fri95] J. L. Friar, G. L. Payne, W. Glöckle, D. Hüber, and H. Witała. *Benchmark solutions for n-d breakup amplitudes.* Physical Review C, **51**(1995) 2356–2359.

[Gab84] B. Gabioud, J.-C. Adler, C. Joseph, J.-F. Loude, N. Morel, A. Perrenoud, J.-P. Perroud, M. T. Tran, E. Winkelmann, W. Dahme, H. Panke, D. Renker, G. Strassner, P. Truöl, and G.F. de Téramond. *nn SCATTERING PARAMETERS a_{nn} and r_{nn} FROM THE PHOTON SPECTRUM OF THE REACTION $\pi^- d \rightarrow \gamma nn$.* Nuclear Physics, **A420**(1984) 496–524.

[Glö96] W. Glöckle, H. Witała, D. Hüber, and J. Golack. *The Three-Nucleon Continuum: Achievements, Challenges and Applications.* Physics Reports, **274**(1996) 107–286.

[GT97] Dinko González Trotter. *Extraction of the $^1S_0$ Neutron-Neutron Scattering Length from a Kinematically Complete N-D Breakup Experiment.* Ph.D. thesis, Duke University, 1997.

[Hüb93] D. Hüber, H. Witała, and W. Glöckle. *Momentum-Space Calculations for Three-Nucleon Scattering Including a Three-Nucleon Force.* Few-Body Systems, **14**(1993) 171–190.

[Koe75] L. Koester and W. Nistler. *New Determination of the neutron-Proton Scattering Amplitude and Precise Measurements of the Scattering Amplitudes on Carbon, Fluorine and Bromine.* Z. Physik, **272**(1975) 189–196.

[Leo94] W.R. Leo. *Techniques for Nuclear and Particle Physics Experiments.* Springer-Verlag, 1994.

[Mac87] R. Machleidt, K. Holinde, and Ch. Elster. *The Bonn Meson-Exchange Model for the Nucleon-Nucleon Interaction.* Physics Reports, **149**(1987) 1–89.

[Mil90] G.A. Miller, B.M.K. Nefkens, and I. Šlaus. *Charge Symmetry, Quarks and Mesons.* Physics Reports, **194**(1990) 1–116.

[Mut43] Y. Muto. Proc. Phys. Mat. Soc., **17**(1943) 629.

[Ped86] R. S. Pedroni. *Cross Sections and Analyzing Powers in the 8 to 17 MeV Range for Neutron Scattering from $^{54,56}Fe$, $^{58,60}Ni$, ^{93}Nb, and ^{120}Sn.* Ph.D. thesis, Duke University, 1986.

[Set95] H. R. Setze. *Differential Cross Section for the Neutron-Induced Deuteron Breakup Reaction at $E_n = 13.0$ MeV.* Ph.D. thesis, Duke University, 1995.

[Šla89] I. Šlaus, Y. Akaishi, and H. Tanaka. *Neutron-Neutron Effective Range Parameters.* Physics Reports, **173**(1989) 259–300.

[Tak51] M. Taketani, S. Nakamura, and M. Sasaki. *On the Method of the Theory of Nuclear Forces.* Progress of Theoretical Physics, **VI**(1951).

[Tor96] W. Tornow, H. Witała, and R. T. Braun. *Determinations of the Neutron-Neutron Scattering Length from Kinematically Incomplete Neutron-Deuteron Breakup Data Revisited.* Few-Body Systems, **21**(1996) 97–130.

[Wit89] H. Witała, W. Glöckle, and Th. Cornelius. *Rigorous Faddeev Calculations for Elastic Neutron-Deuteron Scattering Around 8 MeV c.m. Energy.* Nuclear Physics, **A491**(1989) 157.

[Wit96] H. Witała, D. Hüber, W. Glöckle, W. Tornow, and D. E. González Trotter. *Extraction of the Neutron-Neutron Scattering Length a_{nn} from Kinematically Complete Neutron-Deuteron Breakup Experiments.* Few Body Physics, **20**(1996) 81–92.

Biography

Frank Salinas Meneses

Personal

Born in Arequipa Peru, August 30, 1967

Education

B.S. Physics and Computer Science, Southwestern University, Georgetown, Texas, 1990

M.A. Physics, Duke University, Durham, North Carolina, 1992

Academic Positions

Teaching Assistant, Duke University, 1990–1992

Research Assistant, Duke University, 1992–1997

Memberships

American Physical Society

Alpha Chi

Publications

H. R. Setze, C. R. Howell, W. Tornow, R. T. Braun, W. Glöckle, A. H. Hussein, J. L. Lambert, G. Mertens, C. D. Roper, F. Salinas, I. Šlaus, D. E. González Trotter, B. Vlahović, R. L. Walter, H. Witała. *Verification of the space-star anomaly in nd breakup.* Physics Letters B, **388** 5 (1993).

H. R. Setze, C. R. Howell, R. T. Braun, D. E. González Trotter, A. H. Hussein, C. D. Roper, F. Salinas, I. Šlaus, W. Tornow, B. Vlahović, R. L. Walter, G. Mertens, J. M. Lambert, H. Witała. *Cross-Section Measurements of the Space-Star Configuration in n-d Breakup at 13.0 MeV.* In F. Gross, editor, 14^{th} *International IUPAP Conference on Few Body Problems in Physics.* 1994.

R. T. Braun, W. Tornow, D. E. González Trotter, C. R. Howell, C. D. Roper, F. Salinas, H. R. Setze, R. L. Walter. *Neutron-Proton Analyzing Power at 12 MeV and charged πNN Coupling Constant.* In F. Gross, editor, 14^{th} *International IUPAP Conference on Few Body Problems in Physics.* 1994.

C. R. Howell, H. R. Setze, R. T. Braun, D. E. González Trotter, A. H. Hussein, C. D. Roper, F. Salinas, I. Šlaus, W. Tornow, B. Vlahović, R. L. Walter, G. Mertens, J. M. Lambert, H. Witała. *Probing the three-nucleon force using nucleon-deuteron breakup reactions.* NIM B **99**, 316-319, 1995.

W. Tornow, C. R. Howell, R. T. Braun, Q. Chen, D. E. González Trotter, C. D. Roper, F. Salinas, H. R. Setze, R. L. Walter, H. Witała. *Selected Topics of the Few-Nucleon Research Program at TUNL.* Few-Body Systems Suppl. **8**, 161-165, 1995.

M. A. Al-Ohali, A. Aksoy, A. Coban, J. M. Hanly, P. D. Felsher, C. R. Howell, W. Tornow, F. Salinas, R. L. Walter. *Determination of the neutron detection efficiency of an NE213 scintillator for $E_n = 2.5$ to 16 MeV using the $^2H(d,n)^3He$ reaction.* Nuclear Instruments and Methods in Physics Research A, **396** (1997) 388-393.